Title
Scalable Nano-Manufacturing of Metal-Based Nanocomposites

Author
Javadi, Abdolreza

Publication Date
2018

Peer reviewed|Thesis/dissertation

UNIVERSITY OF CALIFORNIA

Los Angeles

Scalable Nano-Manufacturing of Metal-Based Nanocomposites

A dissertation submitted in partial satisfaction of the

requirements for the degree Doctor of Philosophy

in Mechanical Engineering

by

Abdolreza Javadi

2018

ABSTRACT OF THE DISSERTATION

Scalable Nano-Manufacturing of Metal-Based Nanocomposites

by

Abdolreza Javadi

Doctor of Philosophy in Mechanical Engineering

University of California, Los Angeles, 2018

Professor Xiaochun Li, Chair

The objective of this study is to significantly advance the fundamental knowledge to enable scalable nano-manufacturing of metal-based nanocomposites by overcoming the grand challenges that exist in both fundamental and manufacturing levels. It especially seeks to manufacture bulk aluminum nanocomposite electrical conductors (ANECs) with uniform dispersion and distribution of nanoparticles that offer excellent mechanical and electrical properties.

Polymer-metal nanocomposite is an emerging class of hybrid materials which can offer significantly improved functional properties (e.g. electrical conductivity). Incorporating proper nanoscale metallic elements into polymer matrices can enhance the electrical conductivity of the polymers. To achieve such polymer nanocomposites, the longstanding challenge of uniform dispersion of metal nanoparticles in polymers must be addressed. Conventional scale-down techniques often are only able to shrink larger elements (e.g. microparticles and microfibers) into micro/nano-elements (i.e. nanoparticles and nanofibers) without significant modification in their relative spatial and size distributions. This study uncovers an unusual phenomenon that tin (Sn) microparticles with both poor size distribution and spatial dispersion were stretched into uniformly dispersed and sized nanoparticles in polyethersulfone (PES) using thermal drawing method. It is believed that the capillary instability plays a crucial role during thermal drawing. This novel, inexpensive, and scalable method overcomes the longstanding challenge to produce bulk polymer-metal nanocomposites (PMNCs) with a uniform dispersion of metallic nano-elements (Chapter 3).

Nano-elements (e.g. nanoparticles) are one of the most important constituent of the nanocomposite materials. Since titanium diboride (TiB_2) nanoparticles is of a crucial factor in this study, and more importantly is not commercially available, we synthesized these reinforcements to ensure high purity and size uniformity. Our preliminary results show that TiB_2 nanoparticles with a uniform size can be produced. Further characterization confirmed the presence of crystalline TiB_2 nanoparticles with average size of 8.1 ± 0.4 nm. The in-house synthesized TiB_2 nanoparticles were used to reinforce both aluminum and magnesium matrices. Successful incorporation of TiB_2 nanoparticles in the aforementioned matrices was another indirection indication of high purity and surface-clean TiB_2 nanoparticles (Chapter 4).

Lightweight metallic systems (e.g. Al) have promising potentials for applications in metal-based laser additive manufacturing. Lightweight metals exhibit moderate mechanical properties compare to high density metals (e.g. steel). However, lightweight metal matrix nanocomposites (LMMNCs) offer excellent mechanical properties desirable to improve energy efficiency and system performance for widespread applications including, but not limited to, aerospace, transportation, electronics, automotive, and defense. It has been a longstanding challenge to realize a scalable manufacturing method to produce metal nanocomposite microparticles. This study demonstrates high volume manufacturing of Al and magnesiuim (Mg) nanocomposite microparticles. In-house synthesized TiB_2 and commercial titanium carbide (TiC) nanoparticles were chosen as nano-scale reinforcements. Using a flux-assisted solidification processing method, up to 30% volume fraction nanoparticles were efficiently incorporated and dispersed into Al and Mg microparticles. Theoretical study on nanoparticle interactions in molten metals revealed that TiC and TiB_2 nanoparticles can be self-dispersed and self-stabilized in molten Al and Mg matrices. Metal-based additive manufacturing and thermal spraying coating can significantly benefit from these novel Al and Mg nanocomposite microparticles. This simple yet scalable approach can broaden the applications of such nanocomposite in additive manufacturing of the functional parts. Moreover, the metal nanocomposite microparticles can be applied in conventional manufacturing processing. For example, bulk Al-30 volume percent (vol. %) nanocomposites were produced by cold compaction of Al-30 vol. % TiB_2 nanocomposite microparticles followed by melting. Al-30 vol. % TiB_2 nanocomposites with average Vickers hardness of 458 HV was successfully produced (Chapter 5).

Magnesium is the lightest structure metal applied in broad range of applications in various industries such as biomedical, transportation, construction, naval and electronic. Strengthening Mg is of significance for energy efficiency of numerous transportation systems. Traditional metal strengthening approaches such as elemental alloying have reached their fundamental limits in offering high strength metals functioning at elevated temperature. Adding nanoparticle reinforcements can effectively promote the mechanical properties of Mg nanocomposites. However, manufacturing of bulk magnesium nanocomposites with populous and dispersed nanoparticles remains as a great challenge. Here we report a novel flux-assisted liquid state processing of bulk Mg nanocomposites with TiC as the nanoscale reinforcements. TiC nanoparticles with high hardness and high elastic modulus is well-distributed and uniformly dispersed in the Mg matrix, resulting in a significantly improved Vickers hardness of 143.5±11.5 HV (pure Mg Vickers hardness is about 35 HV). Further theoretical study suggested that TiC nanoparticles can be self-dispersed and self-stabilized in Mg matrix (Chapter 6).

Aluminum is one of the most abundant lightweight metal on Earth with a wide range of practical applications such as electrical wire. However, traditional aluminum manufacturing processing approaches such as elemental alloying, deformation and thermomechanical cannot offer further property improvement due to fundamental limitations. Successful incorporation of ceramic nanoparticles into aluminum have shown unusual property improvements. Adding metal-like ceramic nanoparticles into aluminum matrix can be a promising alternative to produce high performance aluminum electrical wires. Here we show a new class of aluminum nanocomposite electrical conductors (ANECs), with significantly improved average Vickers hardness (130 HV) and good electrical conductivity (41% IACS). The as-cast Al-3 vol. % TiB_2 nanocomposites

exhibit yield strength of 206.6 MPa, UTS of 219.6 MPa, tensile strain of 4.3% and electrical conductivity of 57.5% IACS (pure Al has yield strength of 35 MPa, UTS of 90 MPa, tensile strain of 12% and electrical conductivity of 62.5% IACS). We also observed an unusual ultra-fine grain (UFG) size, as small as 300 nm, in the ANEC samples under slow cooling. We believe that the significant mechanical property enhancements can be partially attributed to the existence of the UFG. Further investigations demonstrated that UFG can be achieved when nanoparticles are uniformly dispersed and distributed in the aluminum matrix (Chapter 7).

In summary, analytical, numerical and experimental approaches have been established to significantly advance fundamental understanding of polymeric and metallic matrix nanocomposites, in particular the effect of metal-like ceramics on mechanical and electrical properties of lightweight metals. This study has demonstrated scalable production of multi-functional metal and polymer matrix nanocomposites. Metal-like ceramic nanoparticles can significantly enhance the mechanical properties of metal matrix while retaining good electrical properties.

The dissertation of Abdolreza Javadi is approved.

Jenn-Ming Yang

Yong Chen

Yongjie Hu

Xiaochun Li, Committee Chair

University of California, Los Angeles

2018

I gladly dedicate this work to my parents, my brother, and my sister for their unconditional love. I also very much appreciate my girlfriend, Elaheh Alizadeh-Birjandi, for her continuous help and support during this journey.

TABLE OF CONTENTS

TABLE OF FIGURES

LIST OF TABLES

ACKNOWLEDGEMENTS

I would like to sincerely thank Professor Xiaochun Li for his outstanding support and continuous guidance, without which this would not be possible. His diligent involvement, systematic supervision, and his wealth of creativity benefited my Ph.D. study and for my future career.

I would also like to acknowledge Professor Jenn-Ming Yang, Professor Yong Chen, and Professor Yongjie Hu for serving in my doctoral committee. I sincerely appreciate their valuable inputs and feedback for my research.

And last but not the least, I would like to acknowledge all of my colleagues at Scifacturing research group.

VIATE

2014, M.S., Mechanical Engineering, University of Wisconsin-Madison, USA

2012, B.S., Mechanical Engineering, University of Wisconsin-Milwaukee, USA

JOURNAL PAPERS

- **Javadi, A.**, Pan, S., & Li, X (2018). Scalable Manufacturing of Ultra-strong Mg Nanocomposites. *Manufacturing Letters*.
- **Javadi, A.**, Pan, S., & Li, X (2018). Fabrication of High Strength Al nanocomposites with Populous TiB_2 Nanoparticles. *Procedia Manufacturing*.
- **Javadi, A.**, Zhao, J., Cao, C., Pozuelo, M., Yang, Y., Hwang, I., & Li, X. (2017). Stretching Micro Metal Particles into Uniformly Dispersed and Sized Nanoparticles in Polymer. *Scientific Reports (Nature)*, *7*.
- **Javadi, A.,** Cao, C., & Li, X. (2017). Manufacturing of Al-TiB2 Nanocomposites by Flux-Assisted Liquid State Processing. *Procedia Manufacturing*, *10*, 531-535.
- Cao, C., Liu, W., **Javadi, A.**, Ling, H., & Li, X. (2017). Scalable manufacturing of 10 nm TiC nanoparticles through molten salt reaction. *Procedia Manufacturing*, 10, 634-640.
- Zhao, J., **Javadi, A.**, Lin, T. C., Hwang, I., Yang, Y., Guan, Z., & Li, X. (2016). Scalable Manufacturing of Metal Nanoparticles by Thermal Fiber Drawing. *Journal of Micro and Nano-Manufacturing*, *4*(4), 041002.
- Lin, T. C., Zhao, J., Cao, C., **Javadi, A.**, Yang, Y., Hwang, I., & Li, X. (2016). Fabrication of Metal–Polymer Nanocomposites by In-Fiber Instability. *Journal of Micro and Nano-Manufacturing*, *4*(4), 041008.
- Mutyala, M. S. K., **Javadi, A.**, Zhao, J., Lin, T. C., Tang, W., & Li, X. (2015). Scalable Platform for Batch Fabrication of Micro/Nano Devices on Engineering Substrates of Arbitrary Shapes and Sizes. *Procedia Manufacturing*, *1*, 205-215.
- Javadi, A., Zheng, Q., Payen, F., **Javadi, A.**, Altin, Y., Cai, Z. & Gong, S. (2013). Polyvinyl alcohol-cellulose nanofibrils-graphene oxide hybrid organic aerogels. *ACS applied materials & interfaces*, *5*(13), 5969-5975.

CONFERENCE PAPERS

- **Javadi, A.**, Cao, C., Xu, J., & Li, X. "Solidification Processing of Super Metals Containing Self-Dispersed Nanoparticles" the 6th Decennial International Conference on Solidification Processing, London, England.
- Zhao, J., **Javadi**, **A.**, Lin, T.C., Hwang, I., Yang, Y., Guan, Z., and Li, X. "Scalable Manufacturing of Metal Nanoparticles by Thermal Fiber Drawing" *Proceeding of the ASME International Manufacturing Science and Engineering Conference,* Blacksburg, VA, 2016.
- Lin, T.C., Zhao, J., **Javadi**, **A.**, and Li, X. "Feasibility Study on Thermal Drawing of Polymer Fibers Containing Micro/Nano Metal Wires" *Proceeding of International Symposium on Flexible Automation,* Cleveland, OH, 2016.
- **Javadi**, **A.**, Pillai, K. M., and Sabo, R. "An Experimental Estimation of Liquid Absorption Coefficient for Cellulose Nano-fiber Films" *Proceeding of 11th International Conference on Flow Processes in Composite Materials,* Auckland, New Zealand, 2012.
- Masoodi, R., **Javadi**, **A.**, Pillai, K.M. "Investigation of Resin Flow in Woven (dual-scale) Jute Fabrics Through the Two-Color Experiment" In *11th International Conference on Flow Processes in Composite Materials,* Auckland, New Zealand, 2012.
- Masoodi, R., **Javadi**, **A.**, Pillai, K.M., and Sabo, R. "An Experimental Study on Swelling of Cellulose Nano-fiber Films in Epoxy, Resin, and Water" *Proceeding of Society for the Advancement of Material and Process Engineering,* Long Beach, CA, 2011.
- Masoodi, R., Hajjar, R.E., Pillai, K.M., **Javadi**, **A.**, and Sabo, R. "An Experimental Study on Cracking Propagation in Green Composites Made from Cellulose Nano-fiber and Epoxy" *Proceeding of Society for the Advancement of Material and Process Engineering*, Long Beach, CA, 2011.

PATENTS

- Scalable Method of Producing Polymer Metal Nanocomposite Materials (US2017/036432).
- Facile Synthesis of 10 nm High Purity Titanium Diboride Nanoparticles (provisional/ UCLA 2018-323-1).

CHAPTER 1. INTRODUCTION

1.1 Background and Motivation

Nanocomposites are class of hybrid materials consist of nanoscale elements as reinforcements and matrix. Nano scale elements are synthesized in various shapes and geometries with average sizes less than 100 nm in each dimension. Nanoparticles and nanofibers are two common nanoscale elements widely used as reinforcement in nanocomposite systems. Nanocomposite materials can be divided into three main category; namely, polymeric matrix nanocomposite (PMNC), metallic matrix nanocomposites (MMNC), and ceramic matrix nanocomposite (CMNC). PMNCs and MMNCs have been intensively studied over the past two decades as they offer significantly enhanced mechanical, electrical, thermal, and chemical properties [1-6]. MMNC materials are capable of offering mechanical properties than cannot be achieved by conventional strengthening mechanisms such as elemental alloying and thermomechanical processing [7].

Lightweight metals have been widely used for diverse range of practical applications in various industries, including but not limited to, aerospace, automotive, railroad, naval, electronic, packaging and etc. In lightweight metal family, aluminum, the second-most-commonly used structural metal, has been widely applied for many structural and functional applications. Aluminum and its alloy have been widely utilized in electrical transmission and distribution lines across the world. It is estimated that annual electricity transmission and distribution losses are about 5% in the United States [8]. In addition, the tower cost for such high density electrical cables (due to steel core as reinforcement) can be significant. Therefore, the electrical transmission line is one of the most promising directions for research and development where nanocomposites can

offer exciting promises to significantly improve the mechanical properties of electrical conductors while maintaining good electrical properties.

Magnesium, the third-most-commonly used structural metal, is another element of interests in lightweight metal family. Magnesium, the low density metal, has been broadly applied in industries such as automotive, electronics and biomedical. Similar to aluminum, traditional magnesium synthesis and processing methods have reach their fundamental limitations in terms of mechanical property improvements. Therefore, a new approach, metal matrix nanocomposites, can be a promising alternatives to procured bulk magnesium with significantly improved mechanical properties.

Additive manufacturing (AM) or three dimensional (3-D) printing of metallic systems have drawn significant attentions by both industries and academia in recent years. Manufacturing of functional or structural parts layer-by-layer have provided an invaluable design freedom for rapid production. The significant reduction of time from conceptual design (e.g. three dimensional modeling)-to-manufacturing offer extraordinary promises for fast development of metals for diverse practical applications. Metal-based 3D printing has shown an unexpected growth in industries, including but not limited to, aerospace, defense, navy, tooling, biomedical, and automotive industries. Currently, more than 5500 alloy systems used in daily life cannot be 3D printed [8, 9]. In addition, 3D printing of metallic systems such as pure Al and it alloys are not readily available for many practical applications due poor solidification behavior and limited mechanical properties. Therefore, there is a strong need for the development of the unique microscale metallic superstructures to be used in 3D printing to improve poor solidification behavior, and more importantly, mechanical properties of the final parts.

1.2 Overarching Goals and Specific Research Objectives

The overarching goas of this study are: (a) to produce multi-functional polymer-metal nanocomposites with a uniform dispersion and distribution of metallic nanoscale elements, (b) to significantly advance the fundamental understating of a suitable nanoparticles interaction in molten metal, (c) to introduce a science-guided novel class of aluminum and magnesium nanocomposites for practical applications such as electrical transmission lines, (d) to fundamentally understand, design, and produce metal-nanoparticle systems with desired mechanical and electrical properties, and (e) to develop a scalable, simple, and novel method to synthesize nanoscale reinforcements. More specifically, the research objective is to understand the exact influence of nanoparticles on different lightweight matrices, which includes nanoparticles interaction in molten metals, nanoparticles impact on mechanical and electrical properties, and the influence of the nanoparticles on unclean of the primary matrix phase during solidifications.

Polymer-Matrix Nanocomposites

Polymers, both in synthetic and natural forms play a crucial and ubiquitous role in our daily life due to their good mechanical and chemical properties. However, polymers do not offer promising mechanical, electrical and thermal properties. Reinforcing polymers with glass fibers or carbon fibers have been utilized for many structural applications such as commercial aircrafts. Significant improvements in mechanical, electrical and thermal properties of polymers allow these low density materials to serve new industries. Incorporating suitable nanoscale elements in polymeric materials result in excellent mechanical and functional properties. Polymer-metal nanocomposites have drawn significant attention within the past two decades due to their excellent physicochemical properties for functional application [10-13]. PMNCs have many potential

applications such as transparent electrodes [14-16], electromagnetic interface (EMI) shielding, electrostatic dissipation (EDS) [17], plasmonic metamaterial electromagnetic wave absorbers for solar cells [18-20] and antimicrobial polymers [21].

For conductive polymers to be used as EMI or EDS, moderate conductivities are required ($\sigma = 10^{-4} – 10^{0}$ Sm^{-1} for EDS and $\sigma > 1$ Sm^{-1} for EMI) [22, 23]. Uniform dispersion of conducting particles such as carbon nanotubes (CNTs), metal nanowires in thin section polymer can lead to anisotropic conduction nanocomposites. CNT-based PMNCs are reported to have electrical conductivities between 10^{-5} and 10^{3} Sm^{-1} [24]. However PMNCs can be significantly useful for the aforementioned applications, the fabrication of PMNCs suffers from major challenges such as uniform dispersion of metallic phase and scalability [17].

PMNCs fabrication methods can be divided into two main categories: extrinsic and intrinsic [11]. In extrinsic methods, nanoparticles are dispersed (i.e. shear forces or ultrasonic vibration) separately in an organic chemical solvent such as ethanol and then incorporated into the polymer matrix during processing such as extrusion or spin coating [17]. In this approach, the surface of the metal nanoparticles are often functionalized or passivated to promote the dispersion and distributions in polymer matrix. Physical dispersion methods are used to produce polymer nanocomposite films and are also categorized as extrinsic which provide homogeneous distribution and distribution. However, it is limited to production of thin films. In intrinsic methods, metal nanoparticles are formed in-situ during processing. Intrinsic methods can produce bulk polymer nanocomposites with improved dispersion, however these methods are more complex and less cost-effective. Therefore, there is a strong demand for scalable fabrication of PMNCs with uniform dispersion and distribution of metallic phase.

Metal Matrix Nanocomposites

Metal matrix nanocomposites are class of materials that the matrix is essentially pure metal or alloy and the reinforcement can be different ceramic or organic compounds. There are several methods to manufacture MMNCs such as wet chemical [25, 26], solid-state processing (i.e. powder metallurgy), liquid-state methods (electroplating and electroforming, pressure infiltration, stir casting, squeeze casting, spray deposition, reactive processing, and solidification) [27-33], semi-solid state processing (e.g. semi-solid powder processing) [34-36], vapor deposition (e.g. physical vapor deposition), electrodeposition [37-43], friction stir welding [44, 45], mechanical alloying [46-57], and laser cladding [51, 58-63].

Solidification processing is of a great potential for an economical manufacturing of bulk nanocomposites specifically for those with crystalline materials as matrix. However, achieving a uniform dispersion of nanoscale reinforcements (e.g. nanoparticles) within crystalline matrix is of a great challenge [7]. The final distribution of nanoparticles depends on incorporation, dispersion in molten metal, and the pushing effect of nanoparticles during solidification. Many researchers have strived to resolve the pushing of the nanoparticles to the grain boundaries during solidification [64]. It is still a grand challenge to achieve uniform dispersion of nanoparticles in metal matrix due to a strong van der Waals (vdW) attraction forces that exist between nanoparticles. Also, the poor wettability between ceramic nanoparticles and molten metal lead to cluster formation. Other factors such as contaminations and air entrapments reduce wettability between nanoparticles and molten matrix which results in poor incorporation efficiency and dispersion [7].

Aluminum Electrical Conductors

Copper (Cu) and silver (Ag) are best known electrical conducting metals, however they have high density. And more importantly, they are expensive for applications in overhead electrical direct current (DC) transmission and distribution lines. On the other hand, pure aluminum, with a low electrical resistivity (2.63 μΩ·cm, 64% international annealed copper standard/IACS) at room temperature, is a low cost, lightweight metal with a one-third density of Ag and Cu. The aforementioned characteristics made aluminum a promising candidate for overhead electrical DC transmission lines. Aluminum conductors have been widely used as electrical conductors, especially as wires and cable.

Aluminum conductor steel reinforced (ACSR) is the most common electrical conductor cable system used for high voltage DC transmission lines [35, 65, 66]. ACSR consist of Al1350-H19 strands responsible for electrical conductivity and high strength steel wire core which carries the weight of the whole cable. ACSR suffers from high electrical resistivity, high density, and high temperature stability. ACSR overhead electrical cable in its current form has remained unchanged for more than 100 years, aside from minor changes in the alloys and construction of the product. It is estimated that annual electricity transmission and distribution losses is about 5% in the United States [67] which can be translated to more than $24B loss. Therefore, reducing this amount of electricity loss by a novel and transformative electrical transmission system (i.e. developing new electrical conductors) with improved mechanical and electrical properties is vital. In addition, since ACSR cables have high density, they require more tower construction which increases the cost of the transmission lines [35]. The rising demand for efficient electrical power transmission lines and increasing cost of the land acquisition for transmission corridors have pressed for development of the new generation of electrical cables.

Traditional strengthening mechanism such as sever plastic deformation (e.g. cold drawing and equal-channel angular pressing) [68-71], high-pressure torsion [72-74], accumulated roll bonding [75-77], solid solution treatment [78-81], grain boundary strengthening (Hall-Petch effect) [82], dislocation strengthening, precipitation strengthening [83], and solid-solution strengthening [84] have reached their fundamental limitations. For instance, the strengthening phases produced via precipitation hardening become unstable at elevate operating temperature.

Several material systems have been proposed to produced aluminum electrical wire via powder metallurgy method such as Al-Nb [34], Al-Ti [85], Al-Mg [86], Al-Sn [87], and Al-Ca [35]. Although these solutions demonstrate improved strength, they suffer from poor electrical conductivity, and more importantly, small scale production (e.g. powder metallurgy). Metal matrix nanocomposites is a class of hybrid material which offer unusual properties [7]. Thus, incorporating suitable nanoparticles into aluminum metal matrix can be a viable approach to produce scalable aluminum electrical conductors suitable for high voltage DC transmission lines. Incorporating metal-like nanoparticles into Al matrix enhances the mechanical strength while retaining good electrical conductivity.

In the United States, it is widely estimated that there will be an increase of at least 20% demand for electricity in the next ten years. In addition, economic development and business expansion requires reliable electrical transmission lines. This increase in demand has created congestion on the current power transmission lines. Therefore, it is crucial to modify and upgrade the existing power transmission lines to meet the increase in national electrical power demand. Nanocomposite approach is an exciting opportunity to produce Al nanocomposites which can offer mechanical and electrical properties beyond the limitations of traditional manufacturing methods.

1.3 Outline

- Chapter 2 reviews the nanocomposites in research and developments.
- Chapter 3 introduces a scalable yet novel approach to produce polymer-metal nanocomposites.
- Chapter 4 shows a scalable synthesis method to produce metal-like ceramic nanoparticles to be utilized as nano-reinforcements.
- Chapter 5 introduces an innovative approach to mass produce metal nanocomposite microparticles.
- Chapter 6 describes nanoparticles interaction in magnesium matrix and production of magnesium nanocomposites with high volume fraction of nanoparticles for significantly improved Vickers hardness.
- Chapter 7 introduces theoretical and experimental studies on the effect of nanoparticles on mechanical strength and electrical conductivity of aluminum matrix nanocomposites.
- Chapter 8 draws conclusions for this dissertation.
- Chapter 9 focuses on the recommended work for future.

CHAPTER 2. LITERATURE REVIEW

Nanocomposites are class of multi-phase solid materials consist of matrix and reinforcements. Matrix phase can be in form of metallic, polymeric and ceramic. The reinforcement phase requires to be less than 100 nm in size and well-dispersed in matrix medium. The reinforcing phase can be in form of particulates, fibrous, tubes, flakes, filler, and etc. Nanocomposite materials offer promising physical, chemical, mechanical, and electrical properties for a broad range of applications in aerospace, automotive, naval, air force, and army.

2.1 Polymer Matrix Nanocomposites

2.1.1 Polymer-Metal Nanocomposites for Functional and Structural Applications

PMNCs with highly ordered nano-element are complex materials with interesting morphological behavior due to the variation in composition, structure and physiochemical properties. Conductive PMNCs are extensively studied for novel applications such as chemical and biological sensors, photovoltaic devices, flexible and transparent electronics, printable circuit wiring, variable resistors, and actuators [17].

Several approaches has been investigated to unfirmly disperse CNT (due to high electrical-current-carrying capacity of CNT, about 1000 higher than copper wire) into polymer matrices such as direct feeding, modification of CNTs or the polymer, and use of the third component [64]. Direct feeding was used by *Sandler et al.* to fabricate conducting PMNCs. First, catalytically grown multi-walled CNTs (MWCNTs) were dispersed in ethanol by sonication. Then, epoxy resin were added to the mixture while stirring. A solvent was then added to the mixture to reduce the viscosity of the mixture. Upon achieving desired dispersion MWCNTs in epoxy resin the solvent was evaporated and hardener was added to completely capture the MWCNTs. Conductivity of the

epoxy resin-MWCNT was increased compare to polymer-carbon black composites. The conductivity of the epoxy resin-MWCNT was reported to be 10^{-1} S/m [64].

Kang et al. fabricated a multilayered nanocomposite membrane from layer-by-layer assembled polymers and single walled CNTs (SWCNTs) with combination of top-down and bottom-up approaches. Poly allylamine hydrochloride (PAH) and poly sodium 4-styrenesulfonate (PSS) were used as cationic and the anionic polymers, respectively. Spin coating (with 4000 rpm and for 20 second) was utilized to form different layers of PSS and PAH. Functionalized SWCNTs (carboxylic/COOH acid group) was dispersed in DMF (N, N-dimethylformamide) solvent, and was spin coated on the substrate. This layer was sandwiched between PSS and PAH layers. COOH group on the SWCNT surfaces result in strong electrostatic interaction with amine group on the positively charged PAH molecular surfaces. These repulsive forces overcome vdW attractions, enabling well-dispersion of SWCNTs in substrate. Nanomembrane fabrication began with 200 nm thick LPCVD (low pressure chemical vapor deposition) silicon nitride deposition onto a silicon (Si) substrate. Followed by pattering backside etched holes. 40 nm Ti film was sputtered after backside bulk etching. The bottom side of the polymeric Spin coating was used to deposit SWCNTS network. Shadow masking was used to form a metal electrode. It was shown the electrical conductivity of the nano-membrane can be tuned by controlling the density of the SWCNT interlayer [88].

2.1.2 Dispersion of Metallic Phase in Polymer Matrix

Many approaches have been reported to effectively disperse nano-elements in polymer matrices. Uniform dispersion of the conductive nano-elements in polymer matrices are desired to achieve PMNCs with exceptional mechanical and functional properties. Dispersion approaches can be classified into kinetic and thermodynamic.

In kinetic methods, essentially an external energy source such as shear force or ultrasound vibration is used to momentarily disperse the nano-elements. Solution blending, melt blending, and in-situ polymerization are the most comment approaches that fall into this category. In this method, nano-elements are disperse in a solvent medium (e.g. using ultrasonication) and then mixed with a desired matrix. Solvent is then evaporated to realize polymer matrix nanocomposites. A highly volatile solvent that expels rapidly can improve dispersion to a great extent [89]. Another approach is to mix the polymer and nano-element at high temperatures using high shear forces. This approach is so called, melt blending. Since the viscosity of the polymer matrix is high the dispersion quality is considered to be lower than the solution blending technique [90]. In the in-situ approach, nano-element is dispersed in a monomer. The monomer is then polymerized with a hardener. This approach is commonly used for epoxy-based nanocomposites [91].

In thermodynamic approaches, chemical additives are used to form covalent (or noncovalent) bond between nano-element and matrix medium. The most common approach contains modification of the surface of the nano-elements to promote compatibility with the matrix and reduce nano-elements attraction vdW forces. Functionalization of CNTs by forming covalent chemical bonding with another chemical elements is commonly used. However, this technique suffers from a major disadvantages which is the disruption of π conjugation in the CNTs. This would lessen the electrical conductivity of CNTs due to electron scattering at the functionalization sites [92].

2.2 Metal Matrix Nanocomposites

In recent century, the demand for lightweight metals with significantly improved properties are continuously growing. These high performance materials have the potential to improve energy

efficiency and system performance in application such as aerospace, automobile, and defense. Among the abundant materials on earth, Al and Mg are of a great potential to be further engineered for such applications. However, achieving a uniform dispersion of the nano-reinforcements in metal matrix is of a significant factor to obtain superior properties [7].

For the first time, *Chen et al.* achieved uniform dispersion of silicon carbide (SiC) nanoparticles in Mg-zinc (Zn) matrix (Figure 1). Mg6Zn-1 vol. % SiC was first fabricated by ultrasonic assisted casting where one volume percent (vol. %) of SiC nanoparticles were dispersed by ultrasonic processing (with 20 kHz and a peak-to-peak amplitude of 60 μm) at 700 °C. The SiC nanoparticles were then concentrated by evaporation of Mg and Zn form the Mg6Zn-1 vol. % SiC sample (at 6 Torr in a vacuum furnace) and slow cooling to achieve 14 vol. % SiC in Mg2Zn matrix. Figure 1a and Figure 1b show SEM images of Mg2Zn-14 vol. % SiC samples.

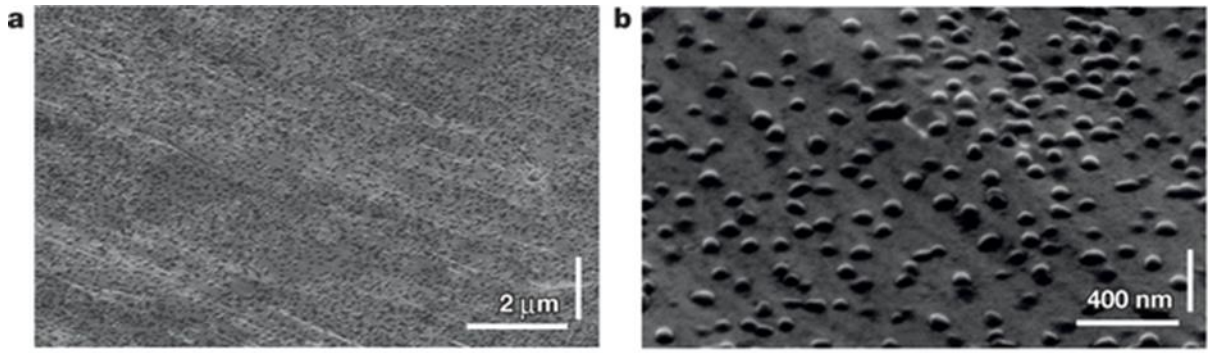

Figure 1: (a) and (b) SEM images of the Mg2Zn-14 vol. % SiC sample acquired at a 52 °C tilt angle and at different magnifications showing the uniform distribution and dispersion of SiC nanoparticles in the Mg-Zn matrix [7].

Young's modulus of the Mg2Zn-14 vol. % SiC sample was reported 86 ± 5 GPa which is drastically greater than Mg2Zn (44 ± 5 GPa). This enhancement was attributed to the strong interfacial bonding between SiC nanoparticles and the Mg matrix. Microcompression tests on the micropillars (prepared from Mg2Zn-14 vol. % SiC sample) showed a yield strength of 716 ± 38

MPa. *Chen et al.* obtained a yield strength of 123 ± 17 MPa for Mg2Zn-14 vol. % SiC sample at 400 ºC [7].

2.2.1 Al Alloying Metal Matrix Composites (AAMMCs)

Goujon et al. studied Al alloy 5000 reinforced nanocomposites with various loading of aluminum nitride (AlN) nanoparticles. 5000 Al alloy powders and various volume percent of AlN (0-30 vol. %) powder were cryo-milled. The prepared mixed powders were cold compressed at 180 MPa in a steel can and sintered at 120 MPa under vacuum to form a billet. The billet was then degassed for 3 hours at 503 K to minimize the moisture content. It was shown that this technique result in AAMNCs with a stable microstructure [93].

Kubota et al. investigated the additional of AlB_2 and MgB_2 in Al matrix to produce AAMMCs. Pure Al powders (with average dimeter of 100 μm) and AlB_2 (with average dimeter of 74 μm) or Mg B_2 (with average dimeter of 149 μm) were mechanically alloyed. The mixed powder were milled with additional of stearic acid ($C_{17}H_{35}COOH$). Various milling time was used to study the impact of the milling time on final particle size. 620 MPa and 846 MPa compressive stress were achieve for $Al_{85}(AlB_2)_{15}$ and $Al_{85}(MgB_2)_{15}$, respectively [48].

Property enhancement of Al-niobium (Nb) MMCs were investigated by *Thieme et al*. Al-20 vol. % Nb AAMMCs were produced by metal-metal deformation process. Al and Nb powders (micron size powders) were blended to obtain a homogeneous powder mixture. The mixture was poured into Cu cans and compacted to 73% density. The billet were consolidated to 100% density at room temperature (under compression). These billets were extruded at various deformation true strain, $\eta = \ln(A_i/A_f)$, where A_i and A_f are the initial and final transverse area of the specimen, respectively. After initial extrusion (η=3.1), Cu was removed by etching in nitric acid (HNO_3). An ultimate tensile strength (UTS) of 1030 MPa (at η=11.1) was reported for Al-20 vol. % Nb MMC

at room temperature. At higher strain, UTS of AAMMC exceeds the UTS calculated with the rule of mixtures, this indicates the dependence of the UTS on deformation strain. Reported value is 2.1 times greater than the UTS estimated based on the rule of mixtures. 4.4 μΩ·cm electrical resistivity (at η=10.2) was reported for Al-20 vol. % Nb AAMMC (with 728 MPa UTS) which is substantially higher than pure Al electrical resistivity (2.63 μΩ·cm). Figure 2 shows the SEM micrograph of the Al-20 vol. % Nb (η =6.2) [34] MMCs. The Nb phase forms a long and continuous ribbon shape with a fair distribution in Al matrix (Figure 2).

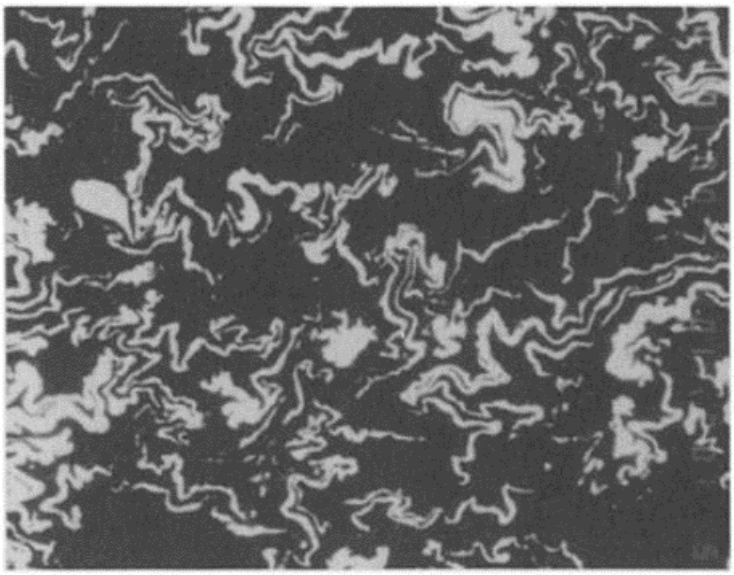

Figure 2: A SEM micrograph demonstrating cross section of the Al-20% Nb at η =6.2 [34].

Russel et al. produced Al-20 vol. % Titanium (Ti) AAMMCs by powder metallurgy followed by axisymmetric deformation processing. Al powder (with 45-75 μm size) and Ti powder (with 150 μm maximum size) were blended at room temperature. The well-mixed powders were cold isostatically pressed (CIP'ed) at 14 MPa to form a compact powder (80 vol. % Al and 20 vol. %Ti). The compacted powder were loaded into a Cu can which was vacuumed and sealed with electron beam weld to form a pellet [85]. The pellet was heated for one hour in a furnace at 535 K and extruded through a heated 13 mm diameter die followed by water quenching. The Cu layer

was then etched with HNO_3. At η=2.5, Ti particles started to form ribbon shape filament. Further deformation to a true strain of 13.9 caused the Ti filament to become sub-micrometer in size within Al matrix, achieving 890 MPa UTS and 4.3 μΩ·cm electrical resistivity. The continued deformation processing of Al-20 vol. %Ti leads to finer microstructure of Al-Ti AAMMC. As the number of deformation cycle increases, η increases, which leads to increase in strength. *Russel et al.* reported that the achieved UTS and electrical resistivity did not changed by a 24 hour annealing at 473 K [85]. Figure 3 shows SEM micrograph of the Al–20 vol. %Ti MMC.

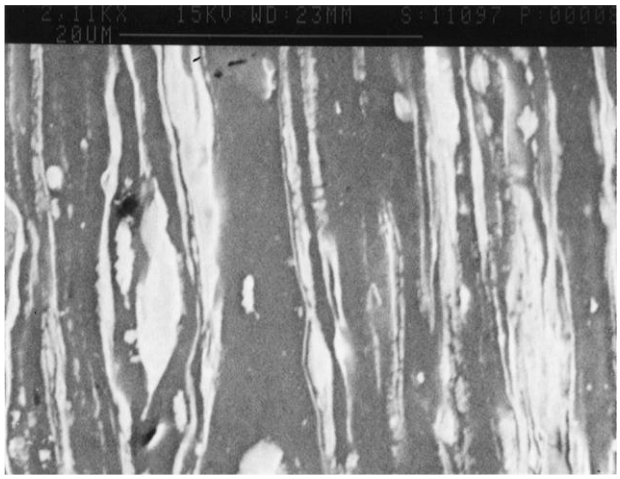

Figure 3: SEM micrograph of the Al–20 vol. %Ti at η=6.8 (longitudinal section) [85].

Xu et al. produced Al-20 vol. % Mg and Al-13 vol. % Mg MMC by cyclic axisymmetric deformation process. Micrometer size Al and Mg powders were mixed and CIP'ed to form billets. The multiple cycle of extrusion process were performed on the billet at room temperature. The deformation processing resulted in finer microstructure of Mg filaments embedded in Al matrix. Deformation process decreases both spacing and size of the Mg filaments in Al matrix. The Mg phase formed convoluted ribbon shape, these filaments are responsible for strengthening. An UTS of 420 MPa and 310 MPa was reported for Al-20 vol. % Mg (η=11.95) and Al-13 vol. % Mg MMC (η=11.28), respectively. Strengthening in Al-Mg MMC is attributed to Mg filaments acting as

barriers to dislocation movement. The electrical resistivity of the Al-20 vol. % Mg (η=11.95) and Al-13 vol. % Mg (η=11.28) MMC was reported 3.58 μΩ·cm and 3.27 μΩ·cm, respectively [86]. Figure 4 represents UTS as a function of deformation for Al-20Mg and Al-13Mg MMCs.

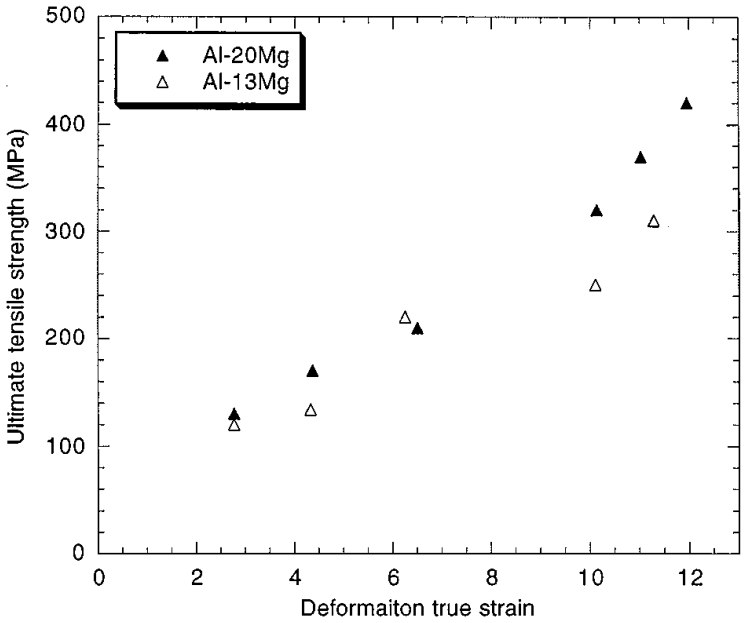

Figure 4: UTS as a function of deformation true strain for Al-20Mg and Al-13Mg [86].

Hernández et al. studied the microstructural and mechanical behavior of highly deformed Al- tin (Sn) alloys. Al-X vol. % Sn (X=3.96, 16.32, and 20.00) was prepared by conventional casting. Al- Sn ingots were then cold rolled at room temperature to achieve true strain deformation η=2.5, 3, 4, 5, 6, 6.25, and 6.5. Hernández reported that as Al-Sn composites are deformed the thickness and spacing between the second phase (Sn) decreases in a nonlinear manner. Also, there is quasi-linear relationship between UTS and second phase thickness. UTS of Al- 3.96 vol. % Sn and Al- 16.32 vol. % Sn increased by 41% at strain rate of η=6.5 compare with pure Al at same strain rate [87].

Tian et al. studied adding calcium (Ca) to pure Al as reinforcing medium to improve mechanical property while maintaining good electrical conductivity of Al-Ca composites. Al-9

vol. % Ca MMCs were produced by powder metallurgy method followed by mechanical deformations. Al (20 – 45 μm) and Ca powders (1.2 mm) were blended. The powder mixture was added to an Al alloy can (1100 commercial purity) and compacted at 6.55 to 8.76 MPa. Warm extrusion at 285 °C was performed to extrude the compacted powders. Tian proposed that Al-20 vol. % Ca MMNCs can have an estimate UTS of 660 MPa if Ca filaments with average size of 200 nm are achieved. Figure 5a shows back-scattering SEM image of the Al–9 vol. % Ca at η = 6.27. Al_2Ca compounds were detected by x-ray diffraction (XRD) study (Figure 5b).

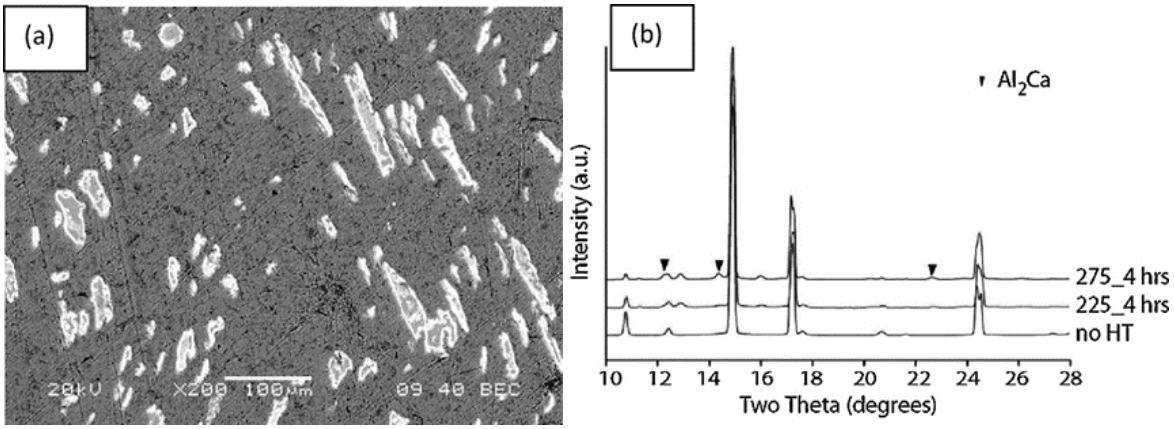

Figure 5: (a) Back-scattered electron SEM micrograph of transverse section of Al–9 vol.% Ca at η = 6.27 after heat treatment at 325 ºC for 1 h, and (b) X-ray diffraction results of specimens at η = 6.27 after different heat treatment [35].

The electrical conductivity of the Al- 9 vol. % Ca (with η=8.55) after heat treatment at 300 °C for various times showed that as the heat treating time increases, the electrical conductivity of the composites decrease (Table 1). This decrement is attributed to the formation of the Al_2Ca intermetallic compound at the interfaces which increase electron scattering effect. Pure Al electrical conductivity is reported to be 38 $(\mu\Omega\ m)^{-1}$ [35].

Table 1: The room temperature electrical conductivity of Al-9 vol. % Ca at η=8.55 after various heat treatment times at 300 C [35].

Heat treatment time (min) at 300 °C	Electrical conductivity $(\mu\Omega\ m)^{-1}$ at 22 °C
0	36.6
5	36.6
15	34.8
30	34.8
60	33.33
180	33.3
720	33.3

The low electrical resistivity of Al-9 vol. % Ca is due to the nano-scale phase of both pure Al and Ca acting as parallel conductive path to conduct electrons through wire axis. Al-Ca MMC composite is prone to corrosion due to high reactivity of Ca. It was reported that Ca filaments exposed to air (on the outer surface of the sample) corrode rapidly [35].

2.2.2 Al Metal Matrix Nanocomposites (AMMCs)

The demand for high strength, lightweight, excellent electrical conductivity, and excellent thermal stability electrical conductors have significantly increased in past decades. Metal Matrix Nanocomposites (MMNCs) offer excellent mechanical, electrical, chemical, and thermal properties (depending on reinforcing medium) while being lightweight. Al MMNCs can be promising candidate due to low density and high ductility of the Al matrix. These factors made Al MMNCs of a great potential for applications where high strength and electrical conductivity is required.

The invention of carbon nanotubes in 1990s have opened up unprecedented research opportunities in the area of nanotechnology. Laha studied Al-Si alloy reinforced by 10 weight percent (wt. %) MWCNTs nanocomposites (Al-Si-10 wt. % CNT). Gas atomized Al-Si (15-45 μm) powders were used as matrix medium. Al-Si and CNT were blended and ball milled for 48 hours [94]. The molten particles were deposited on rotating 6061 Al mandrel to produce cylindrical nanocomposites by plasma spray forming. Although the elastic modulus of the Al-Si-10 wt. % CNT nanocomposites were increased by 78% compare to pure Al-Si, the strain was decrease by 41% [94]. Figure 6 shows the hierarchal modes of tensile fracture in Al-Si-10 wt. % CNT nanocomposites.

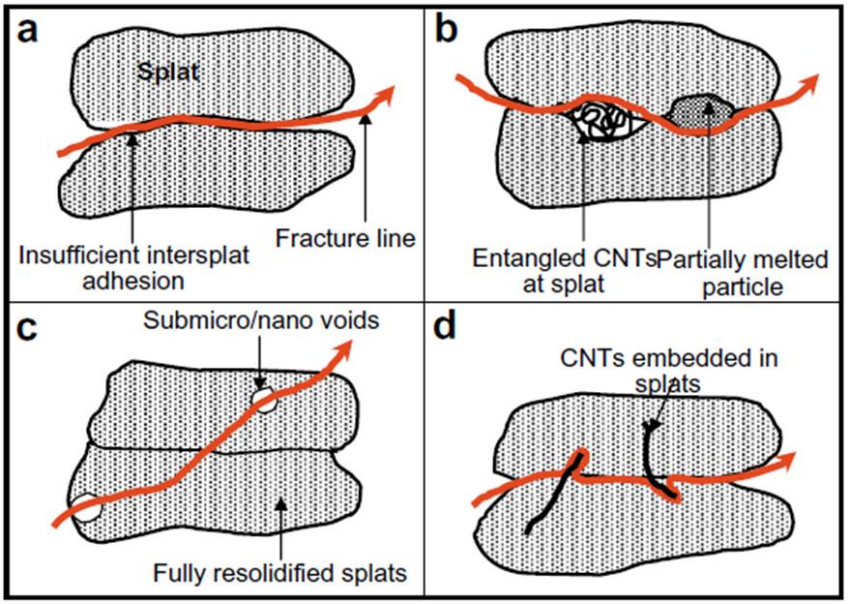

Figure 6: Hierarchical modes of tensile fracture in thermally sprayed nanocomposite: (a) Fracture through weak intersplat boundary due to insufficient solidification at splat interfaces, (b) fracture through partially re-solidified splat boundary caused by entangled CNTs and partially melted particle, (c) intergranular fracture facilitated by micro voids, and (d) fracture by CNT pull out [94].

Wu et al. used MWCNT as reinforcing medium to improve Al6061 mechanical properties. MWCNT (20-50 nm diameter and 5 μm in length) and Al6061 powder (5-23 μm size) were

mechanically alloyed by high energy ball milling process. To consolidate the mixture, sample was heated up to 640 °C for 30 min. Utilizing ball milling, significant CNT breakage occurred which lead to better dispersion of the CNT nanoparticles in Al6061 matrix. By adding 1 wt. % CNT to Al6061 the average hardness of the campsite increased by 28%. It was reported that as ball milling processing time increases to 3 hours, the length of the CNTs decreases from 5 μm to 1 μm. However, longer processing time increases the reaction between CNT and liquid matrix due to formation of the Al_4C_3 compound. Also, longer ball milling time results in ductility reduction [36]. Figure 7e, Figure 7f, and Figure 7g show Al6061 alloy powders mechanically alloyed for various time.

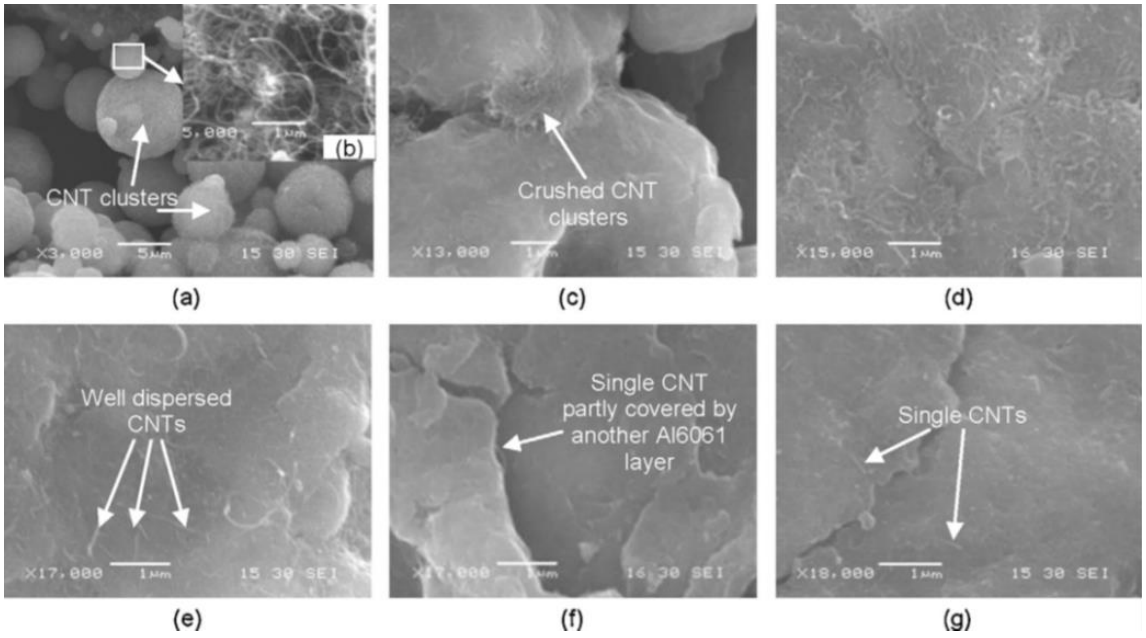

Figure 7: CNTs and mechanically alloyed Al6061 powder and CNTs: (a) and (b) are images of as-received CNTs, and (c)–(g) are Al6061 powder and CNTs mechanically alloyed for (c) 10 min, (d) 0.5 h, (e) 1 h, (f) 2 h and (g) 3 h, respectively [36].

Adding 10 wt. % B_4C nanocrystalline (NC) to Al5083 aluminum alloy can significantly increase the yield strength of the matrix. B_4C and Al5083 NC powders were fabricate by cryomilling. The product was well-mixed with un-milled coarse grain (CG) Al5083 to form

homogeneous mixed powders. The mixed powders (10 wt. % B_4C, 50 wt. % CG 5083 Al and the balance NC 5083 Al) were consolidated by CIP. Consolidated billet was extruded at 798 °K. Compression test study samples were prepared after annealing at 723 K for 2 hours. 50 wt. % Al5083 NC-50 wt. % Al5083 CG composite (without B_4C NC) was prepared as a reference. Compression test revealed that Al5083- 10 wt. % B_4C composites can have yield strength up 1058 MPa with low ductility (0.8%) at room temperature. The reference exhibit 504 yield strength with 14 % strain at room temperature [95].

2.2.3 Mg Metal Matrix Nanocomposites

Magnesium with a low density is the ninth abundant element on Earth. Aside from broad range of applications in biomedical industry (due to biocompatibility) [96] such as stent, it also has applications in aerospace [97], automotive [98] and electronic [99], defense [100]. However, the mechanical property of Mg needs to be improved to serve wider range of industries (e.g. transportation) where high strength-to-weight ratio is required. The aforementioned applications rely on manufacturing of Mg by traditional manufacturing processes such as elemental alloying and thermomechanical processing. For example, alloying Mg with other element followed by heat treatment can improve Mg strength, however the precipitates obtained from heat treatment would grow at elevated temperature which result in low mechanical strength [101]. These approaches have reached their fundamental limits in offering promising mechanical properties. Therefore, limiting the application of the high strength Mg at the elevated temperature.

MMNCs can be a potential alternative for traditional synthesis of bulk metallic materials [101]. MMNCs are class of materials where metallic matrix is reinforced with a nanoscale reinforcements. MMNCs can offer unconventional mechanical, physical, and thermal properties depending on the nanoscale reinforcements [7]. Nanoparticles can significantly improve strength

while maintaining or in some cases improving plasticity of metals [102, 103]. Several nanoparticle systems have been studied to reinforce Mg matrix. Nanoparticle systems such as oxides (e.g. alumina/Al_2O_3 and titanium dioxide/TiO_2), nitrides (boron nitride/BN, aluminum nitride/AlN, titanium nitride/TiN and zirconium nitride/ZrN), carbides (boron carbide/B_4C, silicon carbide/SiC, titanium carbide/TiC, and zirconium carbide/ZrC), and borides (titanium diboride/TiB_2 and zirconium boride/ZrB_2) [104]. Although new types of nanoparticles are explored to reinforce Mg matrix, the manufacturing of Mg nanocomposites with uniform dispersion nanoparticles remains a grand challenge. In fabrication side, many methods have then been employed to increase the nanoparticles incorporation efficiency. Solid phase processing (e.g. metallurgy) is of an appealing approach, since nanoscale reinforcements can be readily blended with the matrix at solid state. However, such a processing approach is suitable for small scale production [104, 105]. For liquid state processing of Mg nanocomposites, mechanical impellers or ultrasonic cavitation zone was utilized to disperse the nanoparticles in Mg matrix [105, 106]. However, these approaches are suitable to low volume fraction of nanoparticles and only effective in small scale. To overcome the high viscosity of molten Mg due high volume fraction of nanoparticles, squeeze casting is also been utilized to improve the incorporation efficiency. Mechanical shearing methods such as direct stirring during processing cause formation of magnesium oxide layer on the melt surface, and more importantly Mg burn once in contact with oxygen. High volume loading of nanoparticles into Mg matrix is of a great challenge. In addition, achieving uniformly dispersed and distributed nanoscale reinforcements into Mg matrix can significantly improve the strength of the Mg nanocomposites [107].

Many research endeavors have been dedicated to identify effective incorporation of nanoparticles into Mg matrix by various approaches such as mechanical shearing/stirring [108,

109], ultrasonic assisted [4, 106], salt-assisted [110, 111], spark plasma sintering [54] and powder metallurgy [112, 113]. However, it is extremely difficult to achieve uniform dispersion and distribution of nanoparticles in metallic matrix [114-117]. Mg is a challenging matrix for many of the aforesaid processes such as powder metallurgy as it can be dangerous. Manufacturing of bulk Mg nanocomposites is of a great challenge.

2.3 Aluminum Based Electrical Cables for Transmission Lines

In this section five important electrical cables will be introduced. The advantageous and disadvantageous of each cable system will be discussed in details.

2.3.1 Aluminum Conductor Steel Reinforced (ACSR)

ACSR cables consist of a strong steel core and annealed Al outer strands surrounding the core to conduct the current (Figure 8). ACSR has a high conductivity (≥ 61International Annealed Copper Standard, IACS) when transmitting AC due to the existence of the skin effect on the exterior surface of the Al strands [35]. Skin effect concentrates the transmitted current to the outer surface of the Al strands. However, it has moderate electrical conductivity in DC transmission line (due to poor electrical conductivity of the steel core). In ACSR, the steel core has poor conductivity (small conducting contribution) and promotes sag in long distance transmission lines. Al strands tensile strength is an important factor in ACSR cables, since at temperature above 75 °C the Al strands begin to soften. Hence, it is vital to develop Al conductor strands with high tensile strength while maintaining low electrical resistivity. Although ACSR cables have good strength, it suffers from the heavy steel core demanding for more tower constructions and transmission line installations.

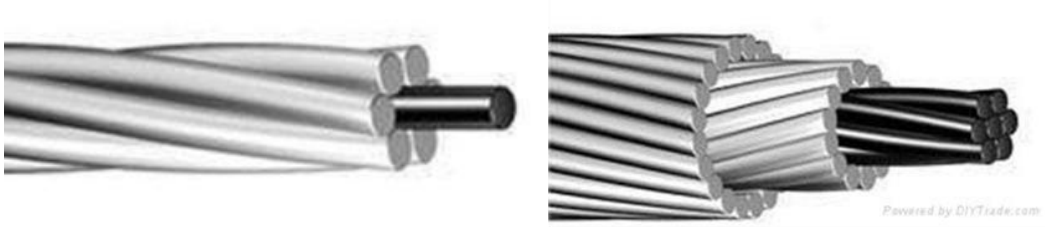

Figure 8: Schematic of the ACSR electrical cables (Black and gray wires show the cores and strands, respectively).

2.3.2 All Aluminum Alloy Conductor (AAAC)

AAAC cables are composed of high strength Al reinforced with Si and Mg, Iron (Fe), Cu, Manganese (Mn), Chromium (Cr), Zn, and Boron (B). AAAC cables have higher strength and less density (lighter) compare to ACSR [118]. Although AAAC have several advantageous over ACSR, the strengthening alloying elements reduce the electrical conductivity to 52.5-53 % IACS (pure Al exhibits electrical conductivity of 63-65% IACS) [118, 119]. In emergency overload situation, AAAC suffers from thermal fatigue due to its high coefficient of thermal expansion (CTE) [119].

2.3.3 Aluminum Conductor Alloy Reinforced (ACAR)

ACAR cables are made of Al 6201-T81 and Al1350-H19 strands. ACAR demonstrates excellent mechanical property while retaining reasonable electrical conductivity. It also offers promising corrosion resistance. Being able to adjust the relative number of 6201-T81 strands required for specific strength and electrical conductivity is a major drawback in ACAR [120]. Al alloys cost more than steel, and it becomes soft at elevated temperature (75 °C). However, In ACAR, thermal expansion and elastic modulus are nearly identical.

2.3.4 Aluminum Conductor Composite Reinforced (ACCR)

In 2003, 3M invented a new class of Al conductors, ACCR [121]. ACCR composed of continuous polycrystalline alumina (α-Al_2O_3) fibers (50 vol. %) as reinforcement (core) and pure

Al or Al-2 wt. % alloy as strands. ACCR displays high strength, excellent sag resistance, and high temperature performance (up to 240 °C). While the Al strands are responsible for conducting electricity, the composite core does not contribute to electrical conductivity. ACCR cables start to degrade irreversibly at about 240 °C [34]. ACCR cable have higher density (3.4 g/cm3) compare to pure Al (2.7 g/cm3) due to presence of alumina fibers. Alumina, a non-conductive, constitutes 50 vol. % of the ACCR. That is, 50 vol. % of the ACCR would not conduct electricity in DC transmission lines (not desirable). In addition, due to the large mismatch of CTE and elastic modulus between Al and alumina, ACCR is prone to thermal fatigue, spooling, and erection issues [35]. ACCR has an outstanding sag resistance at high temperature, however it costs nearly five times more than ACSR cables.

2.3.5 Aluminum Conductor Composite Core (ACCC)

ACCC was invented by CTC Cable Corporation [122]. ACCC cables consist of polymer matrix/carbon (and glass) fiber reinforced composite as a core and Al as strands. The polymer composite core has high tensile strength, low CTE and high temperature sag resistance. The large difference of CTE and elastic modulus between polymer composite core and Al strands surrounding the core are two major drawbacks attributed to ACCC cables [35]. ACCC cables have less energy efficiency in DC transmission lines compared to ACCR due to non-conductive polymer composite core. In order to increase the current carrying capacity of the ACCC wire, trapezoidal shape wires (TW) are utilized (Figure 9). Trapezoidal configuration adds 20-25% aluminum to the wire geometry, which would increase current carrying capacity by 8-10 % for DC transmission lines (compare to the same diameter conductors) [120].

http://archive.constantcontact.com/fs107/1110237241357/archive/1117923570236.html

Figure 9: An image of the aluminum conductor composite core/ trapezoidal wire (ACCC/TW).

Four commonly used Al conductor electrical cables and their properties are listed in Table 2. From Table 2 one can conclude that ACCC/TW has the best tensile strength and electrical conductivity. However, the degradation of polymer composite core at high temperature is a major challenge. Also in ACCC/TW systems, electron scattering significantly reduces the electrical conductivity [123].

Table 2: Comparison between four commonly used conductors [35].

Conductors	Density (g/cm^3)	Strength (MPa)	DC conductivity at 20 °C ($\mu\Omega\ m)^{-1}$	Elastic Modulus (GPa)
ACSR	3.43	304	28.1	85
AAAC	2.74	312	29.4	69
ACAR	2.74	251	31.7	69
ACCC/TW	2.612	345	34.8	57

2.4 Flux-Assisted Liquid State processing

2.4.1 In-situ Nanoparticle Synthesis in Matrix

Five vol. % TiB_2 nanoparticles was incorporated in Al-4.5Cu binary matrix. Commercial pure Al and Cu were used to prepare Al- 4.5Cu matrix. Potassium fluotitanate (K_2TiF_6) and potassium fluoborate (KBF_4) were used to synthesize the TiB_2 reinforcement phase. Magnesium fluoride (MgF_2) and Sodium hexafluoroaluminate (Na_3AlF_6) flux were used to assist the chemical reaction. First Al ingots were melted in a graphite crucible at 700 ºC and Cu ingots were added. Two salts and fluxes were mixed at solid state and gradually were added to the melt surface at 830 ºC (salts and fluxes were dehydrated at 300 ºC for 2 h). The reaction was held for 30 min at 830 ºC. Graphite blade was used to facilitate the stirring during reaction. Two stirring speed was examined, 360 and 540 rpm (blade position was inside the Al melt). Figure 10 shows the experimental set-up used in this study [124]. The in-situ synthesis of the TiB_2 nanoparticles occurs through aluminothermic reaction of a complex potassium fluoride molten salt mixture.

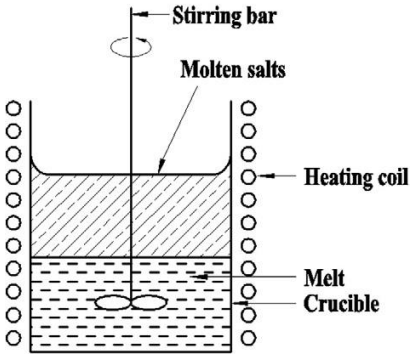

Figure 10: Schematic of mechanical stirring [124].

Estruga et al. synthesized TiB_2 nanoparticles with an average size of 20 nm using ultrasonic assisted salt synthesis method. K_2TiF_6, KBF_4, and CaF_2 were mixed and manually grinded for 10 min. The powder mixture was dehydrated at 120 ºC for 1h to eliminate moisture. Al1350 Al alloy

was molten in a graphite crucible under Ar gas flow protection. Once molten Al was ready, the ultrasonic probe was inserted in the molten Al and the dehydrated reagent mixture was added to the melt for reaction to occur. The mixture was sonicated for 10 min (peak-to-peak amplitude of 50 μm) and the unwanted slugs on the melt surface were removed. After solidification A1350 Al alloy was dissolved away in 20 vol. % aqueous Hydrochloric acid (HCl). The resultant TiB_2 nanoparticles were collected once the mixture solution was centrifuged [125]. XRD results (Figure 11a) and TEM images of the synthesized TiB_2 nanoparticles are shown in Figure 11b and Figure 11c.

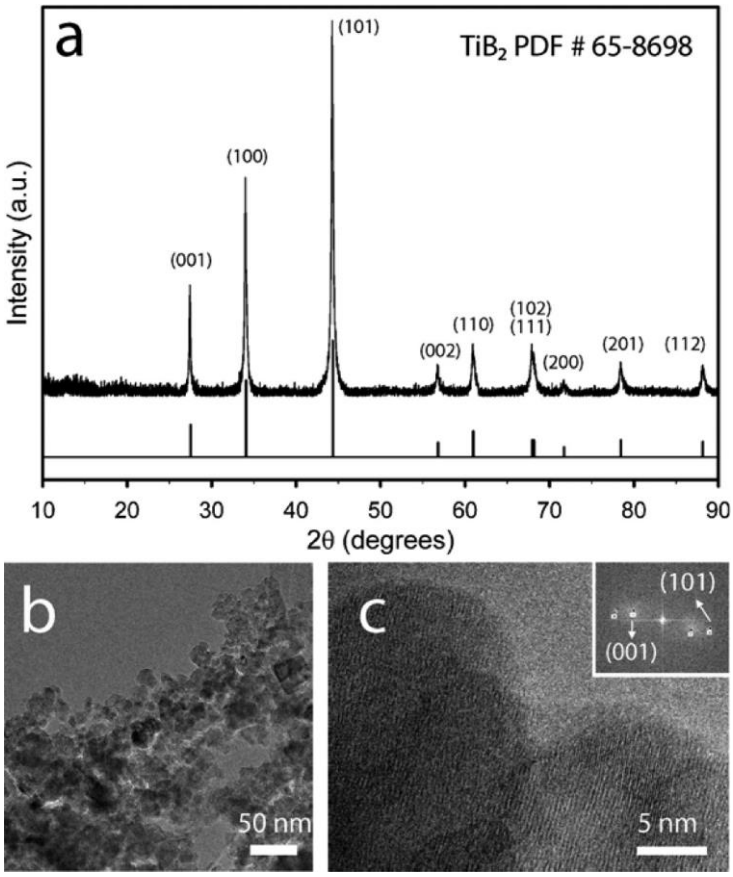

Figure 11: (a) XRD, (b), and (c) TEM characterization of the as prepared TiB_2 nanoparticles [125].

2.4.2 Ex-situ Nanoparticle Synthesis in Matrix

Diboride Nanoparticles

Salt-assisted nanoparticles synthesis has been widely used to produce nanoparticles with small sizes. *Portehault et al.* used one-pot ionothermal process which requires moderate temperature, atmospheric pressure, and environmentally friendly solvent to synthesize hexaborides (CeB_6, CaB_6), tetraborides (MoB_4), diborides (NbB_2, HfB_2). In this method, solid metal chlorides as metal precursor and sodium borohydride as the boron source and reluctant were used. Eutectic LiCl/KCl (45:55 wt. %) mixture was selected as low-melting-point (355 °C), water-soluble, and sustainable solvent to initiate the chemical reactions in liquid state. It was reported that NbB_2 and CaB_6 were successfully synthesized with crystalline size about 3 nm and 10 nm, respectively [126]. Figure 12 shows TEM images of the synthesized NbB_2.

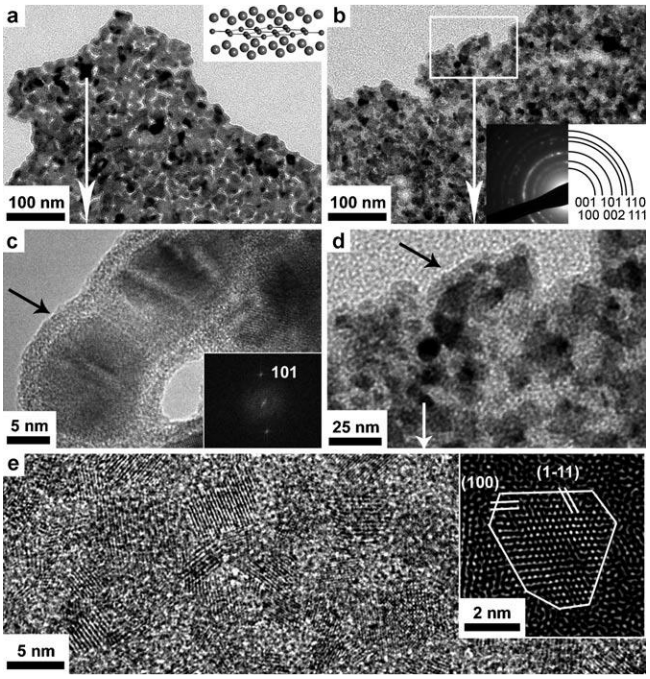

Figure 12: TEM pictures of niobium diboride nanocrystals obtained at 900 °C with $NbCl_5/NaBH_4$ = 1:4 (a, c) and 1:8 (b, d, e). Corresponding SAED pattern (c) and Fourier filtered HRTEM zoom (e) are shown as insets. The black arrows (c, d) highlight an amorphous matrix embedding the particles [126].

Silicide Nanoparticles

Salt-assisted nanoparticles synthesis was used by Estruga to synthesize Ti_5Si_3 nanoparticles. Mg powder, TiO_2 nanoparticles, SiO_2 nanoparticles (20:5:3 molar ratio) and a LiCl–KCl eutectic mixture (45:55 wt. %) were manually ground for 15 min [127] to achieve a uniform powder size. The chemical reaction is shown in below.

$$5TiO_2 + 3SiO_2 + 16Mg \rightarrow Ti_5Si_3 + 16MgO$$

The mixture was then sealed into a stainless steel autoclave inside an Ar-filled glovebox and heated up to 700 °C for 2h in a box electrical resistance furnace. Then, the autoclave was naturally cooled down to room temperature. To dissolve the eutectic salts, the synthesized product was washed with Deionized water. Then, it was washed with a 2 M HCl solution and water to remove the residual magnesium oxide (MgO) by-product. Powder X-ray diffraction (PXRD) confirmed the perfect match (Figure 13a) with hexagonal Ti_5Si_3 nanoparticles [127]. Ti_5Si_3 nanoparticles as small as 25 nm was synthesized (Figure 13b).

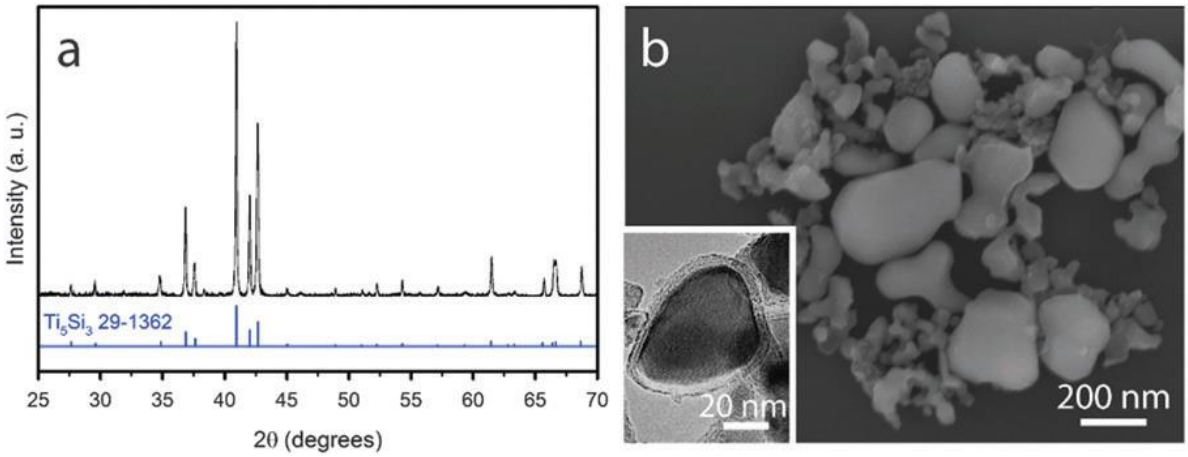

Figure 13: (a) PXRD, and (b) SEM and TEM (inset) of the Ti_5Si_3 nanoparticles prepared in absence of molten salts [127].

CHAPER 3. POLYMER METAL NANOCOMPOSITES

3.1 Composite Preform Fabrication

Non-uniform Sn (Sigma-Aldrich Corporation) and PES (Sumika Electronic Materials, Inc.) microparticles were used with an average diameter of 40 and 60 μm, respectively. The polymer composite preforms of PES-5.0 vol. % Sn (PES-5Sn composite) were first consolidated by thermal sintering before thermal drawings. The experimental procedure is presented below. Figure 14 shows the schematic of the thermal melting process for the fabrication of PES-5 Sn composite preforms. The PES (95.0 vol. %) and Sn (5.0 vol. %) microparticles were first blended by a mechanical shaker for one hour. The well-blended microparticles were added to a cylindrical stainless steel mold with an outer diameter (OD) of 31.75 mm, an inner diameter (ID) of 19.05 mm, and a height of 152.4 mm (the mold was manufactured in house). A hydraulic press was used to compact the well-blended powder mixtures at room temperature. An electrical resistant furnace was then used to melt the compacted powder at 260 ºC for one hour to form a solid preform of PES-5Sn composite preform [128].

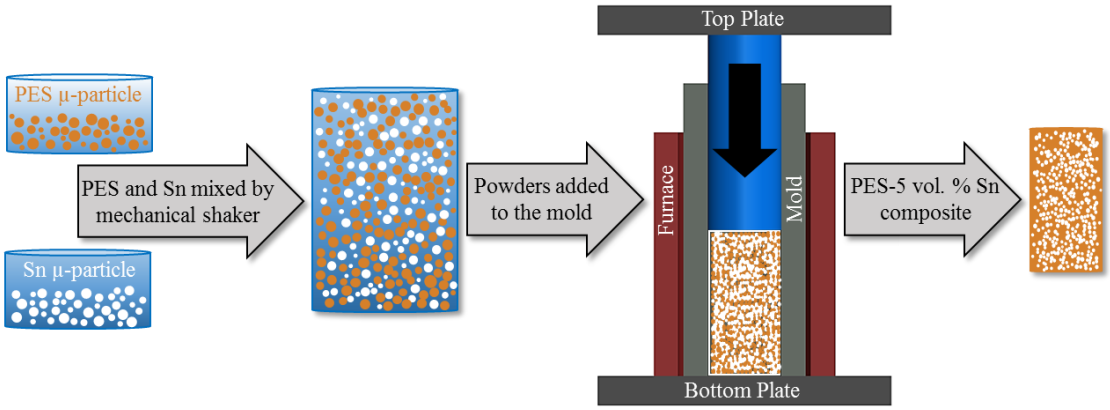

Figure 14: Schematic of the thermal consolidation process [128].

3.2 Thermal Fiber Drawing Experiments

Multiple cycles of thermal fibers drawings were carried out to elongate the embedded Sn microparticles of random sizes into microfibers and finally into Sn nanoparticles. Figure 15 represents the schematic of the first cycle of thermal drawing process. In the first drawing cycle, the PES-5Sn composite preform with a diameter of 19.05 mm was drawn down to a long composite fiber with a diameter of 500 μm under the drawing parameters as shown in Table 3.

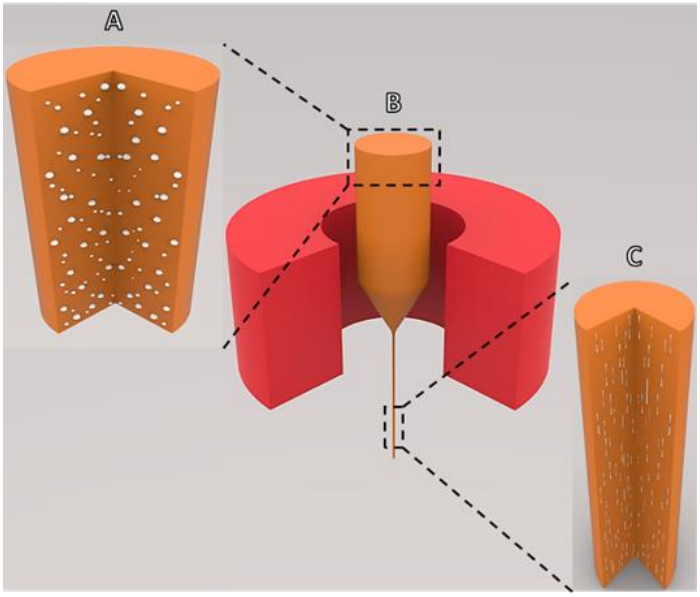

Figure 15: (A) Schematic of the PES-5 Sn composite preform, (B) Composite perform thermally drawn (the first cycle), and (C) PES-5 Sn composite fiber after first cycle of thermal drawing.

Table 3: Parameter for thermal fiber drawing experiments.

Temperature (°C)	Feeding speed (mm/s)	Pulling speed (mm/s)	Initial diameter (mm)
300	0.01	10	19.05

Using a stack and draw process as shown in Figure 16, the composite fibers from the first drawing cycle were cut, stacked and inserted into a cylindrical PES (with dimensions of 19.05 mm in OD, 3.8 mm in ID, and 8 cm in length) to form the preform for the second drawing cycle. The preform for the third drawing cycle was fabricated following the same procedure. The second and third cycles of thermal fiber drawings were carried out in the same conditions as in the first cycle.

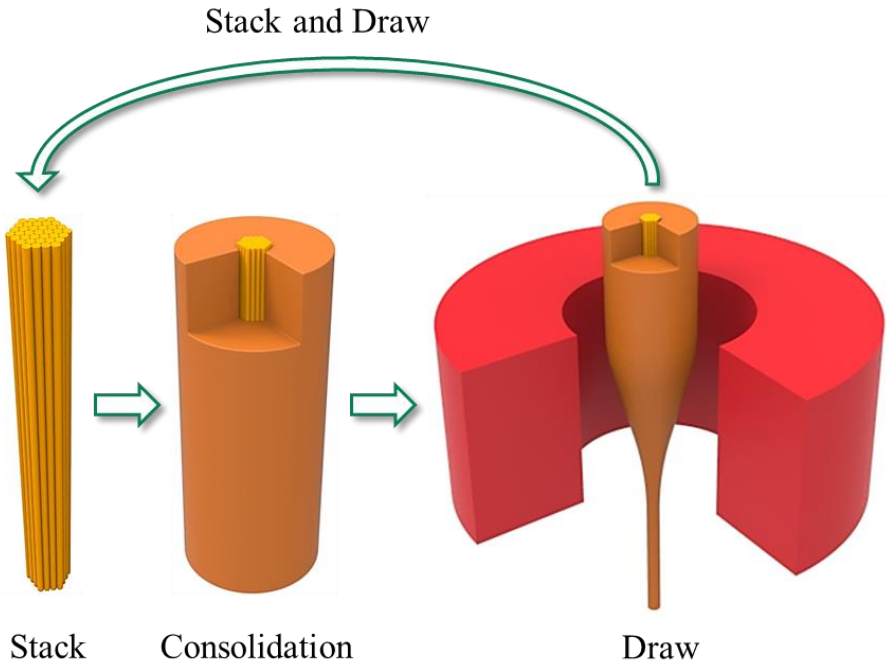

Figure 16: Schematic of the stack and draw iteration process.

3.3 Experimental Results

3.3.1 Sn Particle Distribution in the PES-5Sn Composite Preform

A cross-sectional cut from the PES-5Sn composite perform was used to study the distribution and dispersion of Sn microparticles. Figure 17A shows the typical optical microscope images of the longitudinal cross-sections of the PES-5Sn composite preform. The size distribution of the Sn microparticles in the initial preform is shown in Figure 17B.

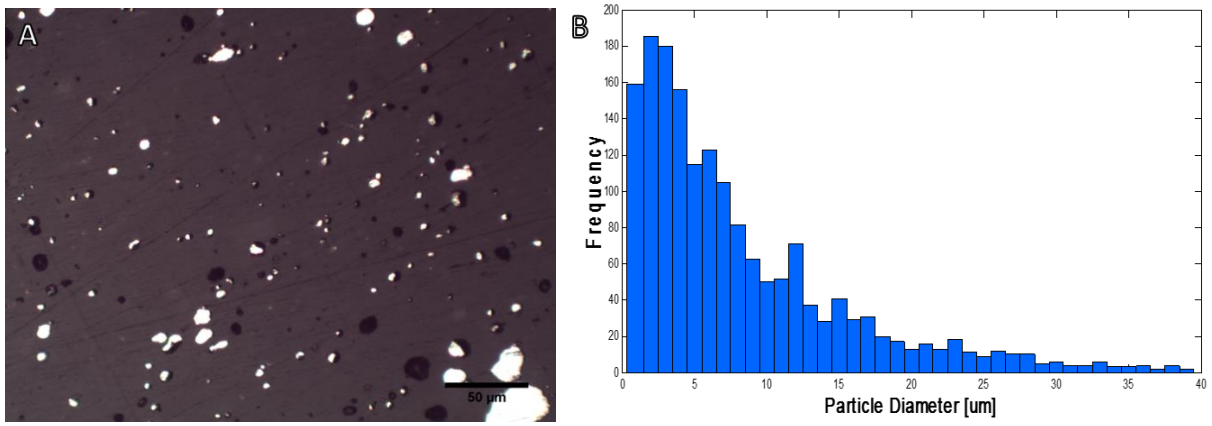

Figure 17: (A) A typical optical microscope image obtained from the longitudinal cross-section of the PES–5Sn composite perform, and (B) Sn microparticles size distribution in the PES-5Sn composite perform.

3.3.2 PES-5Sn Composite Microfibers

After the first thermal drawing cycle, we attempt to observe the drawn composite fibers from the longitudinal direction (from its sidewall) to reveal the Sn microfibers embedded in the PES matrix. Fibers of 1.0 cm long was cut after the first cycle and mounted on a carbon tape, which was attached to a scanning electron microscopic stub from the other side (Figure 18A). Multiple longitudinal cuts were made on the sidewall of the composite fibers using an ultramicrotome tool (Figure 18B). We used ZEISS Supra 40VP SEM machine to obtain images from the surface of composite fiber after cutting several layers (Figure 18C). To further characterize the first composite fiber, we cut five short fiber pieces (1.0 cm long each) from the long fibers. Fiber pieces were placed inside a rectangular box (2.54 x 2.54 cm) made out of stainless steel sheet cloth. The box was submerged in N-Methyl-2-pyrrolidone (NMP) for 5 hours at 70 ºC to dissolve the PES claddings to expose the metal micro-fibers. Figure 18D reveals Sn microfibers in the typical optical microscope images which were obtained from composite fiber after first cycle of thermal drawing. Same characterization steps were performed for the composite fibers after second thermal drawing cycle. Using ImageJ software, the diameter of Sn microfibers

were determined to be 6±1 and 2±0.5 μm after the first and second thermal drawing cycles, respectively. It should be noted that the Sn microfibers vary in length while the diameter of the Sn fibers becoming smaller from first to second cycle.

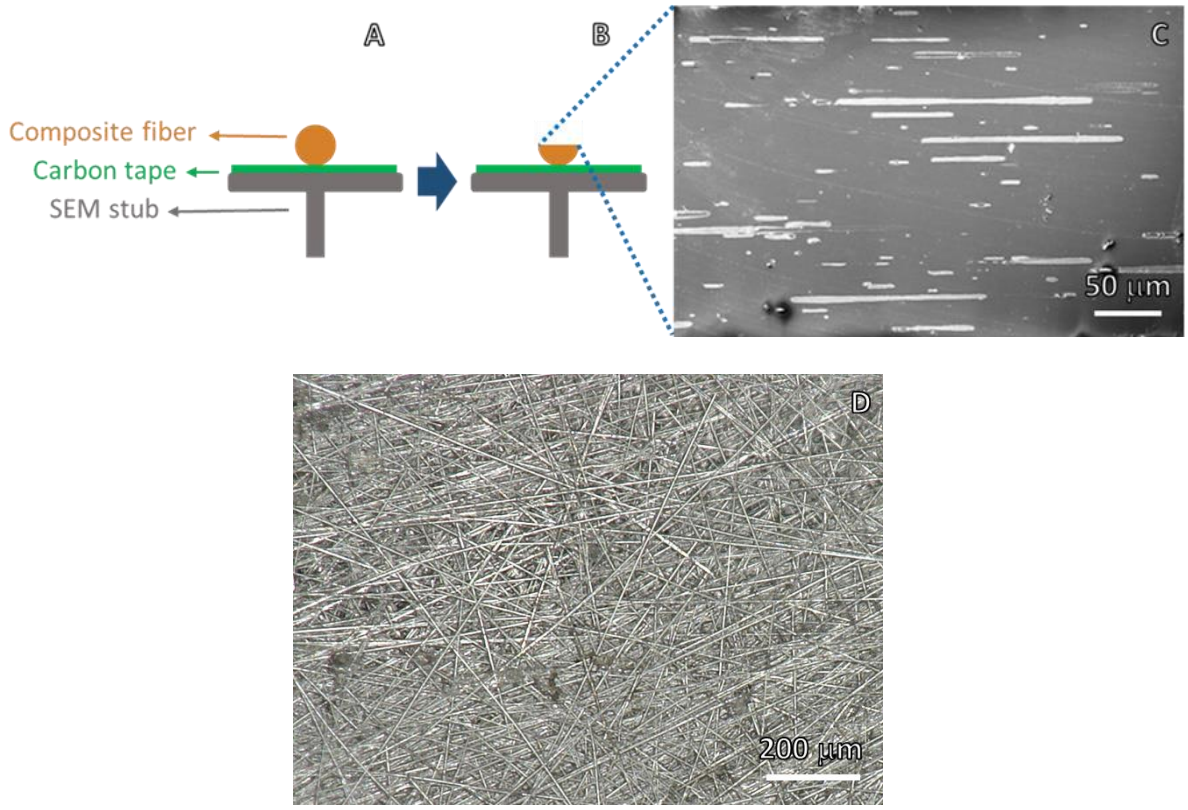

Figure 18: (A) Schematic of a 1.0 cm long composite fiber (after first drawing cycle) on a SEM stub, (B) multiple longitudinal cuts were made on the outer surface (sidewall) of the composite fiber by an ultramicrotome tool, (C) SEM image of the composite fiber surface after several longitudinal cuts, and (D) A typical optical microscope image of Sn microfibers acquired after PES cladding was dissolved (after the first thermal drawing cycle).

3.3.3 PES-5Sn Nanocomposites with Uniform Dispersion Sn Nanoparticles

After the third drawing cycle, the ultramicrotome technique (described previously) was used to prepare films of 500 nm thick from the sidewall of the composite fiber and manually placed on the carbon tape for SEM study (Figure 19A and Figure 19B). Figure 19C and Figure 19D show a uniform distribution and dispersion of Sn nanoparticles inside the PES matrix. It will be of a

significance to study how the uniformly dispersed nanoparticles are formed during the thermal drawing processes.

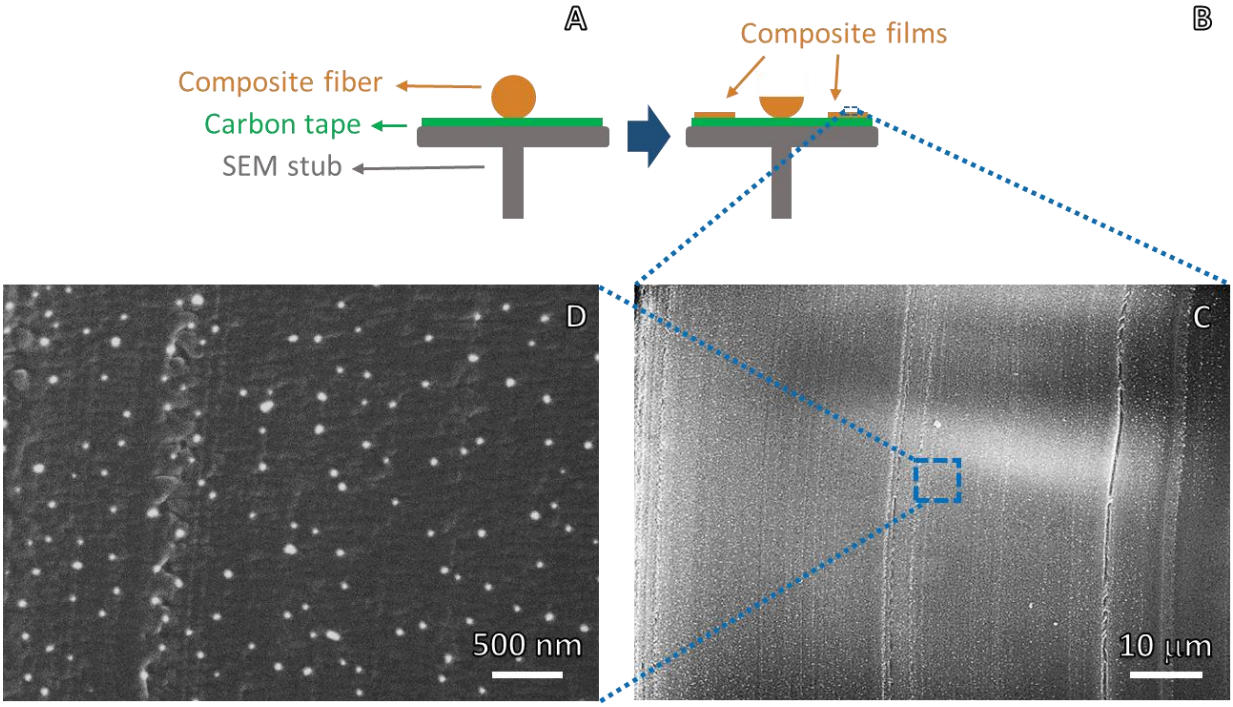

Figure 19: (A) Schematic of a composite fiber (after the third drawing cycle) on a SEM stub, (B) Schematic of the composite fiber and films prepared by the ultramicrotome tool, (C) and (D) are SEM images taken from the thin films prepared by the ultramicrotome tool.

3.3.4 Sn Nanoparticles Size Distribution in PES-Sn Nanocomposites

After the third drawing cycle, Sn nanoparticles size was measured from seven fiber samples. More than 3500 measurements were conducted to statistically determine the average size of the Sn nanoparticles to be 46 nm, as shown in Figure 20. Most of the Sn nanoparticles are less than 100 nm.

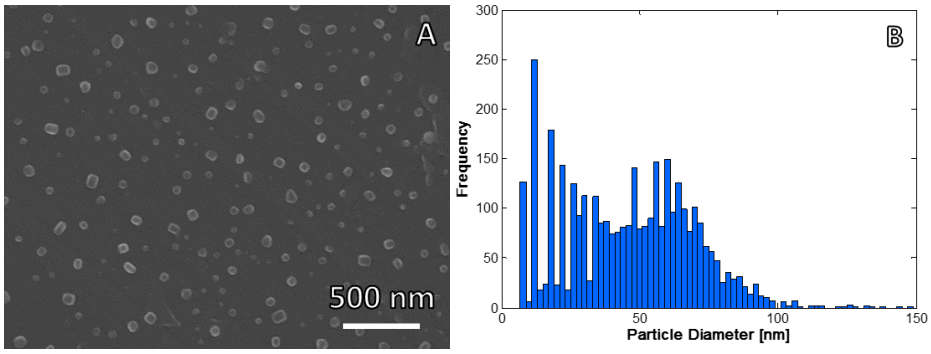

Figure 20: (A) A typical SEM image of composite fiber after third drawing cycle and (B) Sn nanoparticles size distribution in composite fibers after the third thermal drawing cycle.

To study the size of the smallest produced Sn nanoparticles, the composite fiber after the third drawing cycle was cut into 5 pieces of 1ft long and dissolved in NMP solution at 70 ºC for 5 hours. The NMP solution was then centrifuged to extract Sn nanoparticles. Upon a thorough NMP removal, TEM samples were prepared. Titan S/TEM (FEI) machine was used to obtain the TEM images (Figure 21A and Figure 21B). Our atomic resolution TEM results show that the smallest Sn nanoparticles produced were about 10 nm (Figure 21C).

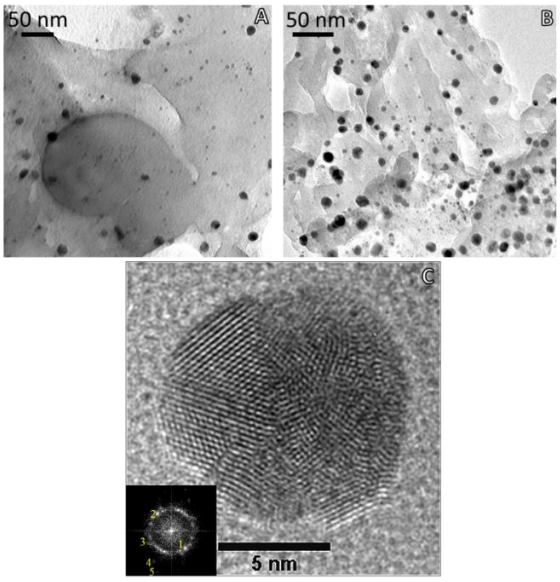

Figure 21: (A) and (B) TEM images of the Sn nanoparticles acquired after third cycle of the thermal drawing where PES cladding was dissolved, and (C) Atomic-Resolution TEM image shows multi-twinned β-Sn nanoparticles.

More composite films (with thickness ranging from 100 to 500 nm) were cut from the longitudinal side of the PES-5Sn nanocomposite fibers (after the third cycle of thermal drawing) for further investigations (Figure 22a). Nanocomposite films were carefully placed on a TEM grid (Pure carbon 200 mesh, Ted Pella Inc.). High-resolution TEM (HRTEM) confirms the existence of α-Sn and β-Sn and Sn_2O_3 nanoparticles embedded in PES matrix film (Figure 22b).

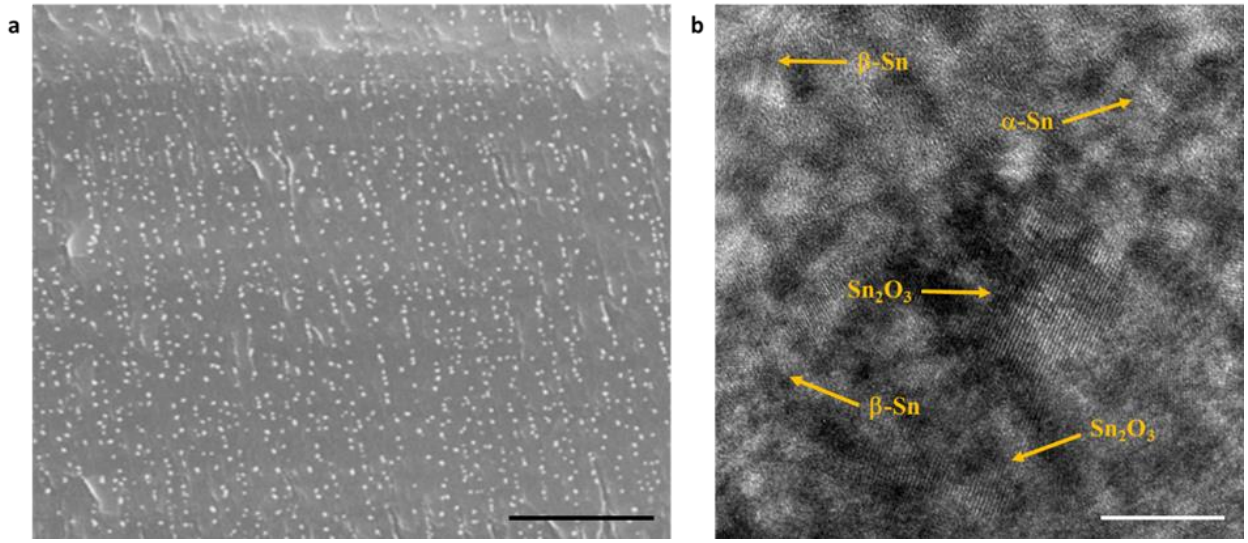

Figure 22: (a) SEM image of a nanocomposite film (from PES-5Sn nanocomposite fiber) prepared by ultramicrotome tool (after third cycle of thermal drawing) (scale bar: 2μm), and (b) HRTEM image obtained from a nanocomposite film (scale bar: 10nm).

3.3.5 Measurement of Index of dispersion

The index of dispersion (ID) is measured from [129]:

$$ID = \frac{s^2}{\bar{x}} \tag{1}$$

Where $\bar{x}$ and s^2 are the sample mean and variance of the number of the points per quadrat. $ID < 1$ suggests uniform particle dispersion while $ID > 1$ indicates clustering. Image processing was

done on each quadrat taken, respectively, at random locations from the longitudinal cross-sections of the PES-5Sn composite preforms and PES-5Sn nanocomposite fibers. The quadrats counts are measured by ImageJ [130], shown in Figure 23.

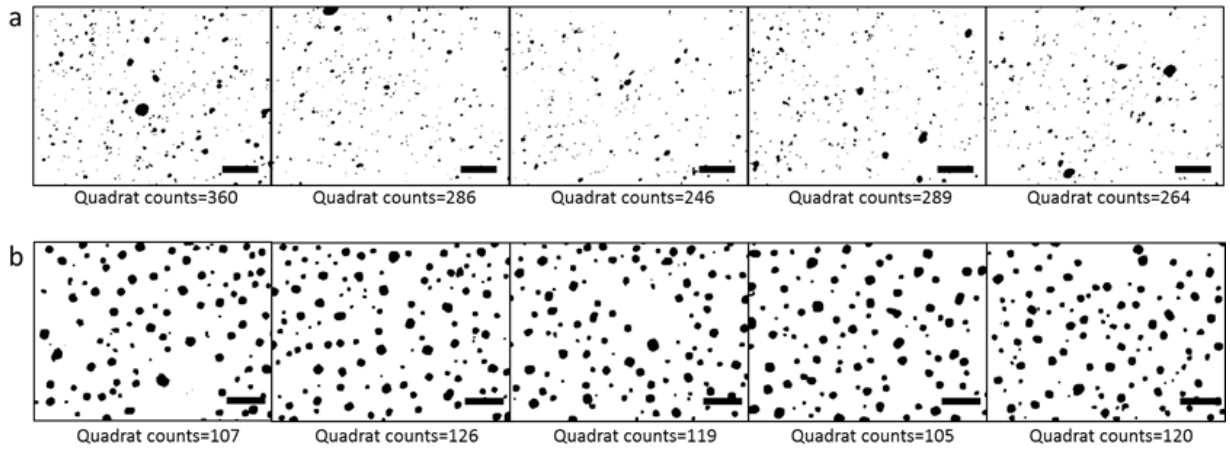

Figure 23: (a) optical microscope images taken from 5 random locations on the longitudinal cross-section of the PES-5 Sn composite preform processed by ImageJ software (scale bars are 100μm), and (b) SEM images taken from 5 random locations on the longitudinal cross-section of the PES-5Sn nanocomposite fiber (after the third cycle of the thermal drawing) processed by ImageJ software (scale bars are 300nm).

3.4 Summary

This work focused on the scalable nano-manufacturing of polymer-metal nanocomposites enabled by thermal drawing nano-emulsification. A simple and cost-effective method was used to fabricate scalable PES-5 Sn composite preforms. After the first thermal drawing cycle, metal microfibers with various diameters and lengths were well aligned in the longitudinal direction of composite polymer fibers. Using a stack and draw iteration, further drawing cycles produced polymer-metal (PES-5Sn) nanocomposite fibers with a uniform dispersion of Sn nanoparticles. Uniformly dispersed Sn nanoparticles with average size of 46 nm were successfully obtained in the polymer fibers from non-uniform Sn microparticles for the first time. This scalable, novel, and inexpensive manufacturing method paves a new way for mass production of polymer-metal nanocomposites with well-dispersed nanoscale crystalline metal elements for widespread applications.

CHAPTER 4. TIB2 NANOPARTICLE SYNTHESIS

We have chosen TiB_2 nanoparticles to reinforce Al and Mg matrices since it is an extremely hard ceramic, a refractory material (retains its strength at elevated temperature) with excellent heat conductivity, oxidation stability and resistance to mechanical erosion with a moderate electrical conductivity (10^5 S/cm). TiB_2 has the highest electrical conductivity in metal-like ceramics. The aforementioned properties make TiB_2 a great candidate to be used as reinforcements for Al electrical conductor wires. To synthesize TiB_2 nanoparticles with precise size control, a salt assisted nanoparticle synthesis method was utilized.

4.1 Experimental Procedure

Eutectic LiCl/KCl (45:55 wt. %) salts were dissolved in methanol. TiO_2 nanoparticles with average size of 5 nm (purchased from US Research Nanomaterials) was then added to the solution. In order to well-disperse the TiO_2 nanoparticles in the solution, the mixture was sonicated for 30 min (peak to peak amplitude of 50 μm). The beaker was placed on a hot plate to promote methanol evaporation. Upon thorough methanol evaporation, dried reagents were placed in a vacuum oven (150 °C) for dehydration (for 12 hours). Mg and B_2O_3 microparticles were blended with dehydrated powders (LiCl, KCl, and TiO_2). The chemical reaction equation is shown in below. Molar ratio of 1:1:5 was used TiO_2:B_2O_3:5Mg, and Mg weight percent of 16% of the total salt weight.

$$TiO_2+B_2O_3+5Mg \rightarrow TiB_2+5MgO$$

Well-blended powders were added to a graphite crucible and were placed in a stainless steel autoclave. The autoclave is made out of 304 stainless steel with 1.12 in wall thickness and outer diameter of 2 in and 3.5 in height (Figure 24).

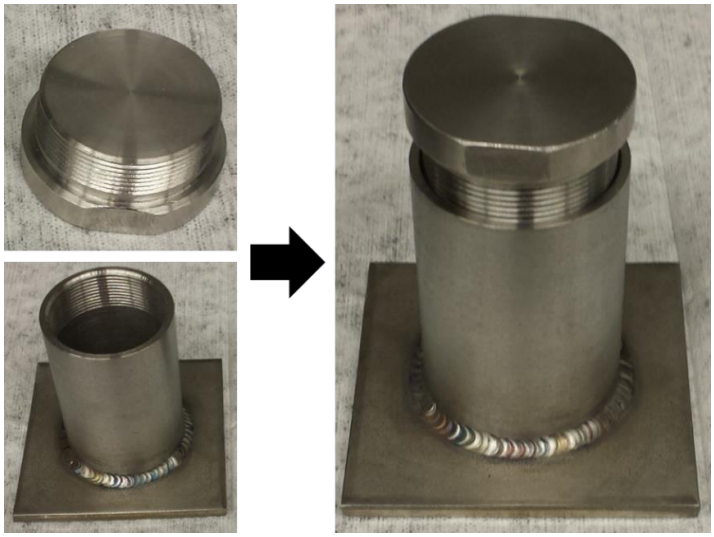

Figure 24: Images of the in-house machined 304 stainless steel autoclave to synthesize TiB_2 nanoparticles.

The autoclave was sealed with a slug and was located inside an electrical resistance furnace. For reaction to happen, the furnace temperature was raised to 700 °C and was held for two hours. To minimize the oxygen presence, the experiment was conducted under Ar gas protection. Then autoclave was then cooled down to room temperature. The graphite crucible was then removed and was broken to extract the TiB_2 synthesized products (Figure 25C and Figure 25D).

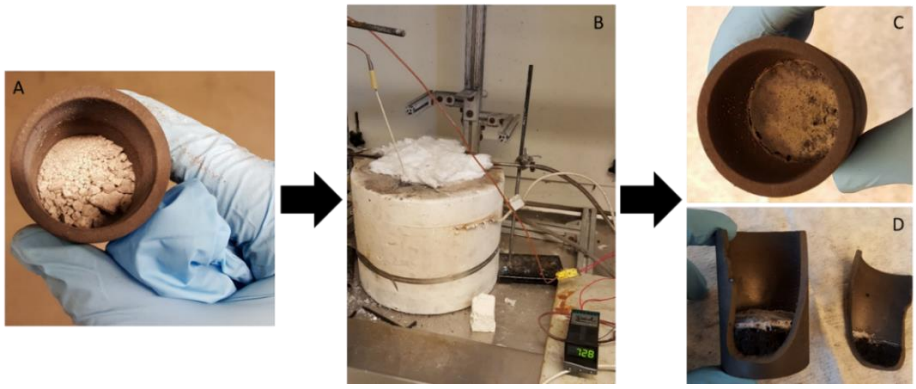

Figure 25: (A) Well-blended reagents (TiO_2, B_2O_3, Mg, KCl and LiCl) inside a graphite crucible, (B) An electrical resistance furnace used for synthesis experiments, (C) Top view of the graphite crucible once removed from the autoclave, and (D) graphite crucible is broken to extract the synthesized products.

4.2 Characterization of the Synthesized Products

To dissolve the by-product of the TiB_2 synthesis experiment, MgO, and eutectic salts, synthesized products were washed with 2M HCl and Deionized water, respectively. TiB_2 synthesis products were added to glass centrifuge tubes to for washing steps (Figure 26). Several washes with each solvent were performed to minimize the amount of the unwanted elements remained in the synthesized products. At the end of each washing step, tubes were centrifuged and the unwanted solvents were poured out from the tubes.

Figure 26: Glass centrifuge tubes containing the TiB_2 synthesis products prior to washing with deionized water and 2M HCl.

To prepare a SEM study sample methanol were added to a small portion of the well-washed synthesis product and sonicated for 10 min. A micro-pipette was used to deposit few droplets on silicon (Si) substrate. Then, the Si substrate was place on a hot plate for 1 hours for thorough evaporation of methanol (Figure 27A). SEM images of TiB_2 nanoparticles are shown in Figure 27B, Figure 27C, and Figure 27D.

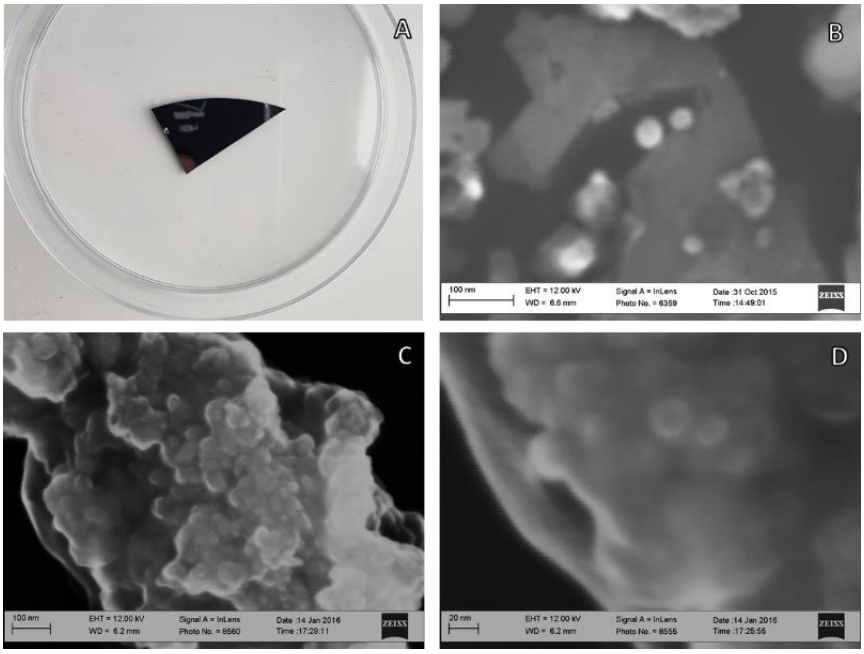

Figure 27: (A) SEM study sample prepared from well-washed TiB_2 synthesis products, (B), (C), and (D) show SEM images obtained from the TiB_2 nanoparticles.

A few droplets were deposited on a TEM grid from the prepared solution (described in above). TEM samples were prepared from the washed TiB_2 nanoparticles to better study the size of the nanoparticles. Our results show that we were able to successfully synthesize TiB_2 nanoparticles as small as 5 nm (Figure 28A and Figure 28B).

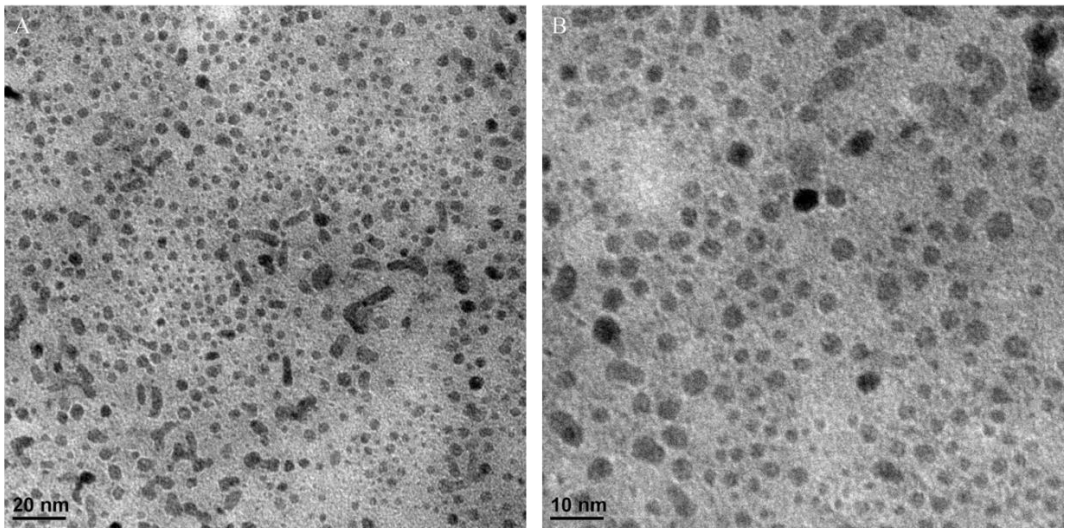

Figure 28: (A), and (B) TEM images obtained from as-washed TiB_2 nanoparticles.

In order to estimate the size of the TiB_2 nanoparticles, statistical tools were used. More than one million nanoparticles were measured from ten high magnification TEM images. Our analysis indicates that TiB_2 nanoparticles with average size of 8.1±0.4 nm was successfully synthesized. These results confirm that the reaction (1) occurred completely. High resolution TEM images further confirmed the presence of the TiB_2 nanoparticles. Figure 29A and Figure 29B show atomic resolution TEM images acquired from as-washed TiB_2 nanoparticles.

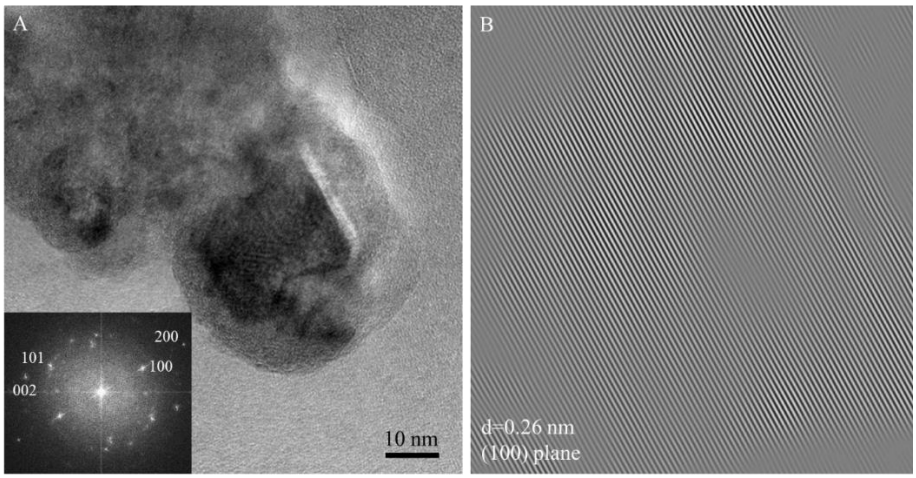

Figure 29: (A) shows a high resolution TEM image obtained from TiB_2 nanoparticles with an inset showing TiB_2 facets as confirmed by their ring patterns, and (B) Fourier filtered atomic resolution TEM image showing a crystalline plane (100) of the TiB_2 nanoparticles.

To identify the phases of the synthesized TiB_2 nanoparticles, XRD test was carried out on TiB_2 nanoparticles. Powder X-ray diffraction (XRD) patterns were collected on a Bruker D8 Advance Powder Diffractometer using Cu Kα1 radiation. XRD result (Figure 30) confirms the existence of the TiB_2. However, this results indicates that the yield of our TiB_2 synthesis is low.

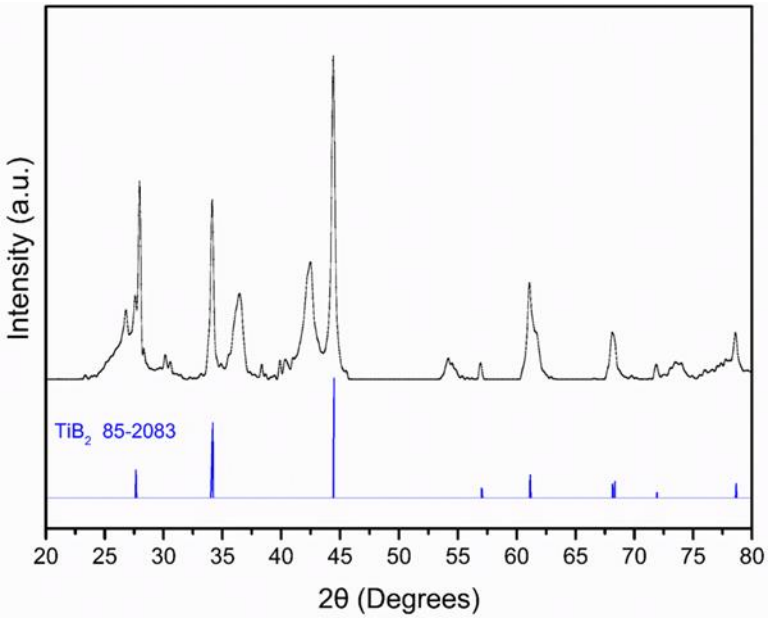

Figure 30: XRD test result of the washed TiB_2 nanoparticles show eight major peaks match with the reference peaks.

4.3 TiB_2 Reaction Mechanism

The general mechanism for the TiB_2 formation is through the reduction of the TiO_2 [131, 132] and B_2O_3 by metallic Mg under suitable temperature (reaction 1) [133]:

$$TiO_2 + B_2O_3 + 5Mg \rightarrow TiB_2 + 5MgO \text{ (reaction 1)}$$

The TiB_2 nanoparticle synthesis occurs via the magnesio-reduction of the metal oxides by the electrons which are provided by dissolved Mg, solvated in the eutectic salt (reaction 2).

$$Mg_{(s)} \leftrightarrow Mg^{2+}_{(diss)} + 2e^-_{(diss)} \text{ (reaction 2)}$$

In our synthesis experiment, the raw materials of B_2O_3, TiO_2, and Mg (as reducer for magnesiothermal reaction) are used. This reaction is possible in a eutectic chloride salt medium [134]. The reaction continued in the sealed autoclave under 700℃ for two hour to reduce the oxygen disturbance to Mg as the electron donor.

In the reaction, the boron trioxide reduction occurs via a dissolution mechanism, and the B_2O_3 precursors become solvated in the molten salts to allow the reaction to happen. Mg first reduce B_2O_3 to amorphous B (in element form) [132] by the electrons provided via reaction 2, since B_2O_3 can be more easily dissolved in Cl^- salt.

$$B_2O_3+3Mg \rightarrow 3MgO+2B \text{ (reaction 3)}$$

At the same time, the boron trioxide dissolution process leads to the formation of the soluble MgO, which is formed by reaction 3. The solubility of MgO guarantees the mobility of reduced B for further reactions. Due to the high activity of the B element, B ion diffuses to the surface of the TiO_2 during the TiO_2 reduction caused by excessive Mg ions. The residual TiO_2 demonstrates the difficulty of TiO_2 to be directly reduced by Mg, and the produced TiO/Ti_2O phase. TiO_2 oxides are generally difficult to be dissolved in KCl and LiCl salts [132, 135].

$$3TiO_2 + (4\text{-}2x)\ B \rightarrow 3TiO_x + (2\text{-}x)\ B_2O_3 \text{ (intermediate reaction) (reaction 4)}$$

$$3TiO_2 + 4B \rightarrow 3Ti + 2B_2O_3 \text{ (reaction 5)}$$

$$TiO_2 + 2B \rightarrow Ti + B_2O_3 \text{ (reaction 6)}$$

After Ti release in the chloride solution it reacts with element B to form TiB_2.

$$Ti + 2B \rightarrow TiB_2 \text{ (reaction 7)}$$

Our synthesis route bases on metal solvation in eutectic chloride salt matrix. The key is to provide the immediate and sufficient reduction electrons (provided by Mg ions) and to guarantee the mobility of electrons and/or reduced intermediate products such as B. The good aspects of our synthesis method root in the removal of the possible boric salts (e.g. $B_2O_6^{6-}$) and titanate salt (e.g. TiO_4^{4-}) [133] which reduces the impurity purification and post processing.

4.4 Summary

In this study, a simple, scalable method was introduced to synthesize surface-clean TiB_2 nanoparticles with a size as small as 5 nm. HRTEM confirmed the different planes of the TiB_2 crystalline without existence of any other elements. The magnesio-reduction of TiO_2 nanoparticles and B_2O_3 particles in eutectic LiCl–KCl melts at 700 °C results in the formation of ultra-fine crystalline TiB_2 nanoparticles with an average particle size of 8.1 ± 0.4 nm. The boric trioxide reduction occurs via a dissolution mechanism and TiB_2 nanoparticles form on the titania surface via a heterogeneous template mechanism. The limited solubility of Mg powder in the molten salts maintains low supersaturation conditions, thus allowing the control of crystal growth at the TiB_2 nanoscale. This scalable method is a promising method for mass production of small crystalline TiB_2 nanoparticles to be used in a wide range of applications specifically as nano-scale reinforcements.

CHAPTER 5. METAL NANOCOMPOSITE MICROPARTICLES

Nano-scale structure synthesis has become an emerging field [136-142]. Diverse approaches have been introduced and developed to synthesize nano-scale structures. Developing novel organic and inorganic nanostructure are of significant interest due to their widespread applications such as catalysts [143-145], thermoelectric materials [146], battery electrodes [147, 148], magnetic materials [149-151], and solar cells [152, 153]. Over the past two decades, additive manufacturing or three-dimensional printing has advanced new opportunities in manufacturing of complex materials such as metals, polymer and ceramics.

Metal-based 3D printing has shown an unexpected growth in industries, including but not limited to, aerospace, defense, navy, tooling, biomedical, and automotive. Building functional parts layer-by-layer provide an invaluable design freedom and manufacturing flexibility. 3D printing of metal parts is a viable alternate for various practical application in aerospace and defense industries. Currently, more than 5500 alloy systems used in daily life cannot be 3D printed [8, 9]. In addition, 3D printing of metallic systems such as pure Al and it alloys are not ready for practical applications due to their poor solidification behavior, high oxidation tendency, and low mechanical property. Therefore, there is a strong need for the development of unique microscale metallic structures to be used in 3D printing to tackle solidification behavior, and more importantly, offer promising mechanical properties. However, self-incorporation of high concentration nano-scale reinforcements into metal microparticles has remained an unresolved challenge.

Adding suitable nanoparticles into metal microparticle matrix can result in unusual behavior of the nanocomposites. This would also significantly change the solidification behavior

of such nanocomposites. High volume percent nanoparticle incorporation into lightweight metal powders can be beneficial for additive manufacturing. Nanoparticles can alter the solidification behavior of the metals during melting process as well enhancing the mechanical properties upon solidification. This class of hybrid materials provide exciting opportunities for the low density metals to compete with the high density metals.

5.1 Experimental Procedure

5.1.1 Material and Methods

Sodium chloride powder (NaCl, > 99.99%), potassium chloride power (KCl, > 99.00%), aluminum powder (Al, > 99.98%), aluminum powder (Al, 99.98%) and magnesium powder (Mg, > 99.98%) were purchased from Sigma Aldrich. In-house synthesized TiB_2 nanoparticles (average size less than 10 nm) was used in this study. TiC nanoparticles (with 60 nm average size) was purchased from US Research Nanomaterials Inc.

Figure 31 represents the schematic of the experimental set up. Flux assisted liquid state processing were employed to successfully incorporate the TiC and TiB_2 nanoparticles into Al and Mg metal microparticles. Metal microparticles, nanoparticles, NaCl, and KCl were mechanically mixed at room temperature for 3 hour (nanocomposite: flux ratio, 1:10 volume percent). Adding a suitable flux agent promotes self-assembly and self-dispersion of the nanoparticles into the metal microparticles. Mixture was put in a graphite crucible and was placed inside an electrical resistance furnace. Crucible was heated to 820 ºC and a mechanical mixing blade was then inserted to stir the molten liquid for 30 min at 200 rpm. The melt was naturally cool down at room environment and synthesis product was carefully extracted. Mg-30 vol. % TiC, Mg-30 vol. % TiB_2, and Al-30 vol. % TiB_2 nanocomposite microparticles were successfully produced.

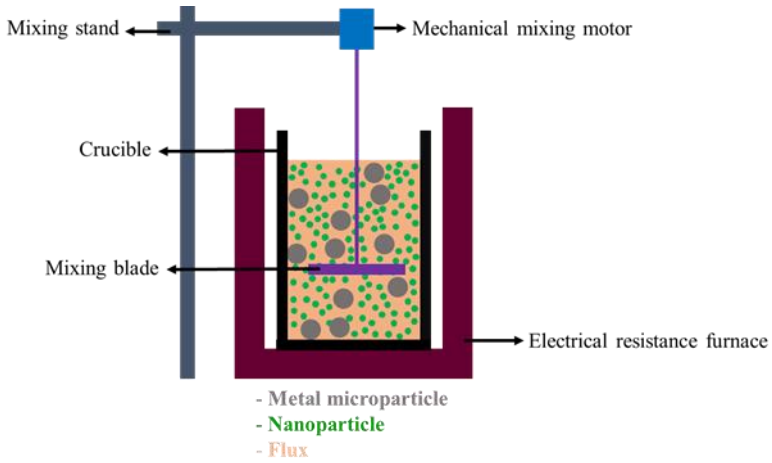

Figure 31: Schematic of the experimental set up to effectively incorporate the nanoparticles into metal microparticles.

5.1.2 Sample Preparations

The synthesis product was broken into smaller pieces and were put in glass centrifuge tubes. Deionized water was added to each tube to dissolute the chloride flux from the synthesis product. The glass tubes were sonicated for 30 min followed by centrifugal process at 4000 rpm for 4 min to separate the liquid solution form the metal microparticle nanocomposites. The aforementioned process was repeated for four times to thoroughly eliminate the flux from the metal nanocomposite microparticles. Solution droplet was implemented using ethanol. Few droplets from the solution was deposited on silicon wafer to prepared study samples for electron microscopy characterization.

5.2 Characterization

Scanning electron microscopic images were acquired using a ZEISS Supra 40VP field emission microscope operating at 10 kV and Energy-dispersive spectroscopy (EDS) mapping was

performed in the same SEM field emission microscope. Nova 600 Focused ion beam (FIB) was utilized to reveal the nanoparticles embedded inside the metal microparticle nanocomposites.

5.2.1 Mg-30 vol. % TiC Nanocomposite Microparticles (Mg-30 TiC)

Figure 32 shows SEM and EDS images obtained from the Mg-30 TiC after removal of the chloride flux. TiC nanoparticles are covering the whole surface of the Mg microparticles (Figure 32a and Figure 32b). Figure 32c, Figure 32d, and Figure 32e represent EDS mapping images on Mg-30 TiC. TiC nanoparticles cover the whole surface of the Mg microparticles. Since EDS cannot detect the low atomic number element precisely, carbon element was not detected.

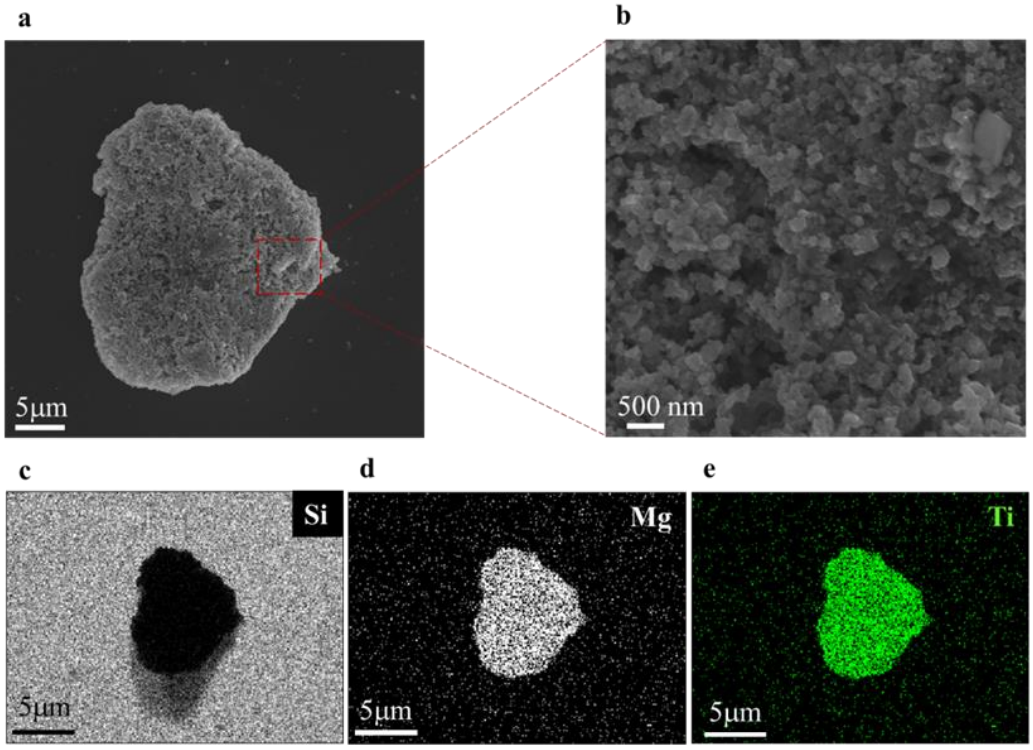

Figure 32: (a) A SEM image of typical Mg-30 vol.% TiC nanocomposite microparticles obtained after thorough removal of the chloride salts, (b) A high magnification SEM image shows TiC nanoparticles population on the surface of the Mg microparticle, (c) , (d) and (e) EDS mapping study on a Mg-30 vol.% TiC nanocomposite microparticle illustrating Si (substrate), Mg and Ti elements.

Nova 600 FIB was used to mill the Mg-30 TiC and reveal the population of the TiC nanoparticles inside the Mg microparticles. Figure 33a shows a SEM image of the Mg-30 TiC before ion-milling (52º angles). Several cross-sectional cuts were performed to reveal the TiC nanoparticles populations inside the Mg microparticle. Low and high magnification SEM images are shown in Figure 33b and Figure 33c, respectively. TiC nanoparticles are densely packed and embedded inside the Mg microparticles.

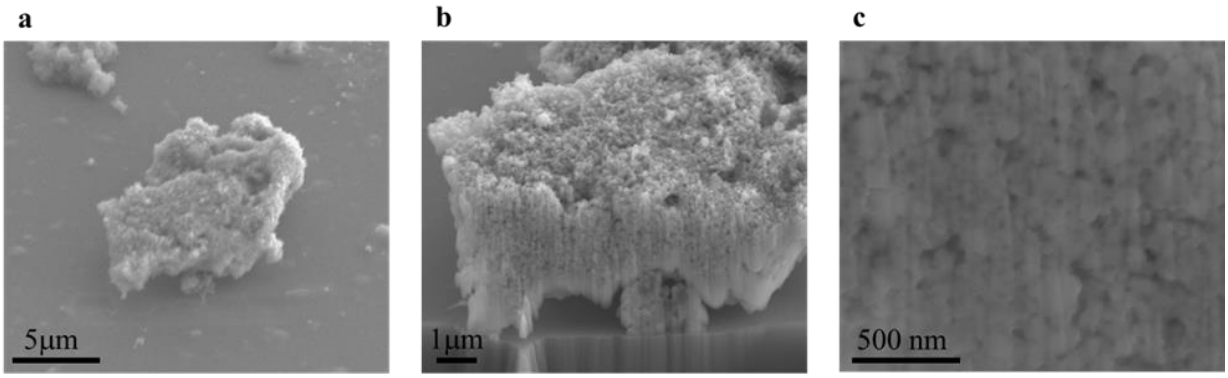

Figure 33: (a) A SEM image taken from Mg-30 vol. % TiC nanocomposite microparticles at 52° tilted angle, (b) SEM image of the Mg-30 TiC after several layers were milled, and (c) A high magnification SEM image showing TiC nanoparticles inside the Mg microparticle.

5.2.2 Al-30 vol. % TiB_2 Nanocomposite Microparticles (Al-30 TiB_2)

Figure 34 shows SEM and EDS images obtained from the Al-30 TiB_2 after removal of the chloride flux. The TiB_2 nanoparticles are well-dispersed and distributed on the surface of the Al microparticles (Figure 34a). Figure 34b shows that the TiB_2 nanoparticles are retaining their original size and not sintering to each other. Figure 34c and Figure 34d, and Figure 34e present EDS mapping images, showing the TiB_2 nanoparticles are covering the whole surface of the Al microparticle.

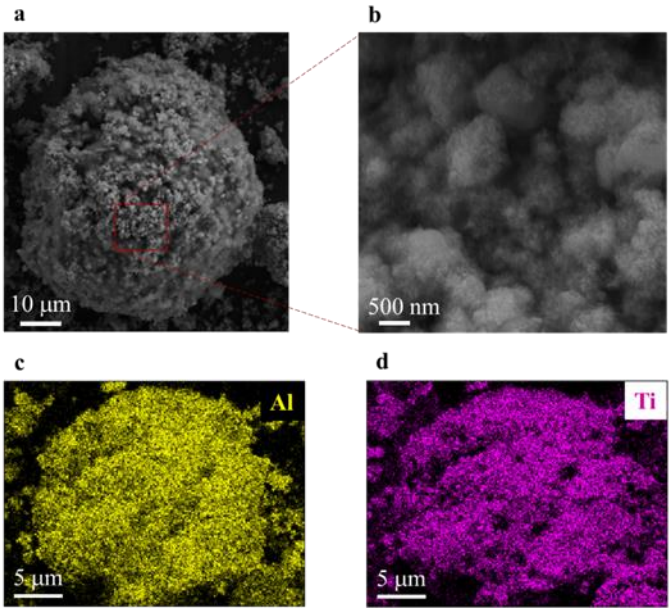

Figure 34: (a) A SEM image obtained from a typical Al-30 TiB_2 nanocomposite microparticle, (b) High magnification SEM image of the Al-30 TiB_2 sample showing small TiB_2 nanoparticles, (c) and (d) show Al and Ti element detected by EDS device.

Similar to Mg-30 TiC, FIB was utilized to mill the Al-30 TiB_2 nanocomposite microparticles. Figure 35 shows the SEM images obtained from Al-30 TiB_2 nanocomposite microparticle when tilted to 52° angle.

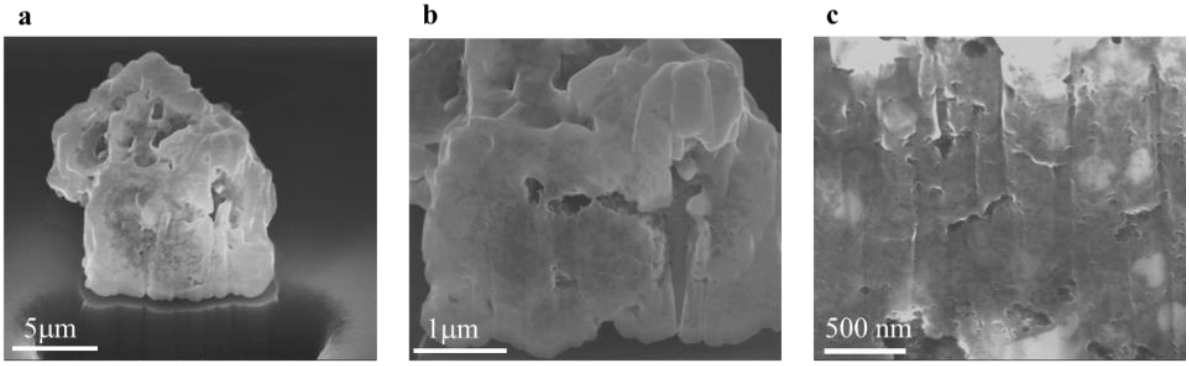

Figure 35: (a) shows a SEM image obtained from Al-30 TiB_2 at 52° tilted angle, (b) SEM image of the Al-30 TiB_2 when longitudinal cuts were made to remove several layers from Al-30 TiB_2 nanocomposite microparticle, and (c) High magnification SEM image showing the inside of a typical Al-30 TiB_2 nanocomposite microparticle.

Cold Compaction and Melting of the Al-30 TiB_2 Nanocomposite Microparticles

The Al-30 vol. % TiB_2 nanocomposite microparticles was then added to a cylindrical stainless steel mold (with diameter of 10 mm and height of 40 mm). A stainless steel ram was used to compact the nanocomposite microparticles. About 200 MPa stress was applied for 5 min at room temperature to form the pellets. The pellets were placed inside an induction furnace for melting step (900 ºC). Three melting times 20, 40, and 60 minute were used in this step. Figure 36a and Figure 36b shows the cold compacted pellet fabricated from Al-30 vol. % TiB_2 nanocomposite microparticles before and after melting, respectively.

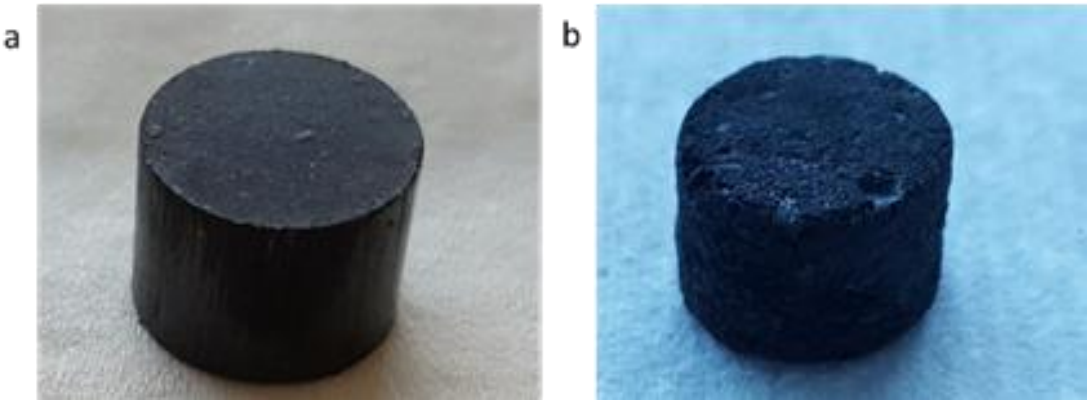

Figure 36: (a) and (b) Image of the Al-30 vol. % TiB_2 nanocomposite pellet acquired before and after melting.

Figure 37 shows SEM images obtain from the Al-30 vol. % TiB_2 nanocomposites (after melting). Figure 37a shows that after melting, there exist micron size porosity on the surface of the samples. This can be associate to the compaction step. In fact, the applied stress during compaction step was not sufficient to eliminate the gaps between nanocomposite microparticles. Figure 37b shows higher magnification SEM images obtain from the same sample. Figure 37c shows that the TiB_2 nanoparticles are uniformly dispersed and well-distributed in Al matrix.

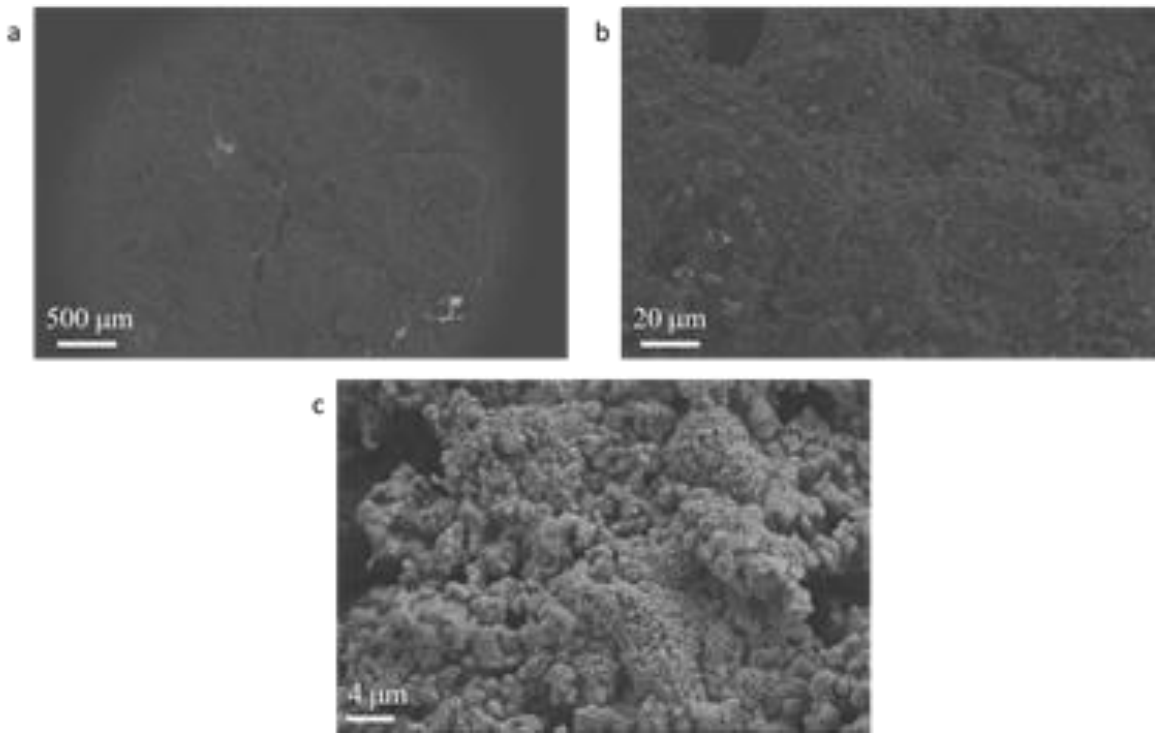

Figure 37: (a) A SEM image of Al-30 vol. % TiB_2 nanocomposite obtained after melting, (b) and (c) High magnification SEM images showing TiB_2 nanoparticles uniform dispersion and distribution.

To further confirm the presence of the designated elements in the Al-30 vol. % TiB_2 nanocomposites (after melting), EDS mapping was carried out. Figure 38 shows the EDS mapping images obtained from the Al-30 vol. % TiB_2 nanocomposite (after melting). Figure 38a presents a typical SEM image acquired from Al-30 vol. % TiB_2 nanocomposites after melting. Figure 38b and Figure 38c demonstrate EDS mapping of Ti and oxygen (O) elements, respectively.

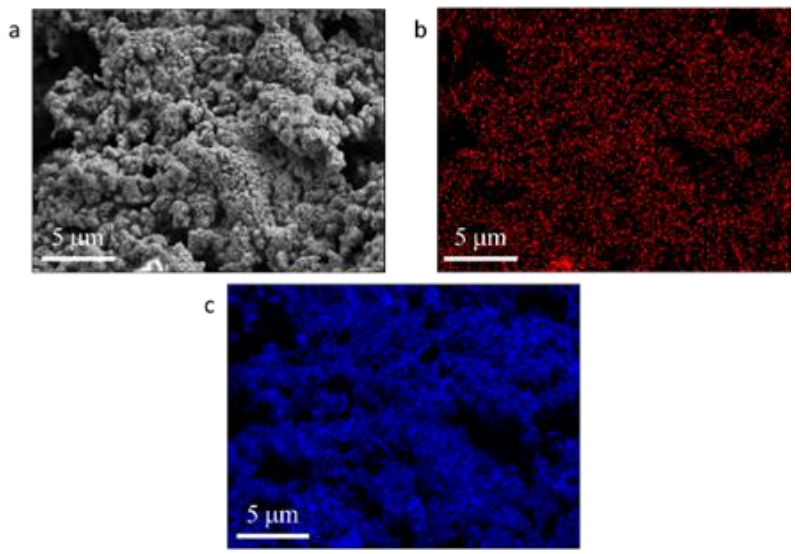

Figure 38: (a) A typical SEM image taken from Al- 30 vol. % TiB_2 nanocomposites after melting, (b) and (c) EDS mapping images show the Ti and O elements.

Figure 39 shows the Vickers hardness test results on Al-30 vol. % TiB_2 nanocomposite samples. Al NC-1, Al NC-2, and Al NC-3 are corresponding to 20, 40, and 60 min melting time, respectively. As the melting time of the pellet increases the hardness value decreases. This can be associate to the oxidation of the Al microparticles resulting in formation of more of brittle porous structure.

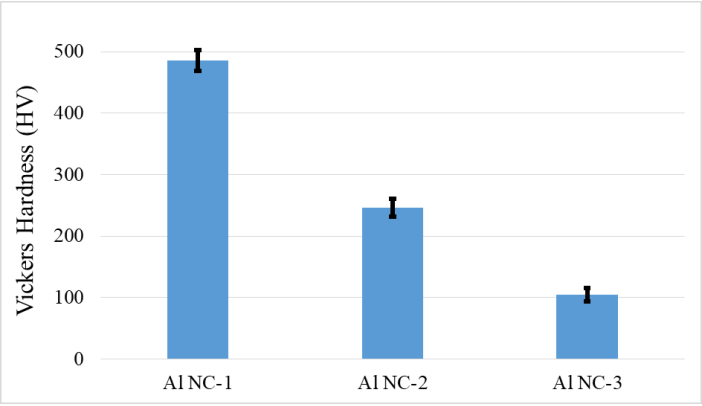

Figure 39: Vickers hardness test results on three different Al-30 vol. % TiB_2 nanocomposites. Al NC-1: Al-30 vol. % TiB_2 (20 min melting time), Al NC-2: Al-30 vol. % TiB_2 (40 min melting time), and Al NC-3: Al-30 vol. % TiB_2 (60 min melting time).

5.3 Summary

We successfully demonstrated that high concentration of ceramic nanoparticle reinforcements can be effectively incorporated in two most common lightweight metallic systems (in powder form), Al and Mg. Reinforcing metal microparticles with high performance ceramic nanoparticles is the area of interest for many applications specifically in metal-based laser additive manufacturing. A scalable approach to synthesize metal nanocomposite microparticles can open-up a new pathway for metal-based 3D printing of lightweight metals with unusual mechanical, thermal, chemical and electrical properties. Al-30 vol. %TiB_2 nanocomposites (after 20 min melting) exhibit average Vickers hardness of 485 HV (pure Al has Vickers hardness of 25 HV). This unusual Vickers hardness enhancement can be attributed to, a) uniform dispersion and distribution of TiB_2 nanoparticles in Al matrix, and b) the strong bonding between TiB_2 nanoparticles and Al matrix.

CHAPTER 6. BULK MAGNESIUM NANOCOMPOSITES

Magnesium is a low density light-weight metal, which is an important metal used in various industries such as biomedical industry [96] construction [97], naval [98] and electronic [99], and defense [100]. MMNCs is of a potential approach to produce bulk Mg nanocomposites [104]. However, scalable manufacturing of bulk Mg nanocomposites with uniformly dispersed and distributed nanoscale reinforcement is of a grand challenge to this date [107]. Adding suitable nanoparticle reinforcements into Mg matrix can substantially enhance the mechanical properties of Mg matrix. In particular, nanoparticles can significantly improve strength while maintaining or in some cases improving plasticity of metals [102, 103].

Many studies have been conducted to effectively incorporate suitable nanoparticles into Mg matrix by various approaches such mechanical shearing [108, 109], ultrasonic assisted [4, 106], salt-assisted [110, 111], spark plasma sintering [54] and powder metallurgy [112, 113]. However, it is extremely difficult to achieve a uniform dispersion and distribution of nanoparticles in Mg matrix [114-117]. In this chapter, it was demonstrated that TiC nanoparticles can be self-incorporated and self-dispersed in Mg matrix via a salt-assisted liquid state processing. Different loadings of TiC nanoparticles into Mg matrix were designed and achieved. The microstructure characterization indicates that TiC nanoparticles are uniformly dispersed and distributed in Mg matrix.

6.1 Experimental Procedure

6.1.1 Materials and Methods

In this study, TiC nanoparticles with an average size of 60 nm (US Research Nanomaterial Inc.) and high purity Mg (99.99%) ingots were chosen as the nanoparticle reinforcement and light-weight matrix, respectively. Different volume fractions (i.e. 10, 20, and 30 vol. %) of the TiC were designed into Mg matrix. TiC nanoparticles and magnesium chloride ($MgCl_2$) flux were mechanically mixed for 5 hours in a glass beaker by mechanical shaker. Mixture was then dehydrated in a vacuum oven at 150 °C for 2 hours. An electrical resistance furnace was used to melt the Mg ingots at 830 °C under a gas mixture flow of the Sulfur hexafluoride (SF_6) and argon (Ar) (99:1 vol. %). The mixed powders were gradually added to the melt surface by a stainless steel spoon. Upon complete melting of the flux, the melt was stirred at 300 rpm for 30 min by a stainless steel impeller. The melt was naturally cooled down to room temperature under SF_6/Ar gas protection. The final product in the shape of a disk (38 mm in diameter and 25.4 mm in height) was carefully extracted from the graphite crucible. Mg-10, 20, and 30 vol. % TiC nanocomposites were successfully produced. Pure Mg was also produced following a similar experimental procedure as a control. Figure 40 illustrates the schematic of the experimental setup used for this experiment.

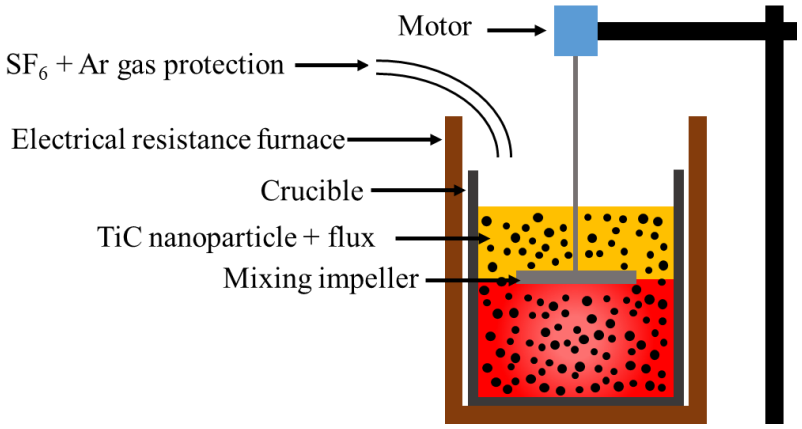

Figure 40: Schematic of the casting experimental setup.

The nanocomposite ingots were then re-melted and maintained at 850 °C under the SF_6+Ar gas protection for two hours, to facilitate the $MgCl_2$ decompositions (minimize the flux entrapment inside the Mg-TiC nanocomposite samples).

6.2 Results

Figure 41 shows the typical SEM images obtain from Mg-TiC nanocomposite samples. From the image one can clearly infer that the TiC nanoparticles are uniformly dispersed and fairly distributed in Mg matrix. The chloride flux enhances the TiC nanoparticles feeding and incorporation efficiency by dissolving the oxide layer formed on the surface of the molten Mg during the liquid state processing.

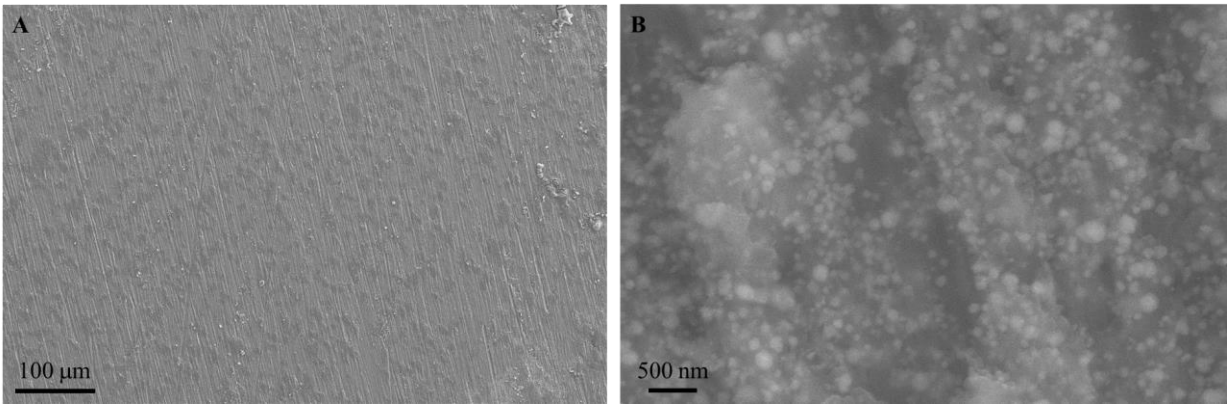

Figure 41: (A) A typical low-magnification SEM image obtained from Mg-TiC nanocomposites, and B) A high magnification SEM image acquired from Mg-TiC nanocomposites.

EDS study were conducted on the Mg-TiC nanocomposite samples with various nanoparticle volume fractions (Figure 42A). EDS results (Figure 42B and Figure 42C) confirm the presence of the Mg and TiC nanoparticles. However, there exists small amount of the Cl element (less than one volume percent in most nanocomposite samples) in EDS results, which can be attributed to the trapped $MgCl_2$ flux in Mg-TiC nanocomposite samples (Figure 42D).

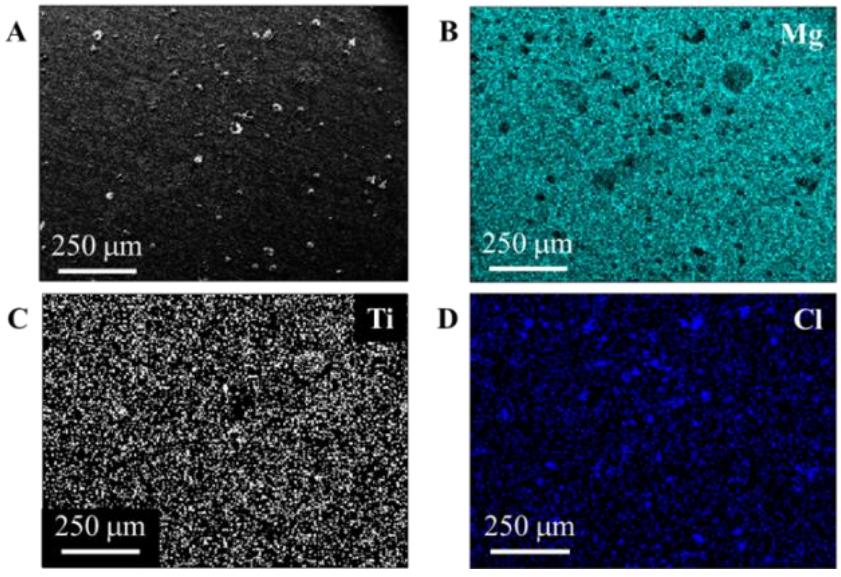

Figure 42: (A) A typical SEM image obtained from Mg-TiC nanocomposites, (B), (C) and (D) EDS mapping results showing the Mg, Ti, and Cl, respectively.

Multiple samples were prepared from Mg-10, 20 and 30 vol. % TiC nanocomposites for Vickers hardness test. The Vickers hardness of the Mg-TiC nanocomposites increase as the volume fraction of the TiC nanoparticles increases. Figure 43 shows the Vickers hardness of the Mg-TiC nanocomposites. The Vickers hardness of the sample increases as the volume fraction of the TiC nanoparticles increases which can be attributed to the strengthening effect caused by TiC nanoparticles.

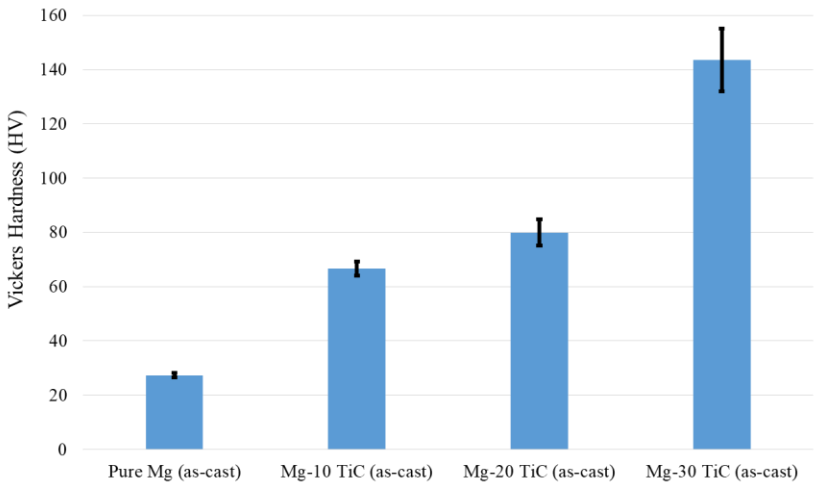

Figure 43: Vickers hardness of Pure Mg and Mg-TiC nanocomposites with various concentration of TiC nanoparticles.

6.3 Discussion

The TiC nanoparticles can be self-dispersed in molten Mg due to the reduced van der Waals forces between the nanoparticles in molten Mg, a high thermal energy of the nanoparticles, and a high energy barrier preventing nanoparticles from sintering due to good wettability between nanoparticles and Mg melt. For two TiC nanoparticles in the magnesium melt at 1100 K, the van der Waals interaction can be approximately estimated by the following equation:

$$W_{vdw}(D) = -\frac{(\sqrt{A_{TiC}}-\sqrt{A_{Mg}})^2}{12D}(R) \qquad \text{Equation 1}$$

Where D is the distance between two nanoparticles in nanometers, A_{TiC} and A_{Mg} are the Hamaker constants and are 238 zJ [154] and 206 zJ [155] for TiC and molten magnesium, respectively. R is the nanoparticle radius assuming two nanoparticles with an identical radius. Equation 1 is only effective when two TiC nanoparticles interact in the molten Mg with D larger than two atomic layers (~ 0.4 nm). Therefore, the maximum attraction, $W_{vdw\,min}$ (D) between two TiC nanoparticles in magnesium melt, is estimated to be −14.4 zJ (when D = 0.4 nm). When the difference between Hamaker constant of nanoparticles and molten metal is small, the van der Waals attraction potential is a small value**.** The thermal energy of nanoparticles due to Brownian motion, E_B, can be calculated by E_B=*k*T. Where *k* is the Boltzmann constant and T is the absolute temperature. At the processing temperature (1103 K), E_B is about 15.3 zJ.

The energy barrier between two nanoparticles in a molten metal can be estimated from the equation 2 [156].

$$W_{barrier} = 2\pi RD(\sigma_{NP} - \sigma_{PL}) \qquad \text{Equation 2}$$

Where σ_{NP} is the surface energy of TiC nanoparticles (1.35 J/m^2) and σ_{PL} is the interfacial energy between TiC nanoparticles and molten Mg (0.8 J/m^2) [156]. The $W_{barrier}$ for Mg-TiC system is about 4200zJ which is more than 2800 times greater than the *k*T values. Therefore, TiC nanoparticles can freely move inside the molten Mg and overcome the van der Waals attraction. This is in good agreement with our experimental results.

6.4 Summary

Conventional manufacturing approaches to produce high strength Mg have reached certain fundamental limits, resulting in limited advances in new generation of bulk Mg suitable for novel applications. This study showed that a suitable nanoparticle, TiC, can be effectively incorporated into Mg matrix via flux assisted liquid state processing. Bulk Mg-TiC nanocomposites with average Vickers hardness of 143.5±11.5 HV was successfully produced. Theoretical study further confirmed that not only TiC nanoparticles can be efficiently incorporated in Mg matrix, they also can be self-dispersed. This novel method has a promising potential for mass production of Mg nanocomposites with significantly improved mechanical properties to serve a wide range of industries.

CHAPTER 7. ALUMINUM NANOCOMPOSITE ELECTRICAL CONDUCTOR

This chapter presents theoretical and experimental studies on the effect of nanoparticles on mechanical and electrical properties of Al nanocomposite electrical conductors (ANECs). It is demonstrated TiB_2 nanoparticles was successfully incorporated in pure Al matrix via flux-assisted liquid-state processing.

7.1 Theoretical Study on Al-TiB_2 ANECs

7.1.1 Theoretical Calculation of Strength

Strengthening mechanism in the MMNC can be divided in two categories: Direct strengthening from the load being transferred from matrix to the reinforcing medium and indirect strengthening from the impact of the reinforcement medium on the matrix microstructure or deformation. Deformation mismatch between matrix and reinforcement leading to dislocation strengthening is an example of indirect strengthening mechanism [157]. *Chen et al.* demonstrates that, when no fine intermetallic precipitates in the MMNC fabrication processes, strengthening mechanism must be primarily due to the densely dispersed nano-reinforcements. Strengthening mechanisms in MMNCs comprise of Orowan Strengthening, Load-bearing and Hall-Petch [7].

Orowan Strengthening Contribution

The strengthening caused by the presence of nano-reinforcement medium in Al matrix can be expressed by Orowan strengthening equation [157]:

$$\Delta\sigma_{Orowan} = M\frac{0.4Gb}{\pi(1-\nu)^{0.5}}\frac{\ln(\bar{d}/b)}{(\sqrt{\pi/4V_p}-1)\bar{d}} \quad \text{Equation 1}$$

$$\bar{d} = \sqrt{2/3}\,d \quad \text{Equation 2}$$

Where M is the mean orientation factor for Al (3.06), G is the shear modulus (26 GPa), b is the Burgers vector (0.286 nm), ν is the Poisson's ration (0.33), V_p is the volume fraction of the dispersed medium and d is the average diameter of the nanoparticles [157].

Figure 44 displays a comparison between Orowan strengthening that can be achieved based on various size and volume fraction of nanoparticles in Al matrix. We anticipate to achieve 184, 275, 352, 422, 488 MPa Orowan strengthening with uniform dispersion of 1, 2, 3, 4, and 5 vol. % TiB_2 (10 nm) nanoparticles in Al matrix, respectively.

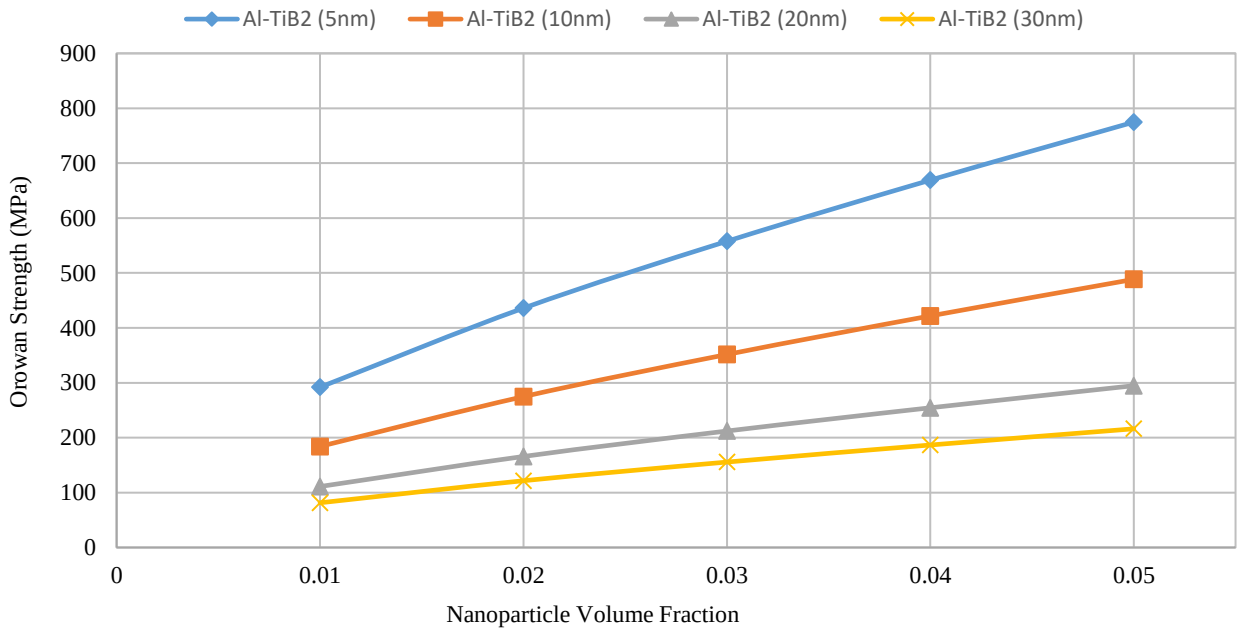

Figure 44: Theoretical calculation of Orowan Strengthening for Al-TiB_2 MMNC with various volume percent of the nanoparticle reinforcements.

Load Bearing Contribution

The increase in strength due to load bearing mechanism can be calculated by [7]:

$\Delta\sigma_{load} = 1.5\, V_p \sigma_i$

σ_i is the interfacial bonding strength between the matrix and nanoparticles.

Hall-Petch Contribution (grain refinement)

Hall-Petch relationship (shown in equation 3) can be used to calculate the strengthening mechanism due to grain refinement [7].

$$\sigma_y = \sigma_0 + K_y/\sqrt{d} \qquad \text{Equation 3}$$

Where σ_y is the final strength value after considering the effect of grain size, σ_0 is the initial strength value, K_y is a constant and d is the mean grain size. K_y value is 0.22 MPa$\sqrt{m}$ [157].

7.1.2 Theoretical Study on Electrical Resistivity

Classical electrical conductivity theory is based on the free electrons that move throughout lattice of the metals. Considering Drude's free electron theory [158], electrons are free to move in every direction within the metal lattice by following Newton's laws of motion and Maxwell-Boltzmann statistics [159]. Electrical resistivity and electron mean-free-path (MFP) of a given metal are constant values. MFP is inversely proportional to the electron scattering probability. The electrons interaction with lattice and inclusion (defect) promotes electron scattering, consequently lead to increase of electrical resistivity. According to the Matthiessen's rule, the electrical resistivity of metals is the summation of two main parts: thermal (ρ_T) and residual (ρ_R). The ρ_T refers to environment temperature of the metal. The ρ_R is associated with the microstructure of the metallic systems that contributes to electron scattering such as lattice scattering (due to phonon-electron interaction), the impurity scattering, precipitate scattering, and the grain boundary scattering [160, 161]. One can conclude that electron scattering and consequently electrical conductivity reduction is inevitable. More theoretical discussion will be presented in the results section of this chapter.

7.2 Al Nanocomposite Electrical Conductors (ANECs)

7.2.1 Manufacturing of ANECs

In this study, high purity Al (99.99%) ingots and in-house synthesized TiB_2 nanoparticles with an average size less than 10 nm were used as matrix and nano-reinforcement, respectively. TiB_2 nanoparticles and potassium aluminum fluoride ($KAlF_4$) flux were mechanically mixed at solid state for 3 hours. Mixed powders were dehydrated at 120 ºC for 1 hours in a vacuum oven. An electrical resistance furnace was used to melt the Al ingots at 900 ºC under argon (Ar) gas flow protection. The mixed powders were gradually added to the melt surface and melt was mechanically stirred at 200 rpm for 10 minutes with a one-inch dimeter graphite mixing blade. The melt was naturally cooled down to room temperature under Ar gas protection.

The final product was (in the shape of a disk with 1.5 inches in diameter and 1.0 inch in height) carefully extracted from the graphite crucible. Al-X vol. % TiB_2 (X=3, 5, and 10) nanocomposites were produced (three study samples were prepared from top, middle, and bottom of each nanocomposite sample). Figure 45 shows the schematic of the experimental set up to produce Al nanocomposites.

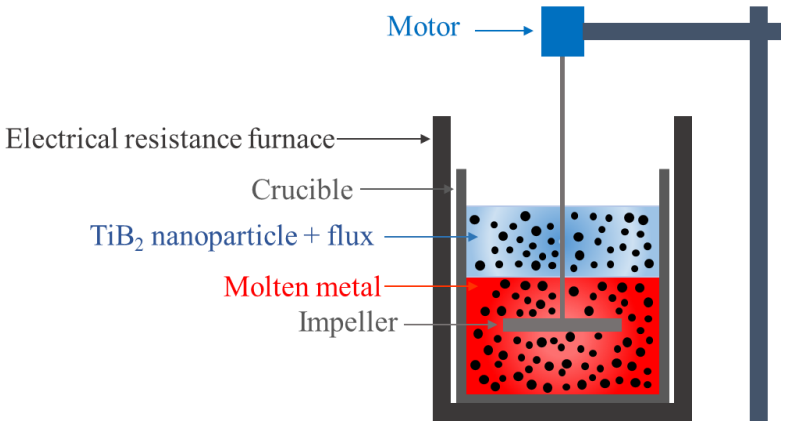

Figure 45: Schematic of the experimental set up to produce Al nanocomposites.

The final product was (a disk with 1.5 inches in diameter and 1.0 inch in height) carefully extracted from the graphite crucible. Al-X vol. % TiB_2 (X=3, 5, and 10) nanocomposites were successfully produced (three study samples were prepared from top, middle, and bottom of each nanocomposite samples).

Scanning electron micrographs (SEM) were acquired using a ZEISS Supra 40VP field emission microscope operating at 10 kV and Energy-dispersive X-ray spectroscopy (EDS) mapping was performed in the same SEM field emission microscope. TEM was carried out using a TF20 High-Resolution EM, CryoEM and CryoET (FEI) electron microscope operating at 300 kV. Focused ion beam (FIB) was used to reveal the nano-level structures. Electrical conductivity was measured by CDE ResMap 178 4-Point Probe.

7.2.2 Characterization of ANECs

Three study samples were prepared from each Al nanocomposites. Samples were ground and polished following Buehler standard method. Study samples were prepared for SEM and TEM characterization. Figure 46a, Figure 46b and Figure 46c show a typical Al-TiB_2 nanocomposite sample. Figure 46d shows the two SEM samples prepared from the nanocomposite ingot. To

clearly reveal the nanoparticles, the SEM samples were processed by a low-angle ion milling (10°, to remove the nanometre-sized polishing powders).

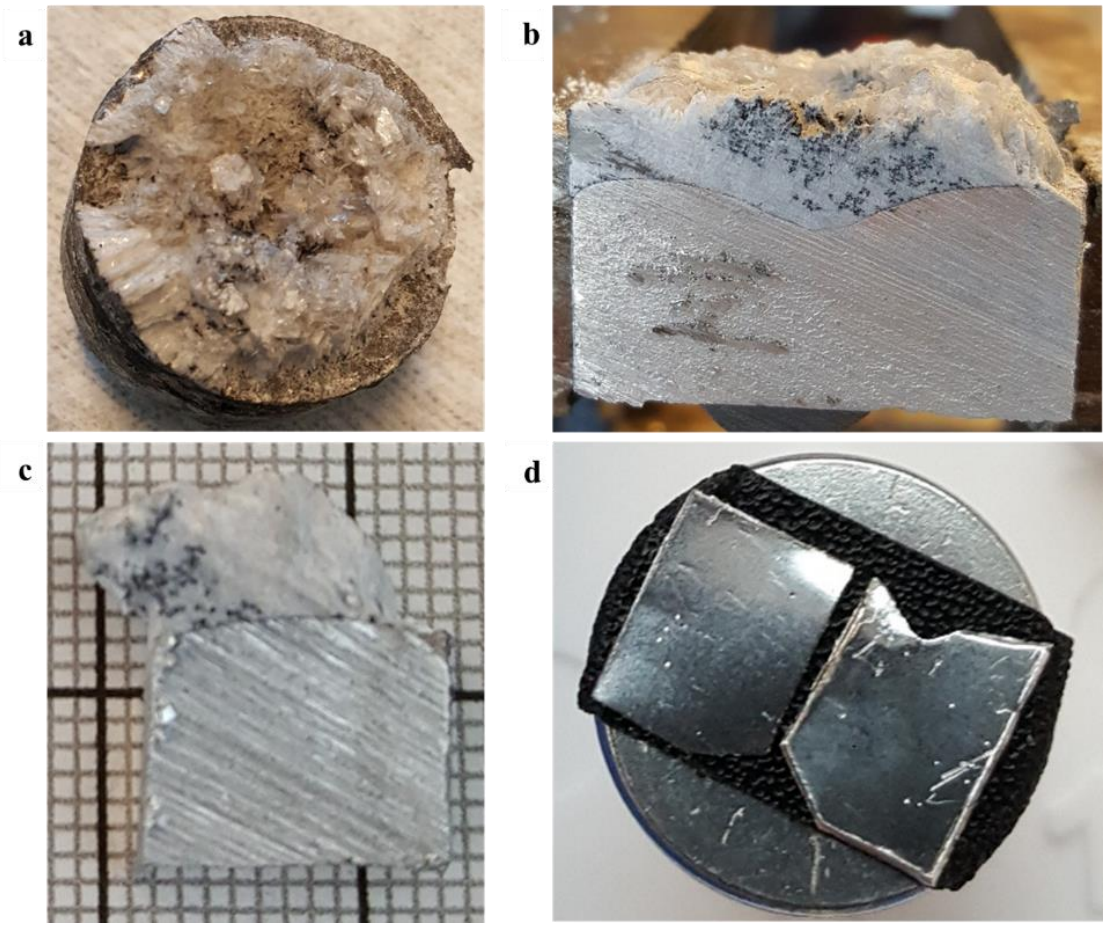

Figure 46: (a) Al-3 vol. % TiB_2 nanocomposites ingots, (b) Al-TiB_2 nanocomposite sample is cut into half, (c) A study sample prepared from the Al-TiB_2 nanocomposites, and (d) Two SEM study samples prepared from Al-TiB_2 nanocomposites.

We first characterized the distribution and dispersion of the TiB_2 nanoparticles in as-casted Al-TiB_2 nanocomposite samples using scanning electron microscopy. SEM images of the Al-TiB_2 nanocomposite are shown in Figure 47. Figure 47a shows high volume fraction of the TiB_2 nanoparticles uniformly dispersed and distributed in the aluminum matrix. Higher magnification SEM images illustrate that the TiB_2 nanoparticles are retaining their original size without any sintering (Figure 47b).

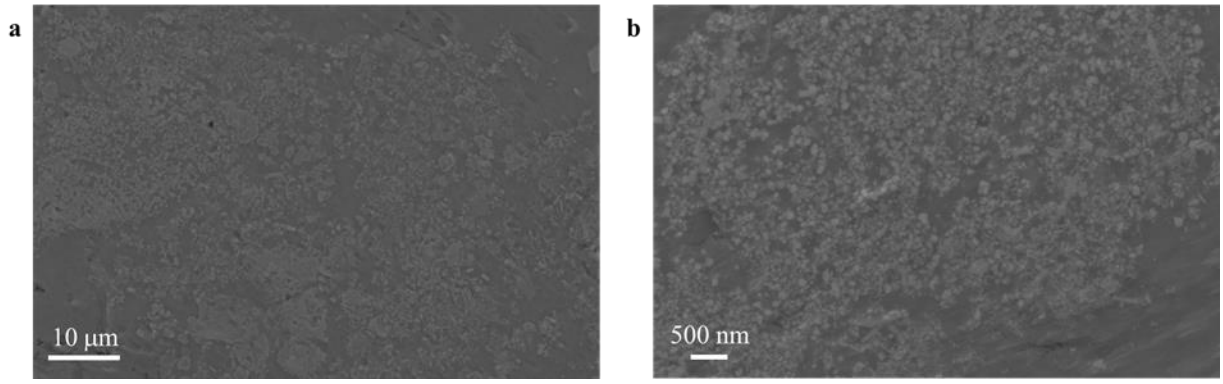

Figure 47: (a) A SEM image obtained from Al-TiB_2 nanocomposite sample, (b) A High magnification SEM image acquired from the Al-TiB_2 nanocomposites.

Focused ion beam was used to cut several micron-size trenches into the Al nanocomposite samples. The underneath morphology of the aluminum nanocomposite samples revealed a surprising phenomenon. The size of the grain in as-cast and low cooling rate Al nanocomposite samples have reached ultrafine scale (less than 1 μm). The smallest grain size observed is about 300 nm. This unusual phenomenon is associated with the presence of the TiB_2 nanoparticles acting both as nucleation sites to decrease the grain size and more importantly pinning down the growth of the aluminum grains and retaining them in ultrafine grain size. Figure 48a shows a thin sheet of Al nanocomposite milled by FIB (the sample is prepared from bulk Al-TiB_2 nanocomposites). Figure 48b shows high magnification SEM images clearly representing nano-sized aluminum grain in slow cooling.

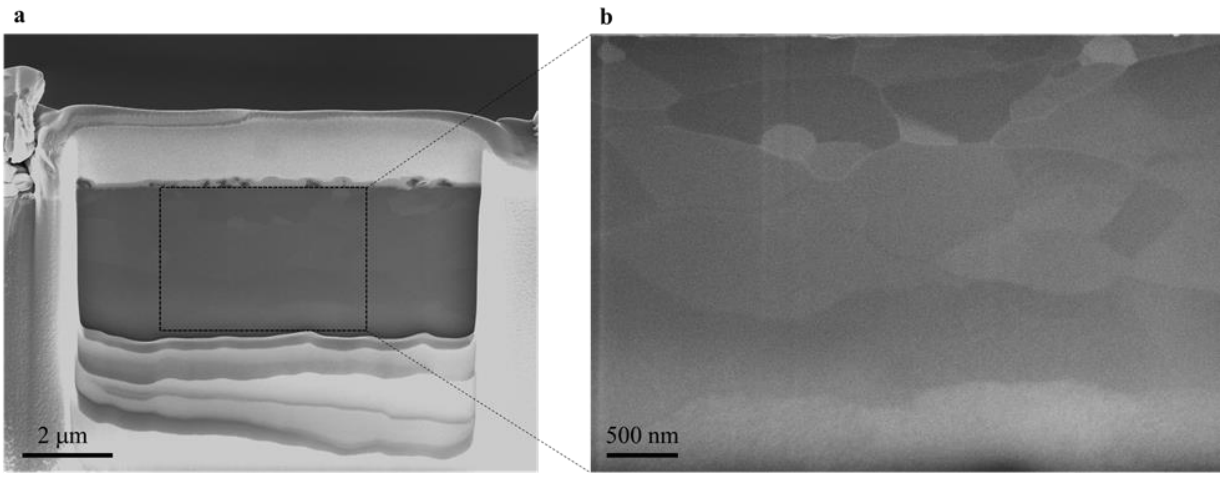

Figure 48: (a) Al-TiB_2 nanocomposite thin film prepared by FIB, and (b) A High magnification SEM image vividly shows the ultrafine grain in Al nanocomposites.

7.3 Results and Discussion on ANECs

7.3.1 Mechanical Property

Figure 49 shows the Vickers hardness (HV) versus electrical conductivity (% IACS) results for pure Al and Al-TiB_2 nanocomposites with three different concentrations of TiB_2 nanoparticles. The Vickers hardness and electrical conductivity of as-cast pure Al is measured to be 25±3 and 62±1 % IACS ($2.8\mu\Omega.cm$) respectively, which are set as the reference points for the Al-TiB_2 nanocomposite systems. Both tests were carried out at room temperature (25 °C) with a constant humidity of about 38%. As the volume percent of the TiB_2 nanoparticles increase, nanocomposite exhibits a greater Vickers hardness. This can be associated to the addition of the hard TiB_2 nanoparticles. On the other hand, TiB_2 nanoparticles as act electron scattering point in Al nanocomposites which result in a reduction of electrical conductivity. The electrical conductivity of Al-3, 5, and 10 vol. % TiB_2 nanocomposites were measured to be 57.0%, 43.6%, and 41% IACS, respectively.

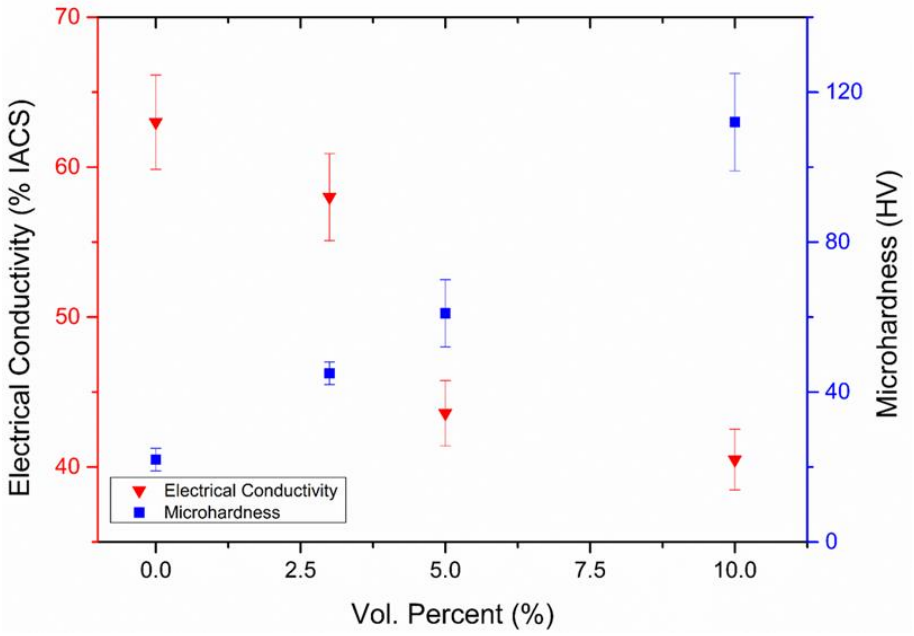

Figure 49: The effect of TiB_2 nanoparticles on mechanical and electrical properties of the pure Al and Al-TiB_2 nanocomposites.

Figure 50 shows a comparison between commercially available electrical conductors and Al-TiB_2 nanocomposites. One can empirically conclude that as the volume percent of the TiB_2 nanoparticles increases, the Vickers hardness value increases. The Al-10TiB_2 nanocomposites have high Vickers hardness when compared to other commercially available electrical conductors. Al-10TiB_2 nanocomposites show more than 35 HV greater Vickers hardness compare to ACSR. Al1350-H19 (as a reference) is a grade of Al commonly used in many electrical conductor cables for high voltage DC transmission and distribution lines.

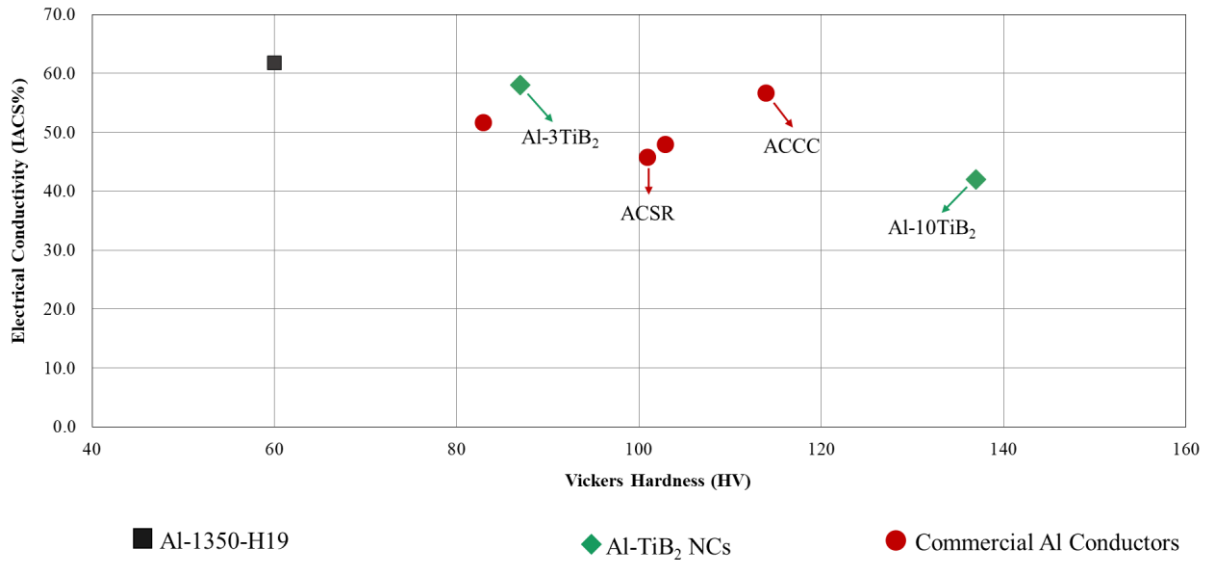

Figure 50: Comparison between electrical conductivity and Vickers hardness for commercially available electrical conductor cables (red), Al-TiB_2 nanocomposites (green) and Al1350-H19 (dark gray).

We also prepared several tensile test bars to measure the tensile properties of the Al-TiB_2 nanocomposites. The as-cast ingots were rolled by an 80% reduction to Al nanocomposite plates. Electric discharge machine (EDM) was utilized to cut the tensile bars from the Al nanocomposite plates. Tensile bars with dimension of 40 mm length, 8 mm width, and gage length of 10 mm were prepared (Figure 51).

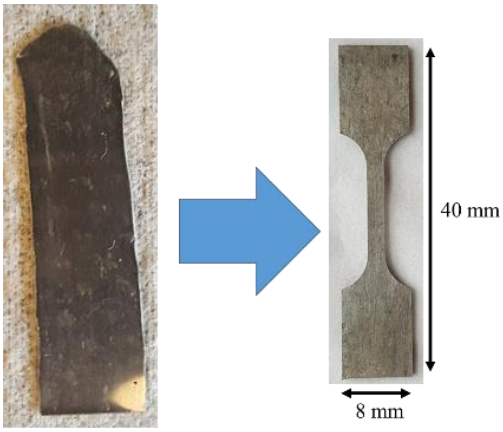

Figure 51: A typical tensile bar prepared from as-cast bulk Al-TiB_2 nanocomposites.

Table 4 shows the tensile test and electrical conductivity results on several samples prepared from Al-3TiB_2 and Al-10TiB_2 (pure Al results are obtained from the literature). It was expected to observe significantly improved tensile properties in the case of Al-10TiB_2 nanocomposites, however $KAlF_4$ flux entrapment partially degraded the property improvement. The flux remnant inside the Al-10TiB_2 nanocomposite samples resulted in moderate mechanical property improvement compare to pure Al. The best results were obtained from Al-3TiB_2 nanocomposites with yield strength of 209.6MPa, UTS of 219.6MPa, and electrical conductivity (σ) of 57.5 %IACS.

Table 4: Comparison between Pure Al and as-cast Al-TiB_2 nanocomposites.

Material	Yield Strength (MPa)	UTS (MPa)	Tensile Strain (%)	σ (%IACS)
Pure Al	35	90	12	62.5
Al-3TiB_2	205 ±3	212±4	4 ±1	56 ±1
Al-10TiB_2	165 ±5	189 ±4	2 ±1	41 ±3

To further investigate the amount of flux remnant inside the Al-10TiB_2 nanocomposite samples, the tensile bars were studied under SEM after the tensile tests. Figure 52a shows a typical SEM image acquired from the fracture surface. EDS point analysis result (Figure 52b, Figure 52c,

and Figure 52d) confirms the presence of the $KAlF_4$ flux (less than one volume fraction) inside the Al-TiB_2 nanocomposites.

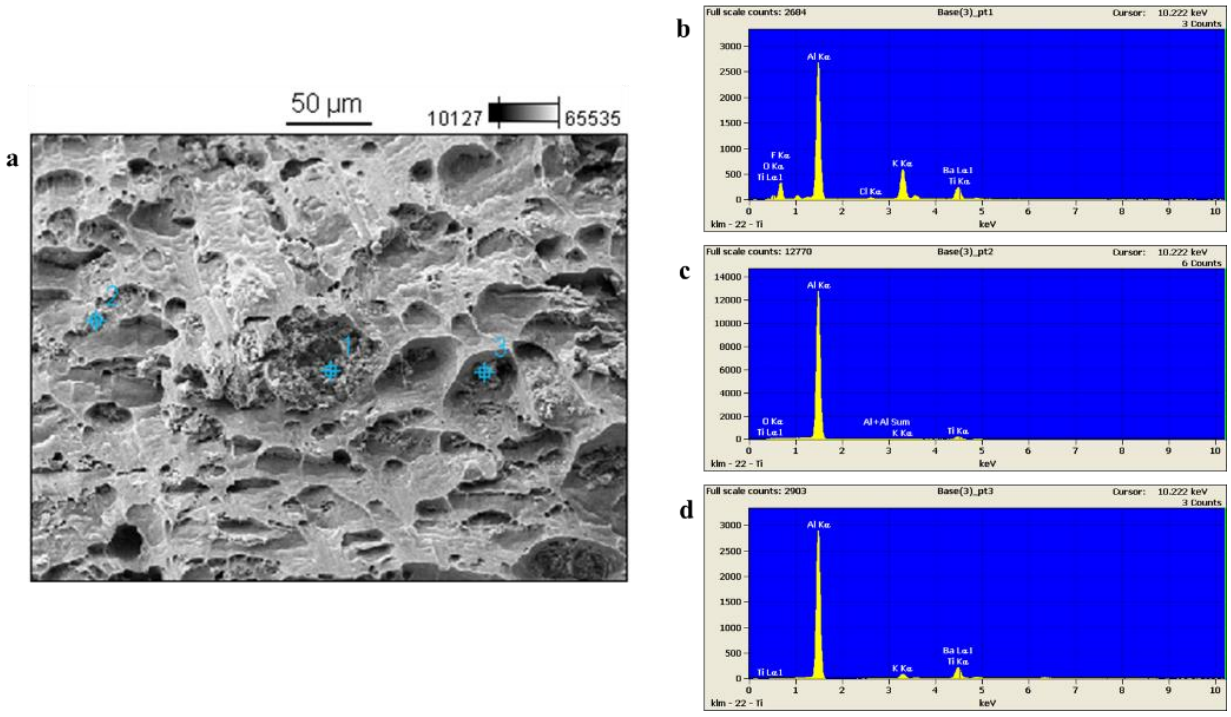

Figure 52: (a) A SEM image acquired from the fracture surface of the Al-10TiB_2 nanocomposite tensile bar, (b), (c), and (d) EDS results obtained from three different locations of the fracture surface.

7.3.2 Electrical Property

Classical electrical conductivity theory is based on the free electrons that move throughout lattice of metal. Considering Drude's free electron theory [158], electrons are free to move in every direction within the metal lattice by following Newton's laws of motion and Maxwell-Boltzmann statistics [159]. Electrical resistivity and electron mean-free-path of a given metal are constant values. MFP is inversely proportional to the electron scattering probability. The electrons interaction with lattice and inclusion (defect) promotes electron scattering, consequently lead to increase of electrical resistivity. According to the Matthiessen's rule, the electrical resistivity of

metals is the summation of two main parts: thermal (ρ_T) and residual (ρ_R). The ρ_T refers to environment temperature of the metal. The ρ_R is associated with the microstructure of the metallic systems that contributes to electron scattering such as lattice scattering (due to phonon-electron interaction), the impurity scattering, precipitate scattering, and the grain boundary scattering [160, 161]. When comparing the conventional strengthening mechanism approaches, one can conclude that electron scattering and consequently electrical conductivity reduction is inevitable.

For metals such as Al, the electrical conductivity analysis can be carried out with Drude model by:

$$S_0 = \frac{n\tau e^2}{m^*}$$

Where S_0 indicates the matrix electrical conductivity without nanoparticle incorporation under the same temperature conditions, τ is the relaxation time of the free mobile electrons in matrix, e is the charge every electron carries, m^* denotes the effective mass of the electrons, and n is the number density of the electrons which is the key parameter to determine the electrical conductivity. According to the Nordheim's rule [162, 163], the electrical conductivity of the nanocomposites can be written as:

$$\frac{1}{S} = \frac{1}{S_0} + k_1 x(1-x) + k_2 x$$

S is the electrical conductivity of the nanocomposites, $k_1$represents the nanoparticle-metal interaction, and k_2 corresponds to the effect of the nanoparticles as a secondary phase in electrical conductivity. And x is nanoparticle volume fraction.

Figure 53 present schematic of the electrons pathway inside a metal matrix nanocomposites. Due to the topographical impedance on the current density pathway will block the transport of electrons. At macroscopic view, k_2 will be greater than k_1 (especially for $x < 0.2$).

The nanoparticles interaction in matrix is negligible (both physically such as Gibbs free energy change, interfacial energy change, phase transition energy, and chemically such as chemical reactions, electronic structure tuning) [164] as a result, the nanoparticle phase will play a dominant role in the electrical conductivity of the nanocomposite.

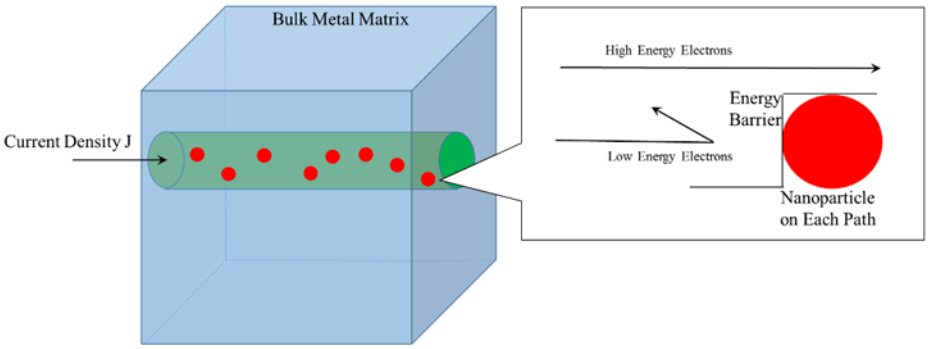

Figure 53: The schematic of the electron scattering mechanisms in Al-TiB_2 metal matrix nanocomposites (The left side indicates the structural impedance by nanoparticle incorporation; whereas the right side demonstrates the interfacial energy barrier formed by Al and TiB_2)

Furthermore, the valence electrons are different in Al matrix and metal-like TiB_2, which leads to the deviation from linearity ("Linearity" indicates the approximation of electrical resistivity associated with $k_2 x$) for the electrical conductivity and nanoparticles volume fraction.

Another important factor is the interfacial scattering at the Al and TiB_2 nanoparticle boundaries. This is supported by the sharp slope change at the point of 3 vol. % to 5 vol. % TiB_2 nanoparticles (Figure 49), which indicates the interface plays a crucial role, when the incorporated nanoparticle reaches a certain volume percent. In the case of high volume fraction (~ 0.03 to 0.05) of the nanoparticles in Al matrix, the transporting electrons have greater chances to encounter the energy barrier between metal matrix and nanoparticles. Thus, the electrical conductivity reduces more drastically. This scattering is mainly due to the interfacial contact. Al and TiB_2 have free electrons at different energy levels and different electronic band structures [164, 165], and the

contact of these two will present an energy difference which scatter the mobile electrons [166]. When lower energy electrons encounter the Al-TiB_2 interface, they will be scattered during transport which reduces the electrical conductivity of the Al nanocomposites, due to the band-bending at the interface [164, 166, 167].

In Al-TiB_2 metal matrix nanocomposites, the electrical conductivity reduction is due to both the structural influence from the incorporation of TiB_2 nanoparticles and the energy structure difference between Al and TiB_2 nanoparticles. Since TiB_2 nanoparticles act as a second phase in Al matrix and have mobile free electrons with different energy levels in different electronic structures (compare to Al), the electrical conductivity reduction is inevitable.

7.3.3 Theory of TiB_2 Nanoparticle Dispersion in Molten Al

In our nanoparticle-molten metal model system, nanoparticles are assumed to be uniformly distributed and dispersed in a molten metal. For simplicity, only interactions between two identical nanoparticles in a molten metal are considered (Figure 54). The model assumes: 1) Nanoparticles with a radius R are spherical in shape and D is the gap between two nanoparticles, 2) no microscopic convection in the melt near the nanoparticles, 3) negligible electrostatic interaction or double layers between the nanoparticles and molten metal, 4) negligible buoyance and gravity forces on nanoparticles, 5) no severe chemical reaction between the nanoparticles and molten metal, and 6) no gas film or contamination on the surface of the nanoparticles.

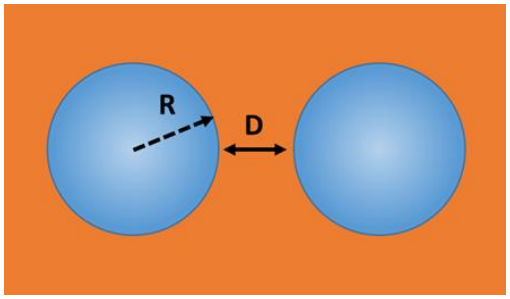

Figure 54: Model for two identical nanoparticles interacting in a molten metal.

Based on the above assumptions, three major interactions: interfacial energy, van der Waals potential, and Brownian potential, are considered in this model system.

When two nanoparticles interact in a molten metal far from each other, the interfacial energy is

$$G_b = 2S_{pl}\sigma_{pl} \qquad (1)$$

where S_{pl} is the surface area of a nanoparticle and σ_{pl} is the interfacial energy between the nanoparticle and molten metal. If the two nanoparticles travel toward each other to push all metal atoms out and create a void between them, the interfacial energy would be

$$G_b = 2(S_{pl}-S_{pp})\sigma_{pl} + 2S_{pp}\sigma_p \qquad (2)$$

Where S_{pp} and σ_p are the effective contact area and the surface energy of the nanoparticles, respectively. If the two nanoparticles attain an adhesive contact to chemically bond (i.e. sintering starts), there will be no physical interface between the two nanoparticles. We consider this global energy minimum to be zero. Therefore, when two nanoparticles move close enough to squeeze metal atoms out and create a void between them, the change in Gibbs free energy can be described as

$$\Delta G_1 = 2S(\sigma_p - \sigma_{pl}) \qquad (3)$$

where S is the effective contact area. If the nanoparticles move further close to start chemically bond with each other, the change in Gibbs free energy can be written as

$$\Delta G_2 = -2S\sigma_p \qquad (4)$$

Since the interfacial energy is always positive, ΔG_2 would be always negative. Hence, a general expression for the interaction potential of two similar surfaces of a unit area along with the gap between them (D) can be expressed as:

$$W_{inter}(D) = 2S(\sigma_p - \sigma_{pl})\, e^{-(D-D_0)/a_0} \frac{D-a_0}{D_0-a_0}, \text{ for } (D_0 < D < a_0) \quad (5)$$

$$W_{inter}(D) = -2S\sigma_p e^{D/a_0}(1 - D/D_0) + 2S(\sigma_p - \sigma_{pl}), \text{ for } (0 < D < D_0) \quad (6)$$

where D_0 is the chemical length bond, and a_0 is the characteristic decaying length (0.2~0.4 nm) for the chemical bond.

The van der Waals potential between two nanoparticles in a molten metal is of a relatively long range (0.2-9 nm). Nanoparticles tend to attract each other due an attract force induced by van der Waals potential. The van der Waals potential for two identical spheres of radius R and is determined by [156, 168]

$$W_{vdw}(D) = -\frac{AR}{12D} \quad (7)$$

where A is the system Hamaker constant for the nanoparticle interactions in the molten metal. To estimate the Hamaker constant A below equation can be used

$$A = (\sqrt{A_{NP}} - \sqrt{A_L})^2 \quad (8)$$

Where A_{NP} is the Hamaker constant for nanoparticle, and A_L is the Hamaker constant for metal. Therefore, the van der Waals potential can be written as

$$W_{vdw}(D) = -\frac{(\sqrt{A_{NP}}-\sqrt{A_L})^2}{12D}(R) \quad (10)$$

The energy barrier between two nanoparticles in a molten metal can be estimated from the equation 2 [156].

$$W_{barrier} = 2\pi RD(\sigma_{NP} - \sigma_{PL}) \quad (11)$$

Since nanoparticles are very small in size, they are free to move randomly under thermal fluctuations. Thus, Brownian potential need to be considered for these small nanoparticles. Equi-

partition theorem suggests that the kinetic energy/potential of the Brownian motion is in one dimension for one particle. Therefore, the Brownian motion energy for the two nanoparticles system in on dimension is kT. For two nanoparticles in a molten metal at high temperature, may be comparable to the van der Waals potential, and thus Brownian potential would play an important role on nanoparticle dispersion.

In the model system for nanoparticle dispersion in a molten metal, the van der Waals potential, interfacial energy, and Brownian potential intrinsically co-exist. The interfacial energy dominates when the gap between two nanoparticles becomes one or two atomic layers. The van der Waals interaction dominates outside this gap until a long distance (up to 10 nm or more).

Figure 55 shows the interaction potentials for nanoparticle self-dispersion in the molten metal. If $W_{barrier}$ is high (i.e. good wettability between the nanoparticle and the molten metal) and the van der Waals potential well is not deep, the Brownian potential kT cannot drive the nanoparticles to pass the barrier for any adhesive contact, although the nanoparticles would not be kinetically trapped either. This would allow nanoparticles to move freely without forming a chemical bonds in the molten metal (self-dispersion).

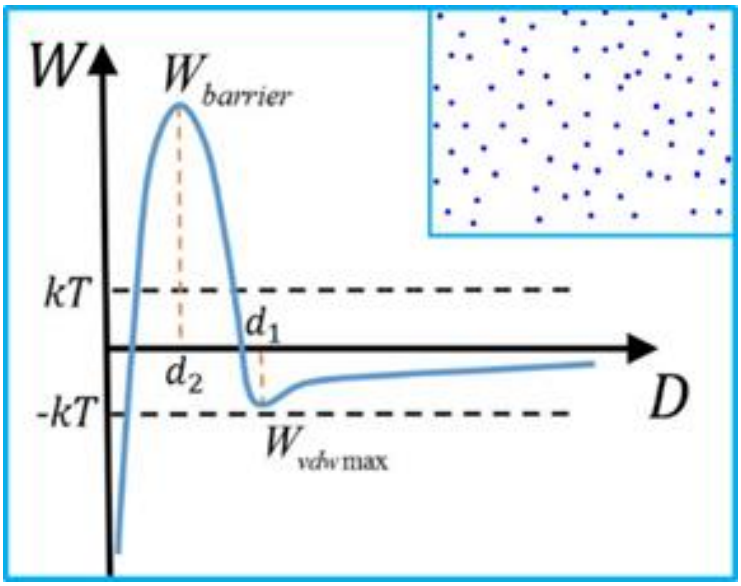

Figure 55: Interaction potentials for nanoparticles self-dispersion in molten metal with an inset to show how nanoparticles disperse in molten metal.

To further validate the self-dispersion model, Al-TiB_2 system was studied. The Hamaker constant for Al and TiB_2 is 266zJ (1zJ=10E-21 J) and 256zJ [156], respectively. And, the average size of the TiB_2 nanoparticles is 10 nm. The equation (10) is effective when only when two TiB_2 nanoparticles interact in molten Al where D is about 0.4 nm [156]. Therefore, by inserting the values into equation (10): $W_{vdw}(D) = -11.9zJ$. The thermal energy value at 900 °C (1173 K) would be 16.2 zJ. The surface energy for liquid Al and solid TiB_2 are is 1.1 j/m^2 [169] and 3.0 j/m^2 [170], respectively. And the contact angle between Al and TiB_2 is 50 degree (D_0= 0.1 nm and a_0 =0.4 nm) at that temperature. Therefore, we can calculate the $W_{barrier}$ (from equation 11) to be 2.4 x 10^3 zJ. Since the $W_{barrier}$ is more than 1500 times greater than the Brownian potential, there is a small chance for TiB_2 nanoparticles to overcome such energy barrier and adhere to one another (forming cluster). Therefore, we can conclude that TiB_2 nanoparticles can be self-dispersed and self-stabilized in molten Al. This is in good agreement with our experimental results shown in result section.

7.4 Summary

In this work, we introduce a novel and scalable approach to produce a new class of aluminum electrical wire for DC transmission lines. A suitable nanoparticle was identified and synthesized in-house to significantly improve the mechanical properties of aluminum matrix while retaining good electrical conductivity. It was shown that how small size TiB_2 nanoparticles (less than 10 nm) were effectively incorporated in Al matrix via a flux assisted liquid state processing. TiB_2 nanoparticles show uniform dispersion and distribution in the Al matrix. Al-3TiB_2 nanocomposites showed yield strength of 206.6 MPa, UTS of 219.6 MPa, tensile strain of 4.3% and electrical conductivity of 57.5% IACS compare to pure Al with yield strength of 35 MPa, UTS of 90 MPa, tensile strain of 12% and electrical conductivity of 62.5%. On the other hand, Al-10 vol. % TiB_2 nanocomposites showed average Vickers hardness of 137 HV (with 41 %IACS electrical conductivity). Mechanical property enhancement in Al nanocomposites can be attributed to the uniform dispersion and distribution of the TiB_2 nanoparticles of 10 nm in Al matrix. Also, the presence of the small TiB_2 nanoparticles allowed formation of unusual ultrafine grain sizes after cooling.

CHAPTER 8. CONCLUSIONS

This study is motivated by the rapid growing interests in the development of nanocomposites, specifically polymer matrix nanocomposites and metal matrix nanocomposites. In addition, there is a lack of fundamental knowledge of how nanoparticles interact in molten metals. This research is inspired by an intriguing hypothesis that the introduction of nanoparticles to polymer and metallic matrices can break the fundamental limits of property improvement.

For polymer metal nanocomposites, Sn metal microparticles was randomly dispersed and distributed in polymer matrix via a powder (Sn and PES) compaction followed by melting, to form PES-Sn composite preforms. Thermal fiber drawing was used to draw the composite preforms into nanocomposite fibers with embedded metal nanoparticles. Cyclic thermal drawing enabled uniform dispersion of the Sn metal nanoparticles in PES polymer matrix. After the first thermal drawing cycle, metal microfibers with various lengths were well-aligned in the longitudinal direction of composite fibers. Using a stack and draw iteration, further drawing cycles produced polymer-metal nanocomposite fibers with a uniform dispersion of Sn nanoparticles from non-uniform Sn microparticles for the first time.

Scalable synthesis of high performance and exotic ceramic nanoparticles was studied. Metal boride, specifically TiB_2 is a refractory intermetallic compounds between titanium (a transition metal) and boron. TiB_2 in the form of microparticles has demonstrated significant reinforcing capabilities in both polymeric and metallic matrices. TiB_2 nanoparticles have received wide attention due to its high hardness and stiffness, high melting point, excellent heat conductivity, oxidation stability, and chemical resistance. Small size TiB_2 nanoparticles can significantly enhance mechanical and functional properties of various matrices. However, TiB_2

nanoparticles of high purity and small size (less than 10 nm) are not commercially available. In this study, TiB_2 nanoparticles were synthesized via magnesio-reduction of titanium dioxide and boron trioxide in a eutectic chloride salts (LiCl/KCl). The synthesized TiB_2 nanoparticles were characterized via SEM, TEM, and XRD to ensure purity and size uniformity. To this date, the smallest commercially available TiB_2 nanoparticles is about 58 nm which suffers from poor purity. This study demonstrated high volume and high purity synthesis of TiB_2 nanoparticles with an average size of 8.1±0.4 nm. The in-house synthesized TiB_2 nanoparticles were utilized as reinforcement phase in Al nanocomposites production.

In this work, it was successfully demonstrated that how high concentration of nanoparticles can be effectively incorporated in two most common lightweight metallic systems, Al and Mg microparticles. Flux assisted liquid state processing with mechanical shearing enabled the incorporation of high volume fraction (up to 30 volume percent) of in-house synthesized TiB_2 and commercial TiC nanoparticles in Al and Mg microparticles, respectively. Reinforcing metal microparticles with such high performance ceramic nanoparticles can be beneficial for many applications such as laser additive manufacturing. Successful incorporation of suitable nanoparticles into metal microparticles can alter the solidification behavior of such nanocomposite materials when applied in selective laser melting. This innovative approach can open-up a new path for metal-based 3D printing of lightweight metals with unusual mechanical, thermal, chemical and electrical properties. The metal nanocomposite microparticles can also be utilized by tradition manufacturing processing to produce high strength metal with high energy efficiency. For example, the Al- 30 vol. % TiB_2 nanocomposite microparticles were compacted and melted under

vacuum to form bulk aluminum nanocomposites. The Al-30 vol. % TiB_2 nanocomposites exhibit an average Vickers hardness of 485 HV (compare to pure Al with 25 HV).

Conventional manufacturing approaches to produce high strength magnesium has reached to their fundamental limits, leading to insufficient advances in manufacturing of magnesium and its alloy suitable to meet 21st century demands. Traditional strengthening approaches such as thermomechanical processing cannot offer high strength Mg functional at high operating temperatures. For example, the precipitated phases obtained from heat treatment grow at elevated temperature, leading to strength reduction. Grain growth restriction at elevated temperature is one of the main advantages of the Mg nanocomposites. This study showed that a suitable nanoparticles, TiC, can be effectively incorporated into Mg matrix offering promising Vickers hardness of 143.5±11.5 HV (while the pure Mg has a Vickers hardness of ~ 35 HV). Theoretical analysis further confirmed that not only TiC nanoparticles can be efficiently incorporated in Mg matrix, they also can be self-disperses in Mg matrix.

Flux assisted liquid state processing was employed to effectively incorporate in-house synthesized TiB_2 nanoparticles into bulk Al metal matrix. One of the major accomplishments of this study is the design and manufacture of aluminum nanocomposites where nanoparticles can be self-assembled and self-stabilized uniformly in Al matrix to deliver high strength and electrical conductivity. For instance, Al-3TiB_2 offers a yield strength of 209 MPa, UTS of 219.6 MPa, tensile strain of 4.3 and electrical conductivity 57.5 %IACS. Another example of Al nanocomposites would be Al-10TiB_2 with an average Vickers hardness of 137 HV and 41 %IACS electrical conductivity. Al-10TiB_2 nanocomposites show more than 35 HV Vickers hardness when compared to the most common electrical conductor, ACSR.

This work conducted fundamental study on nanoparticles induced electron scattering on Al matrix, obtained a better understanding of interaction potentials between nanoparticles in molten Al, successfully synthesized uniform-size TiB_2 nanoparticles, and demonstrated a scalable manufacturing of Al nanocomposites with minimal impurities/flux contamination. Interaction potential study on Al-TiB_2 systems demonstrated that the Brownian potential (kT) is not strong enough to drive the TiB_2 nanoparticles (which has a good wettability with Al matrix) to pass any adhesive contact barrier, preventing nanoparticles from sintering. In addition, theoretical and experimental studies were presented in this work to show the effect of nanoparticles on mechanical properties of metal matrices. Mechanical property enhancement can be associated with the presence of 10 nm TiB_2 nanoparticles in Al matrix, and more importantly formation of ultra-fine aluminum grains. Obtaining ultra-fine aluminum grains under slow cooling is of tremendous interests.

CHAPTER 9. RECOMMENDATIONS FOR FUTURE WORK

The work presented in this dissertation is a major step forward in the fundamental understanding and development of polymeric and metallic nanocomposites both in bulk scale and microscale. High strength aluminum and magnesium were successfully manufactured by a high volume production approach. It is shown that a science-guided nanoparticles incorporated into lightweight metal matrices can significantly improve their mechanical property. Many facets of the developed processes in this dissertation suggest that nanoparticles can be an effective way to engineer the mechanical and electrical properties of Al matrix. To further understand the influence of the nanoparticles on metal matrix and open up new applications for such MMNCs, future research and development are necessary.

9.1 Cost Analysis on TiB_2 Nanoparticle Synthesis

Although the synthesis of nanoparticles of high purity and small size is of great interest, cost reduction is desired for this product to be available in high volume for commercial use. The two most expensive reagents used in the current synthesis are titanium oxide and boron trioxide. Hence, reducing the cost for the aforementioned elements can decrease the final cost of the TiB_2 nanoparticles. For instance, replacing boron trioxide with boron element can reduce the material cost. However, further studies and analysis must be conducted to ensure the high quality of the TiB_2 nanoparticles. Moreover, increasing the synthesis capacity beyond the laboratory scale would lower the cost of the reagents. Reducing the TiB_2 nanoparticles synthesis cost would enable a rapid commercialization of this nanoscale reinforcement.

9.2 Expand Application of TiB_2 Nanoparticles

This work presented that small size TiB_2 nanoparticles (with an average size less than 10 nm) were successfully incorporated and self-dispersed in aluminum and magnesium matrices (both in bulk and micro scale). Refractory TiB_2 nanoparticles offer excellent mechanical, electrical, chemical, and thermal properties. Therefore, it would of tremendous interest to incorporate TiB_2 nanoparticles into other metallic, polymeric and ceramic matrices such as zinc, silver, nickel, PES, and cordierite.

9.3 Optimum Nanoparticle Volume Fraction in Flux

This work discussed a scalable manufacturing of the metal matrix nanocomposites via the flux assisted liquid state processing. In this approach a flux agent was introduced to the conventional casting to promote the incorporation efficiency of the nanoparticles into molten metals. However, an optimum volume fraction of the nanoparticles into flux will be ideal. As discussed in Chapters 6 and 7, the presence of the flux in the final nanocomposites resulted in lower mechanical property improvement than expected. This study could be of significant to minimize the amount of flux introduced to molten metal during manufacturing of metal matrix nanocomposites. For such a study, half-factorial or full-factorial or orthogonal statistical experimental design can be applied to identify the optimum nanoparticles loading in flux.

9.4 Explore New Flux for Effective Nanoparticle Feeding

This work, successfully demonstrated that a high volume fraction of nanoparticles can be incorporated into various matrices such as aluminum and magnesium. However, flux remnant was

also found in final nanocomposite samples when the melt viscosity becomes high. The presence of the flux in the final nanocomposite samples can results in property degradation. In fact, in some instances, the flux remnant neutralize the nanoparticles reinforcing effect. Flux has inherent poor wettability with most metallic matrices leading to formation of porosity or defects inside nanocomposite samples. Fluxes such as CaF_2, BaF_2 and NaF_2 or other binary and ternary combination of flux can be beneficial.

REFERENCES

[1] S. P. Rawal, "Metal-matrix composites for space applications," *JOM Journal of the Minerals, Metals and Materials Society,* vol. 53, pp. 14-17, 2001.

[2] N. Crainic and A. T. Marques, "Nanocomposites: a state-of-the-art review," in *Key engineering materials,* 2002, p. 656.

[3] Q. Jiang, X. Li, and H. Wang, "Fabrication of TiC particulate reinforced magnesium matrix composites," *Scripta Materialia,* vol. 48, pp. 713-717, 2003.

[4] Y. Yang, J. Lan, and X. Li, "Study on bulk aluminum matrix nano-composite fabricated by ultrasonic dispersion of nano-sized SiC particles in molten aluminum alloy," *Materials Science and Engineering: A,* vol. 380, pp. 378-383, 2004.

[5] G. Cao, H. Konishi, and X. Li, "Mechanical properties and microstructure of Mg/ SiC nanocomposites fabricated by ultrasonic cavitation based nanomanufacturing," *Journal of Manufacturing Science and Engineering,* vol. 130, p. 031105, 2008.

[6] N. Qu, K. Chan, and D. Zhu, "Pulse co-electrodeposition of nano Al 2 O 3 whiskers nickel composite coating," *Scripta Materialia,* vol. 50, pp. 1131-1134, 2004.

[7] L.-Y. Chen, J.-Q. Xu, H. Choi, M. Pozuelo, X. Ma, S. Bhowmick, *et al.*, "Processing and properties of magnesium containing a dense uniform dispersion of nanoparticles," *Nature,* vol. 528, pp. 539-543, 2015.

[8] N. Kaufmann, M. Imran, T. Wischeropp, C. Emmelmann, S. Siddique, and F. Walther, "Influence of process parameters on the quality of aluminium alloy EN AW 7075 using selective laser melting (SLM)," *Physics Procedia,* vol. 83, pp. 918-926, 2016.

[9] H. Zhang, H. Zhu, T. Qi, Z. Hu, and X. Zeng, "Selective laser melting of high strength Al–Cu–Mg alloys: Processing, microstructure and mechanical properties," *Materials Science and Engineering: A,* vol. 656, pp. 47-54, 2016.

[10] F. Faupel, V. Zaporojtchenko, T. Strunskus, and M. Elbahri, "Metal-Polymer Nanocomposites for Functional Applications," *Advanced Engineering Materials,* vol. 12, pp. 1177-1190, 2010.

[11] F. Gao, *Advances in polymer nanocomposites: Types and applications*: Elsevier, 2012.

[12] L. Nicolais and G. Carotenuto, *Metal-polymer nanocomposites*: John Wiley & Sons, 2004.

[13] E. A. Stefanescu, C. Daranga, and C. Stefanescu, "Insight into the broad field of polymer nanocomposites: from carbon nanotubes to clay nanoplatelets, via metal nanoparticles," *Materials,* vol. 2, pp. 2095-2153, 2009.

[14] K. Ellmer, "Past achievements and future challenges in the development of optically transparent electrodes," *Nature Photonics,* vol. 6, pp. 809-817, 2012.

[15] D. S. Hecht, L. Hu, and G. Irvin, "Emerging transparent electrodes based on thin films of carbon nanotubes, graphene, and metallic nanostructures," *Advanced Materials,* vol. 23, pp. 1482-1513, 2011.

[16] F. Xu and Y. Zhu, "Highly conductive and stretchable silver nanowire conductors," *Advanced materials,* vol. 24, pp. 5117-5122, 2012.

[17] R. M. Mutiso and K. I. Winey, "Electrical properties of polymer nanocomposites containing rod-like nanofillers," *Progress in Polymer Science,* vol. 40, pp. 63-84, 2015.

[18] M. K. Hedayati, F. Faupel, and M. Elbahri, "Review of plasmonic nanocomposite metamaterial absorber," *Materials,* vol. 7, pp. 1221-1248, 2014.

[19] I. E. Khodasevych, L. Wang, A. Mitchell, and G. Rosengarten, "Micro-and Nanostructured Surfaces for Selective Solar Absorption," *Advanced Optical Materials,* vol. 3, pp. 852-881, 2015.

[20] N. Landy, S. Sajuyigbe, J. Mock, D. Smith, and W. Padilla, "Perfect metamaterial absorber," *Physical review letters,* vol. 100, p. 207402, 2008.

[21] H. Palza, "Antimicrobial polymers with metal nanoparticles," *International journal of molecular sciences,* vol. 16, pp. 2099-2116, 2015.

[22] M. T. Byrne and Y. K. Gun'ko, "Recent advances in research on carbon nanotube–polymer composites," *Advanced Materials,* vol. 22, pp. 1672-1688, 2010.

[23] J. Glatz-Reichenbach, "Feature article conducting polymer composites," *Journal of Electroceramics,* vol. 3, pp. 329-346, 1999.

[24] W. Bauhofer and J. Z. Kovacs, "A review and analysis of electrical percolation in carbon nanotube polymer composites," *Composites Science and Technology,* vol. 69, pp. 1486-1498, 2009.

[25] W. M. Daoush, B. K. Lim, C. B. Mo, D. H. Nam, and S. H. Hong, "Electrical and mechanical properties of carbon nanotube reinforced copper nanocomposites fabricated by electroless deposition process," *Materials Science and Engineering: A,* vol. 513, pp. 247-253, 2009.

[26] J. Kang, P. Nash, J. Li, C. Shi, and N. Zhao, "Achieving highly dispersed nanofibres at high loading in carbon nanofibre–metal composites," *Nanotechnology,* vol. 20, p. 235607, 2009.

[27] H. R. Ezatpour, S. A. Sajjadi, M. H. Sabzevar, and Y. Huang, "Investigation of microstructure and mechanical properties of Al6061-nanocomposite fabricated by stir casting," *Materials & Design,* vol. 55, pp. 921-928, 2014.

[28] A. D. Hamedan and M. Shahmiri, "Production of A356–1wt% SiC nanocomposite by the modified stir casting method," *Materials Science and Engineering: A,* vol. 556, pp. 921-926, 2012.

[29] S. A. Sajjadi, H. Ezatpour, and H. Beygi, "Microstructure and mechanical properties of Al–Al 2 O 3 micro and nano composites fabricated by stir casting," *Materials Science and Engineering: A,* vol. 528, pp. 8765-8771, 2011.

[30] S. A. Sajjadi, M. T. Parizi, H. Ezatpour, and A. Sedghi, "Fabrication of A356 composite reinforced with micro and nano Al 2 O 3 particles by a developed compocasting method and study of its properties," *Journal of Alloys and Compounds,* vol. 511, pp. 226-231, 2012.

[31] B. Schultz, J. Ferguson, and P. Rohatgi, "Microstructure and hardness of Al 2 O 3 nanoparticle reinforced Al–Mg composites fabricated by reactive wetting and stir mixing," *Materials Science and Engineering: A,* vol. 530, pp. 87-97, 2011.

[32] N. Valibeygloo, R. A. Khosroshahi, and R. T. Mousavian, "Microstructural and mechanical properties of Al-4.5 wt% Cu reinforced with alumina nanoparticles by stir casting method," *International Journal of Minerals, Metallurgy, and Materials,* vol. 20, pp. 978-985, 2013.

[33] Q. Zhang, G. Chen, G. Wu, Z. Xiu, and B. Luan, "Property characteristics of a AlNp/Al composite fabricated by squeeze casting technology," *Materials Letters,* vol. 57, pp. 1453-1458, 2003.

[34] C. Thieme, S. Pourrahimi, and S. Foner, "High strength Al metal-matrix microcomposite wire with 20 vol% Nb and ultimate tensile strengths up to 1030 MPa," *Scripta metallurgica et materialia,* vol. 28, pp. 913-918, 1993.

[35] L. Tian, I. Anderson, T. Riedemann, A. Russell, and H. Kim, "Prospects for novel deformation processed Al/Ca composite conductors for overhead high voltage direct current (HVDC) power transmission," *Electric Power Systems Research,* vol. 105, pp. 105-114, 2013.

[36] Y. Wu, G.-Y. Kim, and A. M. Russell, "Mechanical alloying of carbon nanotube and Al6061 powder for metal matrix composites," *Materials Science and Engineering: A,* vol. 532, pp. 558-566, 2012.

[37] F. Hou, W. Wang, and H. Guo, "Effect of the dispersibility of ZrO 2 nanoparticles in Ni–ZrO 2 electroplated nanocomposite coatings on the mechanical properties of nanocomposite coatings," *Applied Surface Science,* vol. 252, pp. 3812-3817, 2006.

[38] Y. Jeon, J. Byun, and T. Oh, "Electrodeposition and mechanical properties of Ni–carbon nanotube nanocomposite coatings," *Journal of Physics and Chemistry of Solids,* vol. 69, pp. 1391-1394, 2008.

[39] S. Lajevardi and T. Shahrabi, "Effects of pulse electrodeposition parameters on the properties of Ni–TiO 2 nanocomposite coatings," *Applied Surface Science,* vol. 256, pp. 6775-6781, 2010.

[40] N. Qu, D. Zhu, and K. Chan, "Fabrication of Ni–CeO 2 nanocomposite by electrodeposition," *Scripta Materialia,* vol. 54, pp. 1421-1425, 2006.

[41] I. Shao, P. Vereecken, C. Chien, P. Searson, and R. Cammarata, "Synthesis and characterization of particle-reinforced Ni/Al 2 O 3 nanocomposites," *Journal of materials research,* vol. 17, pp. 1412-1418, 2002.

[42] Y.-J. Xue, D. Zhu, and F. Zhao, "Electrodeposition and mechanical properties of Ni–La 2 O 3 nanocomposites," *Journal of materials science,* vol. 39, pp. 4063-4066, 2004.

[43] A. Zimmerman, D. Clark, K. Aust, and U. Erb, "Pulse electrodeposition of Ni–SiC nanocomposite," *Materials letters,* vol. 52, pp. 85-90, 2002.

[44] Y. Mazaheri, F. Karimzadeh, and M. Enayati, "A novel technique for development of A356/Al 2 O 3 surface nanocomposite by friction stir processing," *Journal of Materials Processing Technology,* vol. 211, pp. 1614-1619, 2011.

[45] J. Xu, C. Cao, S. Das, L. Chen, C. Ma, R. S. Mishra, *et al.*, "High performance Mg6Zn nanocomposites fabricated through friction stir processing," in *Magnesium Technology 2015*, ed: Springer, 2015, pp. 383-386.

[46] H. Abdizadeh, R. Ebrahimifard, and M. A. Baghchesara, "Investigation of microstructure and mechanical properties of nano MgO reinforced Al composites manufactured by stir casting and powder metallurgy methods: A comparative study," *Composites Part B: Engineering,* vol. 56, pp. 217-221, 2014.

[47] J. Dutkiewicz, L. Lityńska, W. Maziarz, K. Haberko, W. Pyda, and A. Kanciruk, "Structure and properties of nanocomposites prepared from ball milled 6061aluminium alloy with ZrO2 nanoparticles," *Crystal Research and Technology,* vol. 44, pp. 1163-1169, 2009.

[48] M. Kubota, J. Kaneko, and M. Sugamata, "Properties of mechanically milled and spark plasma sintered Al–AlB 2 and Al–MgB 2 nano-composite materials," *Materials Science and Engineering: A,* vol. 475, pp. 96-100, 2008.

[49] M. Marques, V. Livramento, J. Correia, A. Almeida, and R. Vilar, "Production of copper–niobium carbide nanocomposite powders via mechanical alloying," *Materials Science and Engineering: A,* vol. 399, pp. 382-386, 2005.

[50] N. Nemati, R. Khosroshahi, M. Emamy, and A. Zolriasatein, "Investigation of microstructure, hardness and wear properties of Al–4.5 wt.% Cu–TiC nanocomposites produced by mechanical milling," *Materials & Design,* vol. 32, pp. 3718-3729, 2011.

[51] R. Pérez-Bustamante, C. Gómez-Esparza, I. Estrada-Guel, M. Miki-Yoshida, L. Licea-Jiménez, S. Pérez-García, *et al.*, "Microstructural and mechanical characterization of Al–MWCNT composites produced by mechanical milling," *Materials Science and Engineering: A,* vol. 502, pp. 159-163, 2009.

[52] D. Poirier, R. A. Drew, M. L. Trudeau, and R. Gauvin, "Fabrication and properties of mechanically milled alumina/aluminum nanocomposites," *Materials Science and Engineering: A,* vol. 527, pp. 7605-7614, 2010.

[53] Z. Sadeghian, M. Enayati, and P. Beiss, "In situ production of Al–TiB2 nanocomposite by double-step mechanical alloying," *Journal of materials science,* vol. 44, pp. 2566-2572, 2009.

[54] N. Saheb, I. K. Aliyu, S. F. Hassan, and N. Al-Aqeeli, "Matrix structure evolution and nanoreinforcement distribution in mechanically milled and spark plasma sintered Al-SiC nanocomposites," *Materials,* vol. 7, pp. 6748-6767, 2014.

[55] T. Takahashi and Y. Hashimoto, "Preparation of dispersion-strengthened coppers with NbC and TaC by mechanical alloying," *Materials Transactions, JIM,* vol. 32, pp. 389-397, 1991.

[56] A. A. Yar, M. Montazerian, H. Abdizadeh, and H. Baharvandi, "Microstructure and mechanical properties of aluminum alloy matrix composite reinforced with nano-particle MgO," *Journal of Alloys and Compounds,* vol. 484, pp. 400-404, 2009.

[57] D. Ying and D. Zhang, "Processing of Cu–Al 2 O 3 metal matrix nanocomposite materials by using high energy ball milling," *Materials Science and Engineering: A,* vol. 286, pp. 152-156, 2000.

[58] M. Doubenskaia, A. K. Gilmutdinov, and K. Y. Nagulin, "Laser cladding of metal matrix composites reinforced by cermet inclusions for dry friction applications at ambient and elevated temperatures," *Surface and Coatings Technology,* vol. 276, pp. 696-703, 2015.

[59] D. Gu, H. Wang, and D. Dai, "Laser additive manufacturing of novel aluminum based nanocomposite parts: tailored forming of multiple materials," *Journal of Manufacturing Science and Engineering,* vol. 138, p. 021004, 2016.

[60] D. Gu, H. Wang, D. Dai, F. Chang, W. Meiners, Y.-C. Hagedorn, *et al.*, "Densification behavior, microstructure evolution, and wear property of TiC nanoparticle reinforced AlSi10Mg bulk-form nanocomposites prepared by selective laser melting," *Journal of Laser Applications,* vol. 27, p. S17003, 2015.

[61] D. Gu and G. Zhang, "Selective laser melting of novel nanocomposites parts with enhanced tribological performance: nanocrystalline TiC/Ti nanocomposites parts were built via SLM technology and the densification, microstructures, microhardness and tribological performance were investigated," *Virtual and Physical Prototyping,* vol. 8, pp. 11-18, 2013.

[62] B. Song, S. Dong, and C. Coddet, "Rapid in situ fabrication of Fe/SiC bulk nanocomposites by selective laser melting directly from a mixed powder of microsized Fe and SiC," *Scripta Materialia,* vol. 75, pp. 90-93, 2014.

[63] M. Zhong, D. Jiang, H. Zhang, C. Hong, A. Weisheit, and I. Kelbassa, "Fabrication of nanoparticulate reinforced metal matrix composites by laser cladding," *Journal of Laser Applications,* vol. 26, p. 022007, 2014.

[64] N. Grossiord, J. Loos, O. Regev, and C. E. Koning, "Toolbox for dispersing carbon nanotubes into polymers to get conductive nanocomposites," *Chemistry of materials,* vol. 18, pp. 1089-1099, 2006.

[65] J. Hou, Q. Wang, H. Yang, X. Wu, C. Li, X. Li, *et al.*, "Microstructure evolution and strengthening mechanisms of cold-drawn commercially pure aluminum wire," *Materials Science and Engineering: A,* vol. 639, pp. 103-106, 2015.

[66] H. Rhee, W. R. Whittington, A. L. Oppedal, A. R. Sherif, R. L. King, H.-J. Kim, *et al.*, "Mechanical properties of novel aluminum metal matrix metallic composites: Application to overhead conductors," *Materials & Design,* vol. 88, pp. 16-21, 2015.

[67] (February 16, 2017, November 4, 2017). *How much electricity is lost in transmission and distribution in the United States?* Available: https://www.eia.gov/tools/faqs/faq.php?id=105&t=3

[68] M. Cabibbo, "Microstructure strengthening mechanisms in different equal channel angular pressed aluminum alloys," *Materials Science and Engineering: A,* vol. 560, pp. 413-432, 2013.

[69] S. Ding, W. Lee, C. Chang, L. Chang, and P. Kao, "Improvement of strength of magnesium alloy processed by equal channel angular extrusion," *Scripta Materialia,* vol. 59, pp. 1006-1009, 2008.

[70] W. Kim and J. Wang, "Microstructure of the post-ECAP aging processed 6061 Al alloys," *Materials Science and Engineering: A,* vol. 464, pp. 23-27, 2007.

[71] N. Q. Chinh, J. Gubicza, and T. Langdon, "Characteristics of face-centered cubic metals processed by equal-channel angular pressing," *Journal of materials science,* vol. 42, pp. 1594-1605, 2007.

[72] Y. Ito and Z. Horita, "Microstructural evolution in pure aluminum processed by high-pressure torsion," *Materials Science and Engineering: A,* vol. 503, pp. 32-36, 2009.

[73] A. P. Zhilyaev and T. G. Langdon, "Using high-pressure torsion for metal processing: Fundamentals and applications," *Progress in Materials Science,* vol. 53, pp. 893-979, 2008.

[74] G. Sakai, Z. Horita, and T. G. Langdon, "Grain refinement and superplasticity in an aluminum alloy processed by high-pressure torsion," *Materials Science and Engineering: A,* vol. 393, pp. 344-351, 2005.

[75] N. Kamikawa, X. Huang, N. Tsuji, and N. Hansen, "Strengthening mechanisms in nanostructured high-purity aluminium deformed to high strain and annealed," *Acta Materialia,* vol. 57, pp. 4198-4208, 2009.

[76] A. M. Russell, L. S. Chumbley, and Y. Tian, "Deformation processed metal–metal composites," *Advanced Engineering Materials,* vol. 2, pp. 11-22, 2000.

[77] Y. Saito, H. Utsunomiya, N. Tsuji, and T. Sakai, "Novel ultra-high straining process for bulk materials—development of the accumulative roll-bonding (ARB) process," *Acta materialia,* vol. 47, pp. 579-583, 1999.

[78] R. L. Fleischer, "Solution hardening by tetragonal dist ortions: Application to irradiation hardening in FCC crystals," *Acta metallurgica,* vol. 10, pp. 835-842, 1962.

[79] R. Fleischer, "Substitutional solution hardening," *Acta metallurgica,* vol. 11, pp. 203-209, 1963.

[80] G. Fribourg, Y. Bréchet, A. Deschamps, and A. Simar, "Microstructure-based modelling of isotropic and kinematic strain hardening in a precipitation-hardened aluminium alloy," *Acta Materialia,* vol. 59, pp. 3621-3635, 2011.

[81] A. Gupta, D. Lloyd, and S. Court, "Precipitation hardening in Al–Mg–Si alloys with and without excess Si," *Materials Science and Engineering: A,* vol. 316, pp. 11-17, 2001.

[82] C. Carlton and P. Ferreira, "What is behind the inverse Hall–Petch effect in nanocrystalline materials?," *Acta Materialia,* vol. 55, pp. 3749-3756, 2007.

[83] K. Ma, H. Wen, T. Hu, T. D. Topping, D. Isheim, D. N. Seidman, *et al.*, "Mechanical behavior and strengthening mechanisms in ultrafine grain precipitation-strengthened aluminum alloy," *Acta Materialia,* vol. 62, pp. 141-155, 2014.

[84] D. N. Seidman, E. A. Marquis, and D. C. Dunand, "Precipitation strengthening at ambient and elevated temperatures of heat-treatable Al (Sc) alloys," *Acta Materialia,* vol. 50, pp. 4021-4035, 2002.

[85] A. Russell, T. Lund, L. Chumbley, F. Laabs, L. Keehner, and J. Harringa, "A high-strength, high-conductivity Al–Ti deformation processed metal metal matrix composite," *Composites Part A: Applied Science and Manufacturing,* vol. 30, pp. 239-247, 1999.

[86] K. Xu, A. Russell, L. Chumbley, F. Laabs, V. Gantovnik, and Y. Tian, "Characterization of strength and microstructure in deformation processed Al-Mg composites," *Journal of materials science,* vol. 34, pp. 5955-5959, 1999.

[87] O. Hernández and G. Gonzalez, "Microstructural and mechanical behavior of highly deformed Al–Sn alloys," *Materials characterization,* vol. 59, pp. 534-541, 2008.

[88] T. J. Kang, M. Cha, E. Y. Jang, J. Shin, H. U. Im, Y. Kim, *et al.*, "Ultra-thin and Conductive Nanomembrane Arrays for Nanomechanical Transducers," *Advanced Materials,* vol. 20, pp. 3131-3137, 2008.

[89] F. Du, J. E. Fischer, and K. I. Winey, "Coagulation method for preparing single-walled carbon nanotube/poly (methyl methacrylate) composites and their modulus, electrical conductivity, and thermal stability," *Journal of Polymer Science Part B: Polymer Physics,* vol. 41, pp. 3333-3338, 2003.

[90] P. Pötschke, A. R. Bhattacharyya, and A. Janke, "Melt mixing of polycarbonate with multiwalled carbon nanotubes: microscopic studies on the state of dispersion," *European Polymer Journal,* vol. 40, pp. 137-148, 2004.

[91] B. P. Grady, "Recent developments concerning the dispersion of carbon nanotubes in polymers," *Macromolecular rapid communications,* vol. 31, pp. 247-257, 2010.

[92] M. Moniruzzaman and K. I. Winey, "Polymer nanocomposites containing carbon nanotubes," *Macromolecules,* vol. 39, pp. 5194-5205, 2006.

[93] C. Goujon and P. Goeuriot, "Solid state sintering and high temperature compression properties of Al-alloy5000/AlN nanocomposites," *Materials Science and Engineering: A,* vol. 315, pp. 180-188, 2001.

[94] T. Laha and A. Agarwal, "Effect of sintering on thermally sprayed carbon nanotube reinforced aluminum nanocomposite," *Materials Science and Engineering: A,* vol. 480, pp. 323-332, 2008.

[95] J. Ye, B. Q. Han, Z. Lee, B. Ahn, S. R. Nutt, and J. M. Schoenung, "A tri-modal aluminum based composite with super-high strength," *Scripta Materialia,* vol. 53, pp. 481-486, 2005.

[96] R. Erbel, C. Di Mario, J. Bartunek, J. Bonnier, B. de Bruyne, F. R. Eberli, *et al.*, "Temporary scaffolding of coronary arteries with bioabsorbable magnesium stents: a prospective, non-randomised multicentre trial," *The Lancet,* vol. 369, pp. 1869-1875, 2007.

[97] E. L. Dreizin, C. H. Berman, and E. P. Vicenzi, "Condensed-phase modifications in magnesium particle combustion in air," *Combustion and Flame,* vol. 122, pp. 30-42, 2000.

[98] A. A. Luo and B. R. Powell, "Tensile and Compressive Creep of Magnesium-Aluminum-Calcium Based Alloys," *Magnesium Technology 2001*, pp. 137-144, 2001.

[99] M. M. Avedesian and H. Baker, *ASM specialty handbook: magnesium and magnesium alloys*: ASM international, 1999.

[100] P. Knochel, "A flash of magnesium," *Nature chemistry*, vol. 1, pp. 740-740, 2009.

[101] W. Sillekens, D. Jarvis, A. Vorozhtsov, V. Bojarevics, C. F. Badini, M. Pavese, *et al.*, "The ExoMet project: EU/ESA research on high-performance light-metal alloys and nanocomposites," *Metallurgical and Materials Transactions A*, vol. 45, pp. 3349-3361, 2014.

[102] G. Liu, G. Zhang, F. Jiang, X. Ding, Y. Sun, J. Sun, *et al.*, "Nanostructured high-strength molybdenum alloys with unprecedented tensile ductility," *Nature materials*, vol. 12, pp. 344-350, 2013.

[103] Z. Zhang and D. Chen, "Consideration of Orowan strengthening effect in particulate-reinforced metal matrix nanocomposites: a model for predicting their yield strength," *Scripta Materialia*, vol. 54, pp. 1321-1326, 2006.

[104] M. Gupta and W. Wong, "Magnesium-based nanocomposites: Lightweight materials of the future," *Materials Characterization*, vol. 105, pp. 30-46, 2015.

[105] M. Gupta and W. L. E. Wong, "An insight into processing and characteristics of magnesium based composites," in *Magnesium Technology 2014*, ed: Springer, 2014, pp. 423-428.

[106] X. Li, Y. Yang, and X. Cheng, "Ultrasonic-assisted fabrication of metal matrix nanocomposites," *Journal of Materials Science*, vol. 39, pp. 3211-3212, 2004.

[107] A. Mortensen and J. Llorca, "Metal matrix composites," *Annual review of materials research*, vol. 40, pp. 243-270, 2010.

[108] A. Luo, "Processing, microstructure, and mechanical behavior of cast magnesium metal matrix composites," *Metallurgical and Materials Transactions A*, vol. 26, pp. 2445-2455, 1995.

[109] W. Zhou and Z. Xu, "Casting of SiC reinforced metal matrix composites," *Journal of Materials Processing Technology*, vol. 63, pp. 358-363, 1997.

[110] A. Javadi, C. Cao, and X. Li, "Manufacturing of Al-TiB2 Nanocomposites by Flux-Assisted Liquid State Processing," *Procedia Manufacturing*, vol. 10, pp. 531-535, 2017.

[111] A. Kennedy and A. Karantzalis, "The incorporation of ceramic particles in molten aluminium and the relationship to contact angle data," *Materials Science and Engineering: A*, vol. 264, pp. 122-129, 1999.

[112] I. Ibrahim, F. Mohamed, and E. Lavernia, "Particulate reinforced metal matrix composites—a review," *Journal of materials science,* vol. 26, pp. 1137-1156, 1991.

[113] J. Kaczmar, K. Pietrzak, and W. Włosiński, "The production and application of metal matrix composite materials," *Journal of Materials Processing Technology,* vol. 106, pp. 58-67, 2000.

[114] L.-Y. Chen, H. Konishi, A. Fehrenbacher, C. Ma, J.-Q. Xu, H. Choi, *et al.*, "Novel nanoprocessing route for bulk graphene nanoplatelets reinforced metal matrix nanocomposites," *Scripta Materialia,* vol. 67, pp. 29-32, 2012.

[115] J. Ferguson, F. Sheykh-Jaberi, C.-S. Kim, P. K. Rohatgi, and K. Cho, "On the strength and strain to failure in particle-reinforced magnesium metal-matrix nanocomposites (Mg MMNCs)," *Materials Science and Engineering: A,* vol. 558, pp. 193-204, 2012.

[116] H. Ferkel and B. Mordike, "Magnesium strengthened by SiC nanoparticles," *Materials Science and Engineering: A,* vol. 298, pp. 193-199, 2001.

[117] S. C. Tjong, "Novel nanoparticle-reinforced metal matrix composites with enhanced mechanical properties," *Advanced engineering materials,* vol. 9, pp. 639-652, 2007.

[118] S. Karabay and F. K. Önder, "An approach for analysis in refurbishment of existing conventional HV–ACSR transmission lines with AAAC," *Electric power systems research,* vol. 72, pp. 179-185, 2004.

[119] S. Karabay, "Influence of AlB 2 compound on elimination of incoherent precipitation in artificial aging of wires drawn from redraw rod extruded from billets cast of alloy AA-6101 by vertical direct chill casting," *Materials & Design,* vol. 29, pp. 1364-1375, 2008.

[120] J. M. Hesterlee, E. T. Sanders, and F. R. Thrash, "Bare overhead transmission and distribution conductor design overview," *IEEE Transactions on Industry Applications,* vol. 32, pp. 709-713, 1996.

[121] C. McCullough, H. E. Deve, and T. N. Staffaroni, "Method of installing an electrical transmission cable," ed: Google Patents, 2011.

[122] C. Hiel, G. Korzeniowski, and D. Bryant, "Aluminum conductor composite core reinforced cable and method of manufacture," ed: Google Patents, 2007.

[123] A. Alawar, E. J. Bosze, and S. R. Nutt, "A composite core conductor for low sag at high temperatures," *IEEE transactions on power delivery,* vol. 20, pp. 2193-2199, 2005.

[124] Q. Gao, S. Wu, L. Shulin, X. Duan, and P. An, "Preparation of in-situ 5vol% TiB 2 particulate reinforced Al–4.5 Cu alloy matrix composites assisted by improved mechanical stirring process," *Materials & Design,* vol. 94, pp. 79-86, 2016.

[125] M. Estruga, L. Chen, H. Choi, X. Li, and S. Jin, "Ultrasonic-assisted synthesis of surface-clean TiB2 nanoparticles and their improved dispersion and capture in Al-matrix nanocomposites," *ACS applied materials & interfaces,* vol. 5, pp. 8813-8819, 2013.

[126] D. Portehault, S. Devi, P. Beaunier, C. Gervais, C. Giordano, C. Sanchez, *et al.*, "A general solution route toward metal boride nanocrystals," *Angewandte Chemie International Edition,* vol. 50, pp. 3262-3265, 2011.

[127] M. Estruga, S. N. Girard, Q. Ding, L. Chen, X. Li, and S. Jin, "Facile and scalable synthesis of Ti 5 Si 3 nanoparticles in molten salts for metal-matrix nanocomposites," *Chemical Communications,* vol. 50, pp. 1454-1457, 2014.

[128] A. Javadi, J. Zhao, C. Cao, M. Pozuelo, Y. Yang, I. Hwang, *et al.*, "Stretching Micro Metal Particles into Uniformly Dispersed and Sized Nanoparticles in Polymer," *Scientific Reports,* vol. 7, p. 7098, 2017.

[129] Q. Zhou, L. Zeng, M. DeCicco, X. Li, and S. Zhou, "A comparative study on clustering indices for distribution uniformity of nanoparticles in metal matrix nanocomposites," *CIRP Journal of Manufacturing Science and Technology,* vol. 5, pp. 348-356, 2012.

[130] C. A. Schneider, W. S. Rasband, and K. W. Eliceiri, "NIH Image to ImageJ: 25 years of image analysis," *Nat Meth,* vol. 9, pp. 671-675, 07//print 2012.

[131] C. Subramanian, T. C. Murthy, and A. Suri, "Synthesis and consolidation of titanium diboride," *International Journal of Refractory Metals and Hard Materials,* vol. 25, pp. 345-350, 2007.

[132] H. Zarrinpour, S. Firoozi, and V. Milani, "Ignition and chemical mechanisms of volume combustion synthesis of titanium diboride," *Ceramics International,* vol. 42, pp. 11217-11223, 2016.

[133] K. Bao, Y. Wen, M. Khangkhamano, and S. Zhang, "Low-temperature preparation of titanium diboride fine powder via magnesiothermic reduction in molten salt," *Journal of the American Ceramic Society,* vol. 100, pp. 2266-2272, 2017.

[134] R. Baboian, D. Hill, and R. Bailey, "Electrochemical studies on titanium in molten LiCl–KCl eutectic," *Canadian Journal of Chemistry,* vol. 43, pp. 197-205, 1965.

[135] R. O. Suzuki, T. Matsunaga, K. Ono, T. N. Harada, and T. N. Deura, "Titanium powder prepared by magnesiothermic reduction of Ti 2+ in molten salt," *Metallurgical and Materials Transactions B,* vol. 30, pp. 403-410, 1999.

[136] Y. Huang, X. Duan, Q. Wei, and C. M. Lieber, "Directed assembly of one-dimensional nanostructures into functional networks," *Science,* vol. 291, pp. 630-633, 2001.

[137] Y. Lin, H. Skaff, T. Emrick, A. Dinsmore, and T. P. Russell, "Nanoparticle assembly and transport at liquid-liquid interfaces," *Science,* vol. 299, pp. 226-229, 2003.

[138] Y. Min, M. Akbulut, K. Kristiansen, Y. Golan, and J. Israelachvili, "The role of interparticle and external forces in nanoparticle assembly," *Nature materials,* vol. 7, pp. 527-538, 2008.

[139] D. J. Pochan, "Approaching asymmetry and versatility in polymer assembly," *Science,* vol. 337, pp. 530-531, 2012.

[140] K. M. Ryan, A. Mastroianni, K. A. Stancil, H. Liu, and A. Alivisatos, "Electric-field-assisted assembly of perpendicularly oriented nanorod superlattices," *Nano letters,* vol. 6, pp. 1479-1482, 2006.

[141] G. M. Whitesides and B. Grzybowski, "Self-assembly at all scales," *Science,* vol. 295, pp. 2418-2421, 2002.

[142] P. Yang, "Nanotechnology: Wires on water," *Nature,* vol. 425, pp. 243-244, 2003.

[143] D. L. Huber, "Synthesis, properties, and applications of iron nanoparticles," *Small,* vol. 1, pp. 482-501, 2005.

[144] Z. Nie, A. Petukhova, and E. Kumacheva, "Properties and emerging applications of self-assembled structures made from inorganic nanoparticles," *Nature nanotechnology,* vol. 5, pp. 15-25, 2010.

[145] V. Subramanian, E. E. Wolf, and P. V. Kamat, "Catalysis with TiO2/gold nanocomposites. Effect of metal particle size on the Fermi level equilibration," *Journal of the American Chemical Society,* vol. 126, pp. 4943-4950, 2004.

[146] W. Liu, X. Yan, G. Chen, and Z. Ren, "Recent advances in thermoelectric nanocomposites," *Nano Energy,* vol. 1, pp. 42-56, 2012.

[147] A. Vu, Y. Qian, and A. Stein, "Porous Electrode Materials for Lithium-Ion Batteries–How to Prepare Them and What Makes Them Special," *Advanced Energy Materials,* vol. 2, pp. 1056-1085, 2012.

[148] B. Zhang, D. Ye, J. Li, X. Zhu, and Q. Liao, "Electrodeposition of Pd catalyst layer on graphite rod electrodes for direct formic acid oxidation," *Journal of Power Sources,* vol. 214, pp. 277-284, 2012.

[149] S. Cataldo, B. Pignataro, A. Ruggirello, C. Bongiorno, and V. T. Liveri, "The zero field self-organization of cobalt/surfactant nanocomposite thin films," *Nanotechnology,* vol. 20, p. 225605, 2009.

[150] J. Cheon, J.-I. Park, J.-s. Choi, Y.-w. Jun, S. Kim, M. G. Kim, *et al.*, "Magnetic superlattices and their nanoscale phase transition effects," *Proceedings of the National Academy of Sciences of the United States of America,* vol. 103, pp. 3023-3027, 2006.

[151] L. Vovchenko, L. Matzui, O. Stelmakh, and M. Zakharenko, "Electric and Magnetoresistance of Nanocomposite Material Graphite-Cobalt," *Fullerenes, nanotubes, and carbon nanostructures,* vol. 13, pp. 491-495, 2005.

[152] T. Hirakawa and P. V. Kamat, "Charge separation and catalytic activity of Ag@ TiO2 core− shell composite clusters under UV− irradiation," *Journal of the American Chemical Society,* vol. 127, pp. 3928-3934, 2005.

[153] X.-F. Wu, H.-Y. Song, J.-M. Yoon, Y.-T. Yu, and Y.-F. Chen, "Synthesis of core− shell Au@ TiO2 nanoparticles with truncated wedge-shaped morphology and their photocatalytic properties," *Langmuir,* vol. 25, pp. 6438-6447, 2009.

[154] R. G. Lye and E. Logothetis, "Optical properties and band structure of titanium carbide," *Physical Review,* vol. 147, p. 622, 1966.

[155] J. Xu, L. Chen, H. Choi, and X. Li, "Theoretical study and pathways for nanoparticle capture during solidification of metal melt," *Journal of Physics: Condensed Matter,* vol. 24, p. 255304, 2012.

[156] J. N. Israelachvili, *Intermolecular and surface forces*: Academic press, 2011.

[157] Y. Li, Y. Zhao, V. Ortalan, W. Liu, Z. Zhang, R. Vogt, *et al.,* "Investigation of aluminum-based nanocomposites with ultra-high strength," *Materials Science and Engineering: A,* vol. 527, pp. 305-316, 2009.

[158] P. Drude, *The theory of optics*: Courier Corporation, 1925.

[159] W. Gao and N. M. Sammes, *An introduction to electronic and ionic materials*: World Scientific Publishing Co Inc, 1999.

[160] P. Andrews, M. West, and C. Robeson, "The effect of grain boundaries on the electrical resistivity of polycrystalline copper and aluminium," *Philosophical Magazine,* vol. 19, pp. 887-898, 1969.

[161] Y. Miyajima, S.-Y. Komatsu, M. Mitsuhara, S. Hata, H. Nakashima, and N. Tsuji, "Change in electrical resistivity of commercial purity aluminium severely plastic deformed," *Philosophical Magazine,* vol. 90, pp. 4475-4488, 2010.

[162] J. Friedel, "On some electrical and magnetic properties of metallic solid solutions," *Canadian Journal of Physics,* vol. 34, pp. 1190-1211, 1956.

[163] V. Nordheim, "Zur theorie der Elektronen in Metallen," *Ann. Phys,* vol. 5, p. 642, 1931.

[164] C. Kittel and H. Kroemer, "Thermal physics," ed: AAPT, 1998.

[165] A. Yaniv, "Electronic properties of a simple metal-metal interface," *Physical Review B,* vol. 17, p. 3904, 1978.

[166] W. Zhao, Z. Liu, Z. Sun, Q. Zhang, P. Wei, X. Mu, *et al.*, "Superparamagnetic enhancement of thermoelectric performance," *Nature,* vol. 549, pp. 247-251, 2017.

[167] M. L. Cohen and S. G. Louie, *Fundamentals of condensed matter physics*: Cambridge University Press, 2016.

[168] H. Hamaker, "The London—van der Waals attraction between spherical particles," *physica,* vol. 4, pp. 1058-1072, 1937.

[169] S. Rhee, "Wetting of AlN and TiC by liquid Ag and liquid Cu," *Journal of the American Ceramic Society,* vol. 53, pp. 639-641, 1970.

[170] B. Cook, A. Russell, J. Peters, and J. Harringa, "Estimation of surface energy and bonding between AlMgB 14 and TiB 2," *Journal of Physics and Chemistry of Solids,* vol. 71, pp. 824-826, 2010.